Growing Faults in the Lab: Design and Application of a New Experiment to Study Deformation Processes in Laboratory Scale Models

Dissertation

zur Erlangung des Doktorgrades

Doctor rerum naturalium (Dr. rer. nat.)

im Fachbereich Geowissenschaften
an der Freien Universität Berlin

vorgelegt von

Malte Christian Ritter

aus Bremen

Berlin, 2017

Erstgutachter: Prof. Dr. Onno Oncken
Freie Universität Berlin, GeoForschungsZentrum Potsdam

Zweitgutachter: Prof. Dr. Guido Schreurs
Universität Bern

Datum der Disputation: 20. 06. 2017

Erklärung

nach §7 (4) der Promotionsordnung des Fachbereichs Geowissenschaften an der Freien Universität Berlin:

Hiermit erkläre ich, dass die vorliegende Dissertation ohne unzulässige Hilfe Dritter und ohne Benutzung anderer als der angegebenen Literatur angefertigt wurde. Die Stellen der Arbeit, die anderen Werken wörtlich oder inhaltlich entnommen sind, wurden durch entsprechende Angaben der Quellen kenntlich gemacht. Diese Arbeit hat in gleicher oder ähnlicher Form noch keiner Prüfungsbehörde vorgelegen.

Potsdam, März 2017

Abstract

Fault zones are key elements in plate tectonics and important pathways for fluid flow within the Earth's crust, which makes their presence or absence a governing factor for the occurrence of mineral deposits and petroleum reservoirs. Furthermore, seismic activity on fault zones is a hazard to nearby settlements. Mechanically, fault zones can be regarded as narrow, weak zones within a strong host material that form through the processes of strain localisation and strain weakening. Understanding fault system evolution in detail, however, is hindered by their long lifetime and the limited resolution of available geological data. Analogue experiments using loose quartz sand are a viable tool to circumvent these problems and to shed light on the processes controlling fault zone evolution. So far these experiments have mostly considered the kinematic evolution. In this study I develop a new analogue sandbox experiment that combines high-resolution measurements of deformation and strength in order to deepen our understanding of fault system evolution.

In a first step new scaling relations are derived that take into account the transient strength evolution of both, analogue material and natural prototype. Through detailed mechanical tests a previously unrecognised scale dependence of strain weakening is detected that restricts the applicability of the tested analogue material to models with a certain length scale. This length scale is determined by comparison with natural data, considering different common assumptions for the strength of the brittle crust. The scaling values thus obtained can be transferred to other tectonic sandbox experiments.

In a second step a new experimental set-up is developed that is capable of simultaneously measuring deformation and strength evolution at the required resolution and in various tectonic settings. A detailed description of the set-up is given and two standard experiments, a convergent wedge and a Riedel-type strike-slip experiment, are analysed with respect to the temporal relations between deformation and strength evolution. This analysis reveals neither of the two tectonic settings to be particularly well suited to the problem under consideration.

Therefore, in a third step, the new set-up is applied in a different strike-slip setting akin to a transfer fault zone connecting two dip-slip faults. The work required to grow a fault is measured as a function of fault system size. It is found to increase in an approximately quadratic relation with fault length. This is caused by a corresponding increase of diffuse deformation around the fault, which can be interpreted as reflecting sub-seismic deformation in nature. The observed dependence is in accordance with theoretical predictions for natural fault zones; and the numerical values are similar to estimates from measured earthquake energy release rates in nature.

Zusammenfassung

Störungszonen sind Schlüsselelemente in plattentektonischen Prozessen und wichtige Fluidtransportwege innerhalb der spröden Erdkruste. Letzteres macht sie zu einem entscheidenden Faktor für das Vorkommen wirtschaftlich bedeutender Lagerstätten. Darüber hinaus stellt die Erdbebentätigkeit aktiver Störungszonen eine erhebliche Gefahr für nahegelegene Siedlungsgebiete dar. Aus mechanischer Sicht lassen sich Störungszonen als schmale Schwächezonen in einem festen Umgebungsmaterial beschreiben, die durch die Lokalisierung von Verformung und damit einhergehende Verformungsentfestigung gebildet werden. Ein tieferes Verständnis der Entwicklung von Störungssystemen wird jedoch durch ihre lange Lebensdauer sowie die geringe Auflösung zur Verfügung stehender geologischer Daten erschwert. Analogexperimente, in denen unverfestigter Quarzsand als Analogon der spröden Erdkruste verwendet wird, stellen einen gangbaren Weg dar diese Schwierigkeiten zu umgehen. Bisher haben derartige Studien überwiegend die kinematische Entwicklung von Störungssystemen untersucht. In dieser Arbeit hingegen entwickle ich einen neuartigen Versuchsaufbau, in dem hochauflösende Deformations- und Festigkeitsmessungen verwendet werden, um neue Erkenntnisse über die Entstehung von Störungssystemen zu gewinnen.

In einem ersten Schritt werden neue Skalierungsparameter hergeleitet, die die transiente Festigkeitsentwicklung sowohl des Analogmaterials als auch des natürlichen Prototyps berücksichtigen. Anhand ausführlicher mechanischer Tests wird eine bisher unerkannte Skalenabhängigkeit der Verformungsentfestigung nachgewiesen, die die Anwendbarkeit der untersuchten Analogmaterialien auf Modelle mit einem bestimmten Längenmaßstab einschränkt. Dieser Längenmaßstab wird durch Vergleich mit natürlichen Festigkeitsdaten ermittelt, wobei verschiedene gängige Annahmen über die Festigkeit der Erdkruste in die Betrachtungen einbezogen werden. Die ermittelten Skalierungsparameter können auf andere tektonische Analogexperimente übertragen werden.

In einem zweiten Schritt wird ein neuer Versuchsaufbau entwickelt, der gleichzeitige Messungen der Deformations- und Festigkeitsentwicklung bei der geforderten Auflösung und in verschiedenen tektonischen Umgebungen ermöglicht. Der Versuchsaufbau wird im Detail beschrieben und zwei Standardexperimente, ein konvergenter Keil sowie eine Riedel-Transformstörung, werden im Hinblick auf den zeitlichen Zusammenhang von Deformation und Festigkeitsentwicklung analysiert. Im Rahmen dieser Analyse erweist sich keines der beiden Experimente als für die Untersuchung der Problemstellung geeignet.

Daher wird der neue Versuchsaufbau im dritten Schritt in einem weiteren tektonischen Szenario verwendet, nämlich dem einer Transformzone ohne basale Diskon-

tinuität, wie sie in der Natur den Versatz zwischen zwei Auf- oder Abschiebungen übertragen. Die Arbeit, die für die Ausbreitung der Störung notwendig ist, wird in Abhängigkeit der Störungslänge gemessen. Diese Größen stehen in einer ungefähr quadratischen Abhängigkeit zueinander, die von einer entsprechenden Zunahme der diffusen Deformation im Umfeld der Störung hervorgerufen wird. Diffuse Deformation wird in diesem Zusammenhang als Abbild kleinskaliger Deformation unterhalb der seismischen Auflösung interpretiert. Die beobachtete Abhängigkeit der aufzuwendenden Arbeit von der Störungslänge steht im Einklang mit theoretischen Modellen für natürliche Störungszonen. Ebenso stimmen die ermittelten Werte der Arbeit mit Abschätzungen aus natürlichen Erdbeben überein.

Contents

List of Figures

1 Introduction

1.1 Motivation

Fault zones are important features within the Earth's crust, both geologically and economically. Geologically they are important as zones that accommodate the long-term deformation shaping the Earth's surface during orogenesis, subduction and other tectonic processes. They can be both, pathways and barriers, for fluid flow within the Earth's crust that either connect or seal petroleum reservoirs, which makes them economically interesting. As pathways for hydrothermal fluids they may also form exploitable mineral deposits. At the same time, active large fault systems cause seismic hazard to human settlements in their vicinity. Many zones of dense population lie at or close to active fault systems despite this hazard, such as around the Pacific Ocean with the coasts of the Americas, Japan and the Philippines, or along the northern and eastern Mediterranean coasts. Detailed knowledge about the processes acting in fault zones is therefore of fundamental importance. This thesis aims at improving the understanding of generation and long-term evolution of fault zones, i. e. the processes that transform intact rock into mature fault zones over time-spans of several million years.

1.2 Strain Localisation in the Earth's Crust

On a long time-scale, elastic deformation and the occurrence of earthquakes can be assumed to be negligible short-term oscillations that average each other out. Formation of fault zones is then the localisation of plastic strain into shear zones that is driven by mechanical weakening of the overall system (Hobbs et al., 1990). The ability to localise strain is a fundamental characteristic of nearly all Earth's materials and can be observed over a wide range of scales, from laboratory rock samples to outcrops and entire continents (e g. Ramsay, 1980; Ben-Zion and Sammis, 2003).

The process of strain localisation in brittle rock is still not fully understood. For a simple, homogeneous material, such as a glass rod or a single crystal, it can be satisfactorily explained by stress concentrations that occur at the edges of inherent imperfections within a sample ("Griffith cracks") and that locally exceed the atomic bonding strength of the material, resulting in propagation of the crack. This leads to macroscopic weakening and ultimately to separation into two pieces along a discrete plane within otherwise intact material. Griffith (1921) derived an analytical

description of the energy balance of this process, that has subsequently been verified experimentally (see Orowan, 1949, for a review).

For polycrystalline materials, such as rock, the process is more complicated and the response of the great number of different grains with intercalated zones of weakness (e. g. the grain boundaries) cannot be described in a simple analytical model. Yet, localisation has been found to be closely linked to weakening in laboratory experiments on brittle rock samples as well (Wawersik and Fairhurst, 1970; Rummel and Fairhurst, 1970; Crouch, 1971; Holyoke and Tullis, 2006). Other than in homogeneous materials, weakening in rock is preceded by a phase of inelastic hardening. During this, deformation takes the form of opening of micro-cracks in a wide zone around the future fault plane. This opening can be detected through sample dilation or acoustic emission (Brace et al., 1966; Lockner et al., 1992). Some of the micro-cracks subsequently coalesce to form a through-going fracture while the sample weakens (Lockner et al., 1992). Brady et al. (1973) showed weakening to be proportional to the reduction of the cross-sectional area of the coherent portion of the rock sample, which indicates an analogue relationship between weakening and localisation as on the atomic scale described above.

Similar behaviour can be observed on a crustal scale, although it is more difficult to quantify in this case: For the North Sea Rift System, Cowie et al. (2005) reported a gradual increase of strain rate at the rift axis over time, while it simultaneously decreased at the basin margins. This process lasted about 30 Ma. Their study could not unequivocally resolve the causes leading to such localisation. Likewise, from investigations of the Hammaram Faraun Fault System, Gulf of Suez, Gawthorpe et al. (2003) found localisation to occur by several isolated faults linking together to form one basin-bounding fault. They inferred from stratigraphic relationships that the growth of the individual faults took place in a sequential manner: Faults first propagated quickly and then accumulated displacement with only minor lateral growth before linking to the next one. Oncken et al. (2012) were able to link localisation on the orogen-scale to crustal weakening. From field observations in the Andes they found simultaneous reduction of the number of active faults and decrease of convergence rate to coincide with an increase of slip rate on the remaining faults.

Taken together these observations reveal a remarkable similarity over the different scales. Ben-Zion and Sammis (2003) argued that all fault systems will evolve towards a simple, i. e. planar, structure while at the same time weakening. Any structural complexity, they state, is due to an early phase of hardening and low-slip phenomena prior to localisation. Understanding structurally complex fault networks therefore requires a close look at the early stages of fault formation and the transient processes associated with hardening – weakening. Unfortunately, these processes are too fast and too small in scale to be reconstructed in detail from the geological record. At the same time, the evolution of a fault zone lasts too long to be accessible by instrumental observation.

These restrictions can be overcome by means of analogue sandbox experiments which provide physical models that can be observed at high spatio-temporal resolution, can be repeated as required, and facilitate systematic parameter studies. For these reasons analogue sandbox experiments have been used for centuries (starting with Hall, 1815) to investigate processes that are not directly observable in nature (Brun, 1999; Dooley and Schreurs, 2012; Graveleau et al., 2012). Several successful concepts have been derived from, or at least been inspired by, analogue experiments, e. g. the critical taper theory (Davis et al., 1983) or the concept of Riedel shears (Cloos, 1928; Riedel, 1929). Observations from these models can be transferred to nature, provided that the models behave analogous to nature and are properly scaled with respect to all significant physical properties (e. g. Hubbert, 1937).

1.3 Strain Localisation in Granular Media

Sand and other granular media, when being sheared, show a distinct localisation of strain into a narrow shear zone whose width is somewhere between 10 to 20 times the mean grain diameter (e. g. Panien et al., 2006). This localisation goes along with dilation perpendicular to the shear plane and strain hardening followed by strain weakening. Once a shear zone is established, the shear stress for continued deformation remains approximately constant (Lohrmann et al., 2003). Because of these properties, and in particular because of their ability to localise strain into well defined shear zones, granular media have been used for decades as analogue materials to model a brittle, cohesion-less Earth's crust (Brun, 1999; Dooley and Schreurs, 2012; Graveleau et al., 2012). Despite this popularity, the micro-mechanical processes underlying localisation and strain weakening in granular media had not been understood until recently:

Oda and Iwashita (2000) were among the first to present a numerical code that realistically reproduces the weakening behaviour of sands by using a Distinct Element approach (DEM). They found the grains to form "column-like structures" aligned with the direction of maximum compressive stress during the hardening regime. These structures have later been termed "force chains" and found to be the load-bearing structures in granular media (e. g Mair and Hazzard, 2007; Daniels and Hayman, 2008). During weakening the particles within these structures re-organised themselves by means of rolling. Oda and Iwashita (2000) were able to change the width of the shear zones in their model by changing the particle's resistance to rolling.

Rechenmacher (2006) performed compressional tests on sand, using high-resolution Digital Image Correlation (DIC) to monitor strain evolution. She described shear band evolution as competition between conjugate shear zones: Initially multiple sets of conjugate shear bands formed (cf. Desrues and Viggiani, 2004; Dotare et al., 2016), from which later one through-going shear zone emerged while the sample weakened. Inside the shear zone Rechenmacher (2006) found patterns of alternating regions

showing either high shearing or high rotation. She interpreted these patterns as signs of re-organising force chains in accordance with the observations of Oda and Iwashita (2000). Similar results were obtained by Alonso-Marroquín et al. (2006) in a numerical model using a Cosserat-Continuum approach that includes rotation as a field variable.

Tordesillas and Muthuswamy (2009) combined all those observations into a mathematical model: Using an assembly of seven discs they were able to describe failure in granular media as the buckling of confined force chains. This had already been inferred in Oda and Iwashita (2000) and Rechenmacher (2006) but had not yet been tested. Tordesillas and Muthuswamy (2009) described failure as a process comprising several stages: first, grains along a single force chain get elastically compressed. They soon start to slightly roll around each other, causing the particles confining the force chain to slightly dilate. Due to this rolling, particles leave the centre of the force chain. This is assumed to be promoted in real sands, where force chains are rarely ideally oriented. Grains can then be squeezed out of the force chain, which happens either by sliding or continued rolling, depending on grain shape, inter-particle friction and relative orientation. Additional dilation takes place in either case.

The model of Tordesillas and Muthuswamy (2009) is able to reproduce – even for the small number of grains – many of the macroscopic characteristics previously observed in real sands, namely strain weakening, dilation during localisation and the dependency of these processes on confining pressure (Kolymbas and Wu, 1990; Desrues and Viggiani, 2004). The most important parameters in this model are inter-particle rolling- and sliding friction. For larger assemblies of grains Tordesillas and Muthuswamy (2009) assumed many force chains to buckle and fail in a coordinated manner. This was confirmed by Abedi et al. (2012), who monitored a shear zone in natural sand at grain-scale resolution. They found deformation to be mainly dilative during the beginning of weakening. During later stages they observed vortices, as proposed by Alonso-Marroquín et al. (2006), and zones of affine deformation which they interpreted to be force chains. These zones subsequently broke down simultaneously to form new vortices, in between which again new zones of affine deformation formed. The formation of vortices and force chains in these experiments went along with subtle variations in measured shear force, where vortices coincided with lower shear forces and force chains with higher ones. Abedi et al. (2012) did not observe significant amounts of sliding, a fact which they attributed to the high sliding friction of natural sand due to their rough grain surfaces.

From the above it is evident that strain localisation and strain weakening in granular media follow different micro-mechanical processes than in rock. However, they are similar in that rock as well as granular media show an initial phase of distributed deformation prior to localisation that is associated with hardening, followed by a phase of weakening during localisation. Granular materials then enter a regime of stable sliding at constant stress during which the shear zone's properties do not change (e. g. Lohrmann et al., 2003; Panien et al., 2006). This is different from rock,

in which the shear zone gradually forms a layer of fault gauge (e. g. Scholz, 2002). For investigations during the hardening-weakening phase granular materials nevertheless seem well suited.

1.4 Problem Statement and Overview of the Thesis

This thesis aims at improving the understanding of the evolution of complex, continental-scale fault networks through analogue modelling. Particular attention is paid to the mechanical evolution and the corresponding strain distribution prior to the establishment of a localised fault and their proper representation in sandbox experiments.

The thesis is composed of three independent articles intended for separate publication in scientific journals. In the first one (chapter 2), existing scaling routines for analogue sandbox experiments are critically reviewed, which leads to the conclusion that transient strength evolution is not adequately represented in the standard scaling procedures. New data are presented and a more complete scaling approach is derived, based on a quantitative comparison with natural strength data from literature. The new data reveal a scale dependence of scaling due to the transient strength evolution. The resulting limitations for analogue modelling are discussed and an unproblematic set of scaling factors for crustal scale models is recommended. This article has already been published (Ritter et al., 2016).

In the second article (chapter 3) a new experimental set-up is presented that has been developed for the purpose of conducting analogue experiments in which both stress and strain can be monitored simultaneously and at high resolution in various tectonic settings. A brief example of its capacities is given for the cases of compressional wedges and strike-slip tectonics, respectively. These experiments confirm the relationship between diffuse deformation and hardening, which on the scale of an entire wedge had previously only been inferred. Through the combined approach details of deformation can be detected, that otherwise would have remained obscured. In the strike-slip case the limitations of a classical Riedel-type set-up for analysing dynamic evolution become evident.

The findings from the previous chapters are applied in the third article (chapter 4) in a study investigating fault evolution in a network of transfer faults, using an improved strike-slip set-up. A scale dependence of transient mechanical evolution is detected and quantified in terms of energy. Its relation to the evolution of distributed deformation is established and an analogy to the development of complex fault networks in nature is drawn.

The results of the three articles are summarised in chapter 5.

References

Abedi, S., A. L. Rechenmacher and A. D. Orlando (2012): 'Vortex formation and dissolution in sheared sands'. In: *Granular Matter* 14.6, pp. 695–705. DOI: 10.1007/s10035-012-0369-5.

Alonso-Marroquín, F., I. Vardoulakis, H. J. Herrmann, D. Weatherley and P. Mora (2006): 'Effect of rolling on dissipation in fault gouges'. In: *Physical Review E* 74.3, p. 031306. DOI: 10.1103/PhysRevE.74.031306.

Ben-Zion, Y. and C. G. Sammis (2003): 'Characterization of Fault Zones'. English. In: *Pure and Applied Geophysics* 160.3, pp. 677–715. DOI: 10.1007/PL00012554.

Brace, W. F., B. W. Paulding and C. H. Scholz (1966): 'Dilatancy in the fracture of crystalline rocks'. In: *Journal of Geophysical Research* 71.16, pp. 3939–3953. DOI: 10.1029/JZ071i016p03939.

Brady, B. T., W. I. Duvall and F. G. Horino (1973): 'An experimental determination of the true uniaxial stress-strain behavior of brittle rock'. In: *Rock Mechanics Felsmechanik Mécanique des Roches* 5.2, pp. 107–120. DOI: 10.1007/BF01240161.

Brun, J.-P. (1999): 'Narrow rifts versus wide rifts: inferences for the mechanics of rifting from laboratory experiments'. In: *Philosophical Transactions of the Royal Society A: Mathematical, Physical and Engineering Sciences* 357.1753, pp. 695–712. DOI: 10.1098/rsta.1999.0349.

Cloos, H. (1928): 'Experimente zur inneren Tektonik'. In: *Centralblatt für Mineralogie, Geologie und Paläontologie*, pp. 609–621.

Cowie, P. A., J. R. Underhill, M. D. Behn, J. Lin and C. E. Gill (2005): 'Spatio-temporal evolution of strain accumulation derived from multi-scale observations of Late Jurassic rifting in the northern North Sea: A critical test of models for lithospheric extension'. English. In: *Earth and Planetary Science Letters* 234.3-4, pp. 401–419. DOI: DOI10.1016/j.epsl.2005.01.039.

Crouch, S. L. (1971): 'The post-failure behaviour of norite in triaxial compression'. In: *Engeneering Geology* 6.6, pp. 19–30. DOI: 10.1126/science.ns-5.112.260.

Daniels, K. E. and N. W. Hayman (2008): 'Force chains in seismogenic faults visualized with photoelastic granular shear experiments'. In: *Journal of Geophysical Research* 113.B11, B11411. DOI: 10.1029/2008JB005781.

Davis, D. M., J. Suppe and F. A. Dahlen (1983): *Mechanics of Fold-and-Thrust Belts and Accretionary Wedges*.

Desrues, J. and G. Viggiani (2004): 'Strain localization in sand: an overview of the experimental results obtained in Grenoble using stereophotogrammetry'. In: *International Journal for Numerical and Analytical Methods in Geomechanics* 28.4, pp. 279–321. DOI: 10.1002/nag.338.

Dooley, T. P. and G. Schreurs (2012): 'Analogue modelling of intraplate strike-slip tectonics: A review and new experimental results'. In: *Tectonophysics* 574-575, pp. 1–71. DOI: 10.1016/j.tecto.2012.05.030.

Dotare, T., Y. Yamada, J. Adam, T. Hori and H. Sakaguchi (2016): 'Initiation of a thrust fault revealed by analog experiments'. In: *Tectonophysics* 684, pp. 148–156. DOI: 10.1016/j.tecto.2015.12.023.

Gawthorpe, R. L., C. A.-L. Jackson, M. J. Young, I. R. Sharp, A. R. Moustafa and C. W. Leppard (2003): 'Normal fault growth, displacement localisation and the evolution of normal fault populations: the Hammam Faraun fault block, Suez rift, Egypt'. In: *Journal of Structural Geology* 25.6, pp. 883–895. DOI: 10.1016/S0191-8141(02)00088-3.

Graveleau, F., J. Malavieille and S. Dominguez (2012): 'Experimental modelling of orogenic wedges: A review'. In: *Tectonophysics* 538-540, pp. 1–66. DOI: 10.1016/j.tecto.2012.01.027.

Griffith, A. A. (1921): 'The Phenomena of Rupture and Flow in Solids'. In: *Philosophical Transactions of the Royal Society A: Mathematical, Physical and Engineering Sciences* 221.582-593, pp. 163–198. DOI: 10.1098/rsta.1921.0006.

Hall, J. (1815): 'On the Vertical Position and Convolutions of certain Strata, and their relation with Granite'. In: *Transactions of the Royal Society of Edinburgh* 7.01, pp. 79–108. DOI: 10.1017/S0080456800019268.

Hobbs, B. E., H.-B. Mühlhaus and A. Ord (1990): 'Instability, softening and localization of deformation'. In: *Geological Society, London, Special Publications* 54.1, pp. 143–165. DOI: 10.1144/GSL.SP.1990.054.01.15.

Holyoke, C. W. and J. Tullis (2006): 'Formation and maintenance of shear zones'. In: *Geology* 34.2, p. 105. DOI: 10.1130/G22116.1.

Hubbert, M. K. (1937): 'Theory of scale models as applied to the study of geologic structures'. In: *Bulletin of the Geological Society of America* 48, pp. 1459–1520.

Kolymbas, D. and W. Wu (1990): 'Recent results of triaxial tests with granular materials'. In: *Powder Technology* 60.2, pp. 99–119. DOI: 10.1016/0032-5910(90)80136-M.

Lockner, D. A., J. D. Byerlee, V. Kuksenko, A. Ponomarev and A. Sidorin (1992): 'Observations of Quasistatic Fault Growth from Acoustic Emissions'. In: *International Geophysics* 51.Fault Mechanics and Transport Properties of Rocks — A Festschrift in Honor of W. F. Brace, pp. 3–31. DOI: 10.1016/S0074-6142(08)62813-2.

Lohrmann, J., N. Kukowski, J. Adam and O. Oncken (2003): 'The impact of analogue material properties on the geometry, kinematics, and dynamics of convergent sand wedges'. English. In: *Journal of Structural Geology* 25.10, pp. 1691–1711. DOI: 10.1016/S0191-8141(03)00005-1.

Mair, K. and J. F. Hazzard (2007): 'Nature of stress accommodation in sheared granular material: Insights from 3D numerical modeling'. In: *Earth and Planetary Science Letters* 259.3-4, pp. 469–485. DOI: 10.1016/j.epsl.2007.05.006.

Oda, M. and K. Iwashita (2000): 'Study on couple stress and shear band development in granular media based on numerical simulation analyses'. In: *International Journal of Engineering Science* 38.15, pp. 1713–1740. DOI: 10.1016/S0020-7225(99)00132-9.

Oncken, O., D. Boutelier, G. Dresen and K. Schemmann (2012): 'Strain accumulation controls failure of a plate boundary zone: Linking deformation of the Central Andes and lithosphere mechanics'. In: *Geochemistry, Geophysics, Geosystems* 13.12. DOI: 10.1029/2012GC004280.

Orowan, E. (1949): 'Fracture and strength of solids'. In: *Reports on Progress in Physics* 12.1, p. 309. DOI: 10.1088/0034-4885/12/1/309.

Panien, M., G. Schreurs and O. A. Pfiffner (2006): 'Mechanical behaviour of granular materials used in analogue modelling: insights from grain characterisation, ring-shear tests and analogue experiments'. English. In: *Journal of Structural Geology* 28.9, pp. 1710–1724. DOI: 10.1016/j.jsg.2006.05.004.

Ramsay, J. (1980): 'Shear zone geometry: A review'. In: *Journal of Structural Geology* 2.1-2, pp. 83–99. DOI: 10.1016/0191-8141(80)90038-3.

Rechenmacher, A. L. (2006): 'Grain-scale processes governing shear band initiation and evolution in sands'. In: *Journal of the Mechanics and Physics of Solids* 54.1, pp. 22–45. DOI: 10.1016/j.jmps.2005.08.009.

Riedel, W. (1929): 'Zur Mechanik geologischer Brucherscheinungen'. In: *Centralblatt für Mineralogie, Geologie und Paläontologie*, pp. 354–368.

Ritter, M. C., K. Leever, M. Rosenau and O. Oncken (2016): 'Scaling the sandbox — Mechanical (dis-) similarities of granular materials and brittle rock'. In: *Journal of Geophysical Research: Solid Earth* 121.9, pp. 6863–6879. DOI: 10.1002/2016JB012915.

Rummel, F. and C. Fairhurst (1970): 'Determination of the post-failure behavior of brittle rock using a servo-controlled testing machine'. In: *Rock Mechanics Felsmechanik Mécanique des Roches* 2, pp. 189–204. DOI: 10.1007/BF01245574.

Scholz, C. H. (2002): *The Mechanics of Earthquakes and Faulting*. 2nd editio. Cambridge: Cambridge University Press, p. 471.

Tordesillas, A. and M. Muthuswamy (2009): 'On the modeling of confined buckling of force chains'. In: *Journal of the Mechanics and Physics of Solids* 57.4, pp. 706–727. DOI: 10.1016/j.jmps.2009.01.005.

Wawersik, W. R. and C. Fairhurst (1970): 'A study of brittle rock fracture in laboratory compression experiments'. In: *International Journal of Rock Mechanics and Mining Science and Geomechanics Abstracts* 7, pp. 561–575. DOI: 10.1016/0148-9062(70)90007-0.

2 Scaling the Sand Box – Mechanical (Dis-) Similarities of Granular Materials and Brittle Rock

Abstract

Analogue sandbox experiments are an important tool to understand brittle tectonic deformation. To date, most experiments are interpreted kinematically only. With the advent of reliable, small scale force sensors, however, their dynamic evolution becomes available for analysis, offering new insights into the transient evolution of tectonic systems. Both rock and granular materials show an evolution of strain hardening and weakening during loading in the brittle-plastic regime, but so far this similarity has only been appreciated qualitatively. As strain weakening is a vital parameter controlling fault reactivation and lifetime, it requires proper scaling.

We therefore measured and analysed two common granular analogue model materials (quartz sand and glass micro beads) using ring-shear tests at a range of normal loads typical for analogue experiments. We find two different modes of strain weakening as a function of normal load: Strain weakening at normal loads <1 kPa is due to partial loss of extrapolated cohesion, while at normal loads >1 kPa it is controlled by reduction of internal friction, which is consistent with previous measurements in this range. We show that this introduces a scale-dependence into the scaling and restricts the possible use of the tested materials to crustal scale models with a length scaling factor of $l(\frac{\text{model}}{\text{nature}}) \approx 2 \times 10^{-6}$. For these we quantitatively compare the model materials' transient strength evolution to that known from natural rock and the Earth's crust.

2.1 Introduction

Analogue models are an important tool to understand tectonic deformation. In combination with modern imaging techniques they achieve a spatio-temporal resolution

published as: M. C. Ritter et al. (2016b): 'Scaling the sandbox — Mechanical (dis-) similarities of granular materials and brittle rock'. In: *Journal of Geophysical Research: Solid Earth* 121.9, pp. 6863–6879. DOI: 10.1002/2016JB012915.

Individual Contributions: M. C. R. planned and performed research, carried out experiments and analysed results, wrote the paper; K. L. was involved in planning the research, participated in writing the paper; M. R. participated in writing the paper; O. O. was involved in planning the research, supervised the research, participated in writing the paper.

that neither natural data nor numerical models can provide (Adam et al., 2005). Most long-term models of the brittle upper crust use some kind of granular material ("sand") as a rock analogue and study its kinematic behaviour during compression (e. g. Graveleau et al., 2012), extension (e. g Brun, 1999) or strike-slip movement (e. g. Dooley and Schreurs, 2012). Some recent experiments also include force measurements in an attempt to characterise the dynamics of the model (Nieuwland et al., 2000; Cubas, Maillot et al., 2010; Cubas, Barnes et al., 2013; Herbert et al., 2015).

For the observations from any model to be representative of a natural prototype it is crucial that the model be properly scaled to nature with respect to geometry, kinematics and dynamics (Hubbert, 1937). According to this author, three fundamental scaling factors need to be defined: one each for length, mass and time, or, more commonly, length, density and gravity:

$$l^* = \frac{l_{\text{model}}}{l_{\text{nature}}},\ \rho^* = \frac{\rho_{\text{model}}}{\rho_{\text{nature}}},\ g^* = \frac{g_{\text{model}}}{g_{\text{nature}}}. \tag{2.1}$$

All other necessary scaling factors can then be calculated from these. For tectonic models the most important other scaling factor would probably be that for stress, which can be derived from eq. 2.1 as

$$\sigma^* = \rho^* g^* l^*. \tag{2.2}$$

If these scaling factors are taken care to be valid always and everywhere throughout the entire experiment, Hubbert (1937) states, scaling will be achieved. However, doing so for stress is not trivial, since it cannot be directly controlled but arises as a response of a material to the applied boundary conditions. Consequently, the material's response to boundary conditions, i. e. its rheology, must be the same as for the natural material (Weijermars and Schmeling, 1986), which for brittle prototypes means that the analogue model material must be brittle as well, and has to show the same transient strength evolution.

The common approach to achieve scaling is, apart from ensuring geometric similarity, to assume that both brittle rock and analogue material behave according to a Mohr-Coulomb failure criterion:

$$\tau = \mu\sigma_{\text{n}} + C \tag{2.3}$$

where τ and σ_{n} are the shear stress and the normal stress on a failure plane, μ is the coefficient of internal friction and C is the extrapolated cohesion. (In the following the term "cohesion" is always referring to this extrapolated cohesion unless stated otherwise. For a procedure to determine the true cohesion, see Abdelmalak et al. (2016)). Being small compared to $\mu\sigma_{\text{n}}$, C is often simply neglected for the purpose of scaling (Davy and Cobbold, 1988; Buchanan and McClay, 1991; Tron and Brun, 1991; Duerto and McClay, 2009). This conveniently results in the single scaling condition

that μ_{sand} and μ_{rock} be similar. μ_{sand} is commonly taken to be between 0.5 and 0.7 (based on e. g. Krantz (1991)), and μ_{rock} is taken to be 0.6, based on Byerlee's law (Byerlee, 1978). Consequently models are assumed to be properly scaled.

Other modellers (Gutscher et al., 1996; Cobbold et al., 2001; Galland, Cobbold et al., 2006; Rosenau et al., 2009; Burchardt and Walter, 2010; Galland, Burchardt et al., 2014; Abdelmalak et al., 2016) do scale C, using the geometry of their set-ups and the density of their model materials. They all come to the conclusion that their models are properly scaled for C_{nature} ranging somewhere from 10^5 Pa to 10^7 Pa, depending on their materials and modelled settings. According to these authors this range of values represents the natural materials in their respective cases quite well.

The major problem of this common approach is that the Mohr-Coulomb failure criterion does not account for any transient post-failure behavior of a material. This is particularly unfortunate since the post-failure phase is the one during which most significant tectonic evolution takes place. It is characterised by a loss of strength with progressive deformation known as "strain weakening", in both rock (Bieniawski et al., 1969) and sand (Kolymbas and Wu, 1990; Desrues and Viggiani, 2004). Strain weakening is assumed to be closely linked to strain localisation and fault formation. Accordingly it is an additional material property that should be properly scaled in tectonic models. Lohrmann et al. (2003) were the first to recognise this and to qualitatively compare the shapes of failure curves of natural rock and quartz sand. From measurements in a Ring-Shear tester they defined three Mohr-Coulomb-type failure envelopes for quartz sand, corresponding to the different stages during deformation: peak strength, stable strength and reactivation strength (fig. 2.2). They did not, however, quantitatively compare these strength values to those of natural materials. Panien et al. (2006) determined the same mechanical parameters for several other analogue materials, but did not relate them to natural data either. Therefore a quantitative comparison of the transient mechanical behaviour of granular analogue materials to nature is still missing to date and its scaling remains to be determined.

Another problem of the above scaling approach, although not inherent to it, is the mechanical testing of the analogue material itself. It is usually carried out at normal loads of a few kPa (Krantz, 1991; Lohrmann et al., 2003; Panien et al., 2006) to a few hundred kPa (Kolymbas and Wu, 1990). This yields linear failure envelopes for peak and stable strength that differ mainly by slope, i. e. friction coefficient. However, the overburden load at the bottom of a 5 cm thick layer of sand, which is a typical height of an analogue model, is $\rho g h \approx 1700\,\text{kg}\,\text{m}^{-3} \times 9.81\,\text{m}\,\text{s}^{-2} \times 0.05\,\text{m} = 834\,\text{Pa}$ and thus below the range of the test data. It is therefore unclear whether the data obtained in these studies are representative for the material's behaviour under model conditions.

Schellart (2000) tested different granular materials at very low normal loads (50 Pa to 900 Pa) and found that for this range the failure envelope of the peak strength shows a convex shape. He attributed the observed deviation from the linear Mohr-Coulomb envelope to a reduction of apparent cohesion. Stable strength and weakening were not measured in this study, owing to the nature of the experimental device used.

The data in Schellart (2000), as well as in Krantz (1991) and most of Lohrmann et al. (2003), have been obtained using a so-called "Hubbert-type" shear box. This device consists of two cylinders of equal diameter that are placed above each other with a thin gap in between. They are filled with the tested material; then the upper one is moved laterally, thereby shearing the material at the transition between the cylinders. Its strength can be calculated from the contact area between the two cylinders and the force required to move the upper cylinder. There are some issues with this approach, though, the main one being that the shear zone does not necessarily remain between the cylinders as a plane feature. For small thicknesses of the layer above the shear zone ($h < \frac{r}{3}$, where r is the radius of the cylinder) it may bend upwards (Schellart, 2000) or even evolve into a thrust cross-cutting the sample. Obviously, this would bias the results. Schellart (2000) provides a detailed discussion of possible sources of error related to the Hubbert-type apparatus.

In this study we aim to address the issues mentioned above: We first create a set of mechanical data for two common analogue materials, that covers the entire range of relevant normal loads and is large enough to account for statistical variability. We do this through measurements with a Ring-Shear tester (Schulze, 1994) that due to its design avoids the problems of the Hubbert-type apparatus. We then quantitatively compare this data set to natural data to assess the analogue materials' suitability for tectonic modelling, taking into account the transient material behaviour during failure.

2.2 Materials and Methods

We use two granular materials that are both commonly applied in analogue modelling: quartz sand and glass beads. The quartz sand (type G23T) is a moderately sorted, medium-grained fluvial sand, with rounded grains and a mean grain size of 300 µm. It is the standard sand used for analogue modelling at GFZ Potsdam and represents a rather coarse variant of sands used by the analogue modelling community. However, friction and cohesion values are similar to sands from other laboratories (Klinkmüller, Schreurs, Rosenau and Kemnitz, 2016). The glass beads are an artificial product. They are nearly perfectly rounded and very well sorted, with a grain size distribution ranging from 100 µm to 200 µm and a mean grain size of 175 µm. They represent rather fine-grained and low friction and cohesion material compared to commonly used sands (Klinkmüller, Schreurs, Rosenau and Kemnitz, 2016).

Measurements are carried out in the Ring-Shear tester RST-01.pc (Schulze, 1994) which has also been used by Lohrmann et al. (2003) and Panien et al. (2006). It consists of an annular shear cell containing the sample (inner radius: 5 cm, outer radius: 10 cm, height: 4 cm), and a lid that is pressed onto the sample at a preset normal load which is kept constant throughout an experiment (fig. 2.1). The shear cell is rotated while the lid is kept in place. Closely spaced radial blades pointing

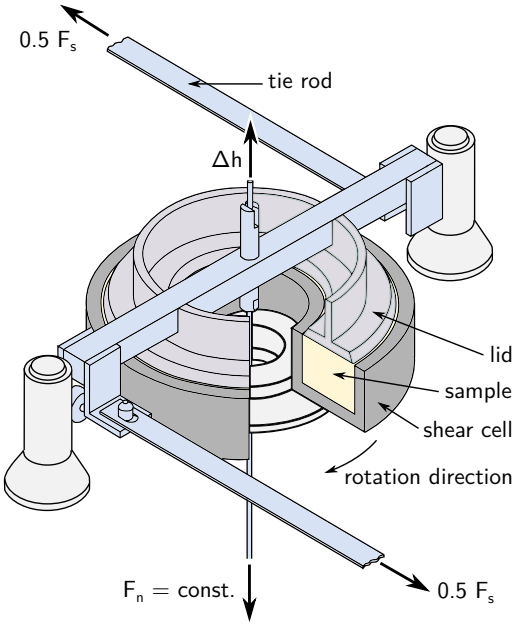

Fig. 2.1: Sketch of the Ring-Shear tester. The material is sifted into the shear cell, then the lid is placed on top of it and a constant normal load F_n is applied through a weight. The cell is then rotated, while the lid is kept in place by tie rods. Due to this differential movement between shear cell and lid a shear zone forms within a sample. Force sensors register the shearing force F_s, which can be transformed into shear stress within the sample using the known geometry of the device. Dilation of the sample is measured as the vertical movement Δh of the lid. Modified from Schulze (1994).

vertically downward from the lid (distance: 17.9 mm at inner edge, 30.2 mm at outer edge; height: 5 mm, thickness: 0.9 mm) ensure that it is mechanically coupled with the sample, such that all relative displacement between lid and shear cell must be taken up by the sample. Sensors at the lid record the torque transferred from the shear cell via the sample to the lid, as well as the lid's vertical movement which is equivalent to the sample dilation. Knowing the geometry of the device one can transform the torque measurements into shear stress (τ) and the rotation into displacement, and plot those as shear curves (fig. 2.2). This device has been benchmarked using a certified standard bulk material (limestone powder CRM-116) and the results have been found to be consistent with those of a Jenike shear cell (Schulze, 1994). The Jenike shear cell is mechanically equivalent to the Hubbert-type shear box that is commonly applied in the analogue modelling community.

At the onset of deformation shear stress first increases quickly to a maximum τ_p and then drops to a stable value τ_s, which it retains for the rest of the deformation. When deformation is stopped, the sample unloaded and subsequently deformation is resumed, another stress peak occurs which is called reactivation strength τ_r. It is usually somewhat smaller than τ_p. Detailed inspection of fig. 2.2 reveals that the stable value is actually slightly increasing. This is an artefact of the set-up and due to the fact that the lid of the shear cell slowly burrows into the material upon continued shearing, thereby increasing the friction at its side walls. It causes a tendency to overestimate τ_r. For exact an determination of the reactivation stress this should be corrected for using the measurement of the vertical displacement of the lid. The

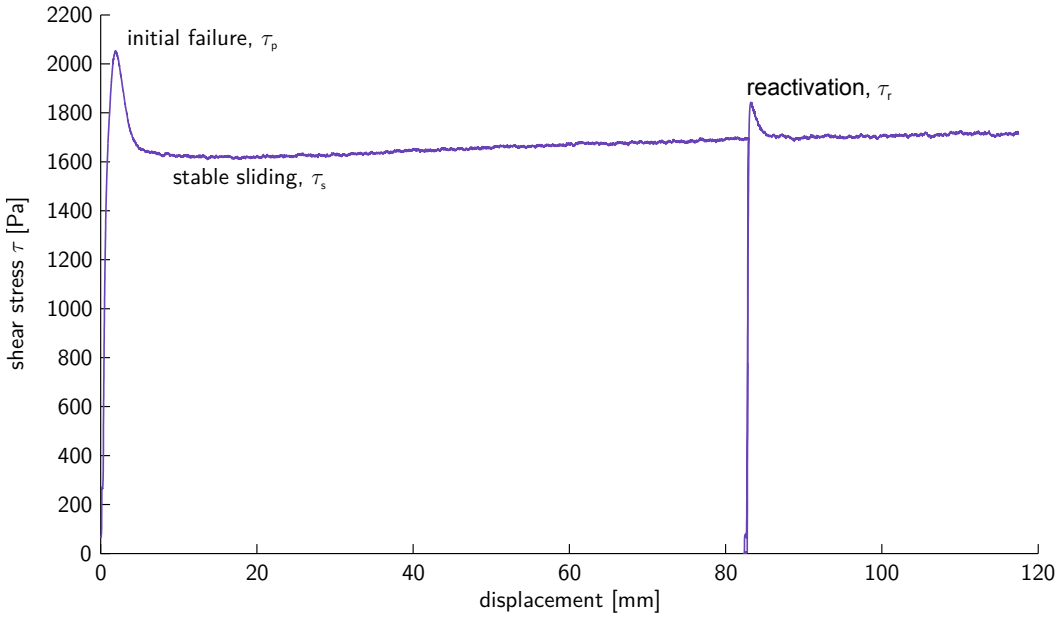

Fig. 2.2: Characteristic shear stress – displacement curve (shear curve) for quartz sand at $\sigma_n = 3\,\text{kPa}$, obtained using the Ring-Shear tester (RST). Strain localisation into a discrete shear zone is associated with a peak in the diagram due to hardening and subsequent weakening (initial failure, τ_p). Smaller hardening – weakening precedes reactivation (τ_r). The horizontal part of the curve is associated with stable sliding on the shear zone (τ_s). The slight increase is due to the lid of the shear cell burrowing slowly into the material.

three stress values were automatically picked from the shear curves and form the base of the following analysis, in which we will concentrate on τ_p and τ_s, and report the values of τ_r merely for the sake of completeness. The automatic picking algorithm finds the two maxima of the shear curves, which are τ_p and τ_r, and then finds the minimum in between the two peaks, which is τ_s. The unloading phase is detected via the rotation velocity and masked out prior to determining the peaks.

Samples were sifted into the shear cell to achieve high compaction (Krantz, 1991), and measurements were carried out for different normal loads ranging from 125 Pa to 4000 Pa, repeating them eight to ten times per normal load. Samples measured at normal loads below 500 Pa were pre-loaded at 500 Pa to make sure the blades were fully immersed in the sand and the lid was in close contact with the sample. Preliminary tests at a normal load of 300 Pa have shown that this does not affect the strength.

2.3 Results

In total 102 measurements were carried out for quartz sand and 83 for glass beads. The complete shear curves for all of them are available in the supplementary data publication of Ritter et al. (2016a). In the following we use only τ_p, τ_s and τ_r derived from the shear curves. We divide them in two data sets, one containing all measurements for quartz sand and one for those of glass beads. Both data sets show an approximately linear increase of all three values with σ_n, and neither shows the convex shape of the failure envelope observed by Schellart (2000) for low σ_n (fig. 2.3 A, B). This is consistent with a Mohr-Coulomb failure criterion. The strength of the quartz sand is generally higher than that of the glass beads. In order to quantify the strength drop from τ_p to τ_s we define the relative weakening $\Delta\tau$ as

$$\Delta\tau = 1 - \frac{\tau_\mathrm{s}}{\tau_\mathrm{p}} = 1 - \frac{\mu_\mathrm{s}\sigma_\mathrm{n} + C_\mathrm{s}}{\mu_\mathrm{p}\sigma_\mathrm{n} + C_\mathrm{p}}. \tag{2.4}$$

This value will be between zero (no weakening) and one (no residual strength). For high normal loads it will be dominated by μ and converge towards $1 - \frac{\mu_\mathrm{s}}{\mu_\mathrm{p}}$, whereas for normal loads approaching zero it will be dominated by C and converge towards $1 - \frac{C_\mathrm{s}}{C_\mathrm{p}}$. Fig. 2.3 (C, D) shows $\Delta\tau$ for both data sets. In either case $\Delta\tau$ is highest (about 0.35) for low normal loads, decreases towards a minimum of about 0.1 at $\sigma_\mathrm{n} \approx 1\,\mathrm{kPa}$ and then reaches a stable value of roughly 0.2 at high normal loads. This shape is inconsistent with the assumption of linear τ and positive σ_n, for which, according to the definition in eq. 2.4, $\Delta\tau$ should be monotonic: If $\tau_\mathrm{s,p}$ are simple linear functions (eq. 2.3), they are differentiable. Thus $\Delta\tau$ is differentiable as well. It has a pole for $\tau_\mathrm{p} = 0$ and no other extremum. This can be verified by setting

$$\frac{\partial\Delta\tau}{\partial\sigma_\mathrm{n}} = \frac{\mu_\mathrm{p}C_\mathrm{s} - \mu_\mathrm{s}C_\mathrm{p}}{\tau_\mathrm{p}^2} \equiv 0 \tag{2.5}$$

which yields no solution for σ_n, except for the case of $\mu_\mathrm{p}C_\mathrm{s} - \mu_\mathrm{s}C_\mathrm{p} = 0$, in which it becomes true for any σ_n. For physical reasons $\tau_\mathrm{p} > 0$ for $\sigma_\mathrm{n} \in (0, \infty)$ and thus $\Delta\tau$ must be monotonic in this interval.

We therefore divide both data sets at their respective minimua of $\Delta\tau$ in two subsets, such that each subset individually satisfies this criterion. The "low-load" subsets comprise all measurements of the respective material for which $\sigma_\mathrm{n} \leq 1\,\mathrm{kPa}$ and the "high-load" subsets all those for which $\sigma_\mathrm{n} \geq 1\,\mathrm{kPa}$. For each subset a linear least squares algorithm is applied to find the best fitting Mohr-Coulomb failure envelope (eq. 2.3). The fitting parameters μ and C for each subset are listed in tab. 2.1.

The high-load subsets (fig. 2.4 (A, B)) show similar characteristics as observed in previous studies (Mandl et al., 1977; Lohrmann et al., 2003; Panien et al., 2006): The failure envelopes for peak, stable and reactivation strength diverge, with friction

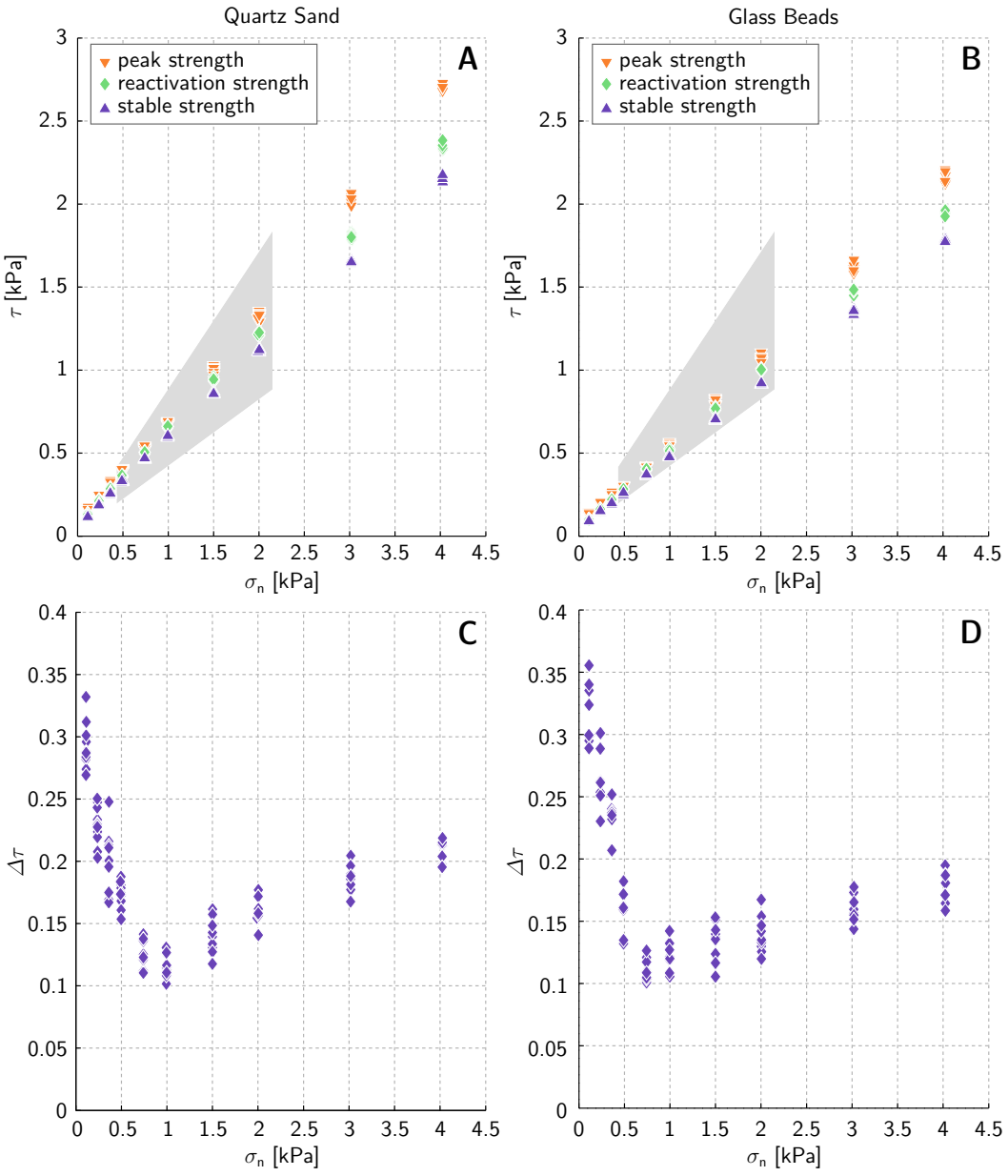

Fig. 2.3: Shear strength as function of normal load of quartz sand (**A**) and glass beads (**B**), measured with the Ring-Shear tester (raw data in Ritter et al. (2016a)). The data show a linear increase with normal load, which is consistent with the assumption of a Mohr-Coulomb failure criterion. The strength of quartz sand is generally higher than that of glass beads, and the peak strength of each material shows a higher slope than the respective stable and reactivation strengths. The grey patch shows the range of other common analogue model materials (Klinkmüller, Schreurs and Rosenau, 2016). (**C**) and (**D**): Relative weakening $\Delta\tau = 1 - \frac{\tau_s}{\tau_p}$ as function of normal load of quartz sand and glass beads. Neither of the data sets show the monotonic behaviour expected from the definition of $\Delta\tau$ and linear failure envelopes.

Tab. 2.1: Mechanical properties of the investigated materials, as determined by linear least squares fitting of τ_p, τ_r and τ_s at different normal loads. The numbers in parentheses are the numerical values of measurement uncertainty, calculated as twice the standard deviation of the respective fit parameter and referred to the corresponding last digits of the result.

	μ_p	C_p [Pa]	μ_r	C_r [Pa]	μ_s	C_s [Pa]
quartz sand, $\sigma_n \geq 1\,\mathrm{kPa}$	0.672(5)	0(13)	0.562(4)	101(9)	0.524(3)	91(6)
quartz sand, $\sigma_n \leq 1\,\mathrm{kPa}$	0.576(7)	110(4)	0.591(4)	70(2)	0.546(3)	60(2)
glass beads, $\sigma_n \geq 1\,\mathrm{kPa}$	0.536(7)	0(17)	0.471(3)	58(6)	0.429(2)	57(4)
glass beads, $\sigma_n \leq 1\,\mathrm{kPa}$	0.459(9)	85(5)	0.478(3)	47(2)	0.443(4)	40(3)

coefficients of $\mu_p \approx 0.7$ and $\mu_s \approx 0.5$ for quartz sand, and $\mu_p \approx 0.5$ and $\mu_s \approx 0.4$ for glass beads. $\Delta\tau$ is similar for both materials and increases from 0.1 to 0.2 over the range of the subset (fig. 2.4 (C, D)). This increase is mainly due to $C_p \ll C_s$ for both materials, which makes the derivative in eq. 2.5 positive.

This is remarkably different for the low-load subsets (fig. 2.5 (A, B)). Here peak friction coefficients are significantly lower than in the high-load subset, particularly for the quartz sand. At the same time, friction coefficients for reactivation and stable strength remain approximately constant. This results in the failure envelopes of peak and stable strength being almost parallel. Consequently, the weakening is mainly controlled by cohesion, which shows an offset of about 50 Pa between peak and stable strength for both materials. According to eq. 2.5 this results in decreasing $\Delta\tau$. It starts around 0.3 to 0.35 for $\sigma_n = 125\,\mathrm{Pa}$ and decreases to 0.1 to 0.15 for $\sigma_n = 1000\,\mathrm{Pa}$ (fig. 2.5 (C, D)). It is slightly higher in glass beads than in quartz sand owing to the quartz sand's higher peak strength.

2.4 Discussion

2.4.1 Validation of Measurements

Deformation in the Ring-Shear tester used in this study is in general similar to that in the Hubbert-type shear box. As a main difference there is not one single back wall at which failure initiates – as in the Hubbert-type apparatus – but several blades at each of which a small shear zone initiates and propagates to link up with the next shear zone at the next blade. Conceptually, the Ring-Shear tester can be regarded as a series of small scale Hubbert-type shear boxes that are each bounded by two adjacent blades. Therefore, the measured shear stress is averaged over several developing shear zones, which makes the results more stable. The mechanical processes within the sample, however, are the same.

The data set we have obtained in our measurements spans a wider range of normal load conditions than any previous study: Lohrmann et al. (2003) measured quartz sand similar to ours (their sands "SIC2" and "SHC") at normal load conditions

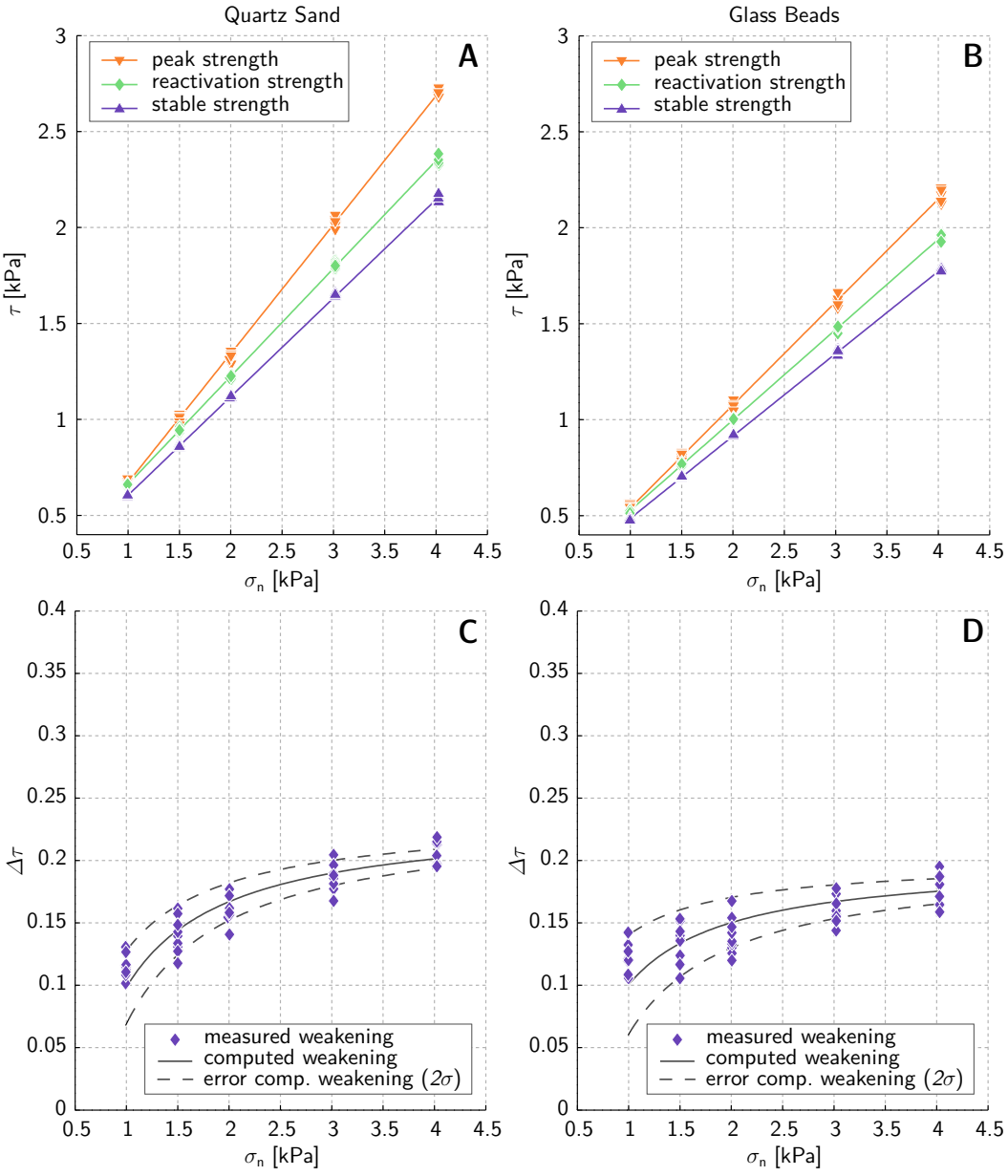

Fig. 2.4: Shear strength as a function of normal load for the high-load subset of quartz sand (**A**) and glass beads (**B**). The lines represent Mohr-Coulomb failure envelopes fitted by means of a linear least squares algorithm. The three failure envelopes for each material diverge, indicating a weakening mechanism controlled by reduction of internal friction. (**C**) and (**D**): Relative weakening $\Delta\tau = 1 - \frac{\tau_s}{\tau_p}$ as function of normal load for quartz sand and glass beads in the high-load subset. For both materials is $\Delta\tau$ is slightly increasing with σ_n. The computed weakening is the result of inserting the equations of the fitted failure envelopes into eq. 2.4.

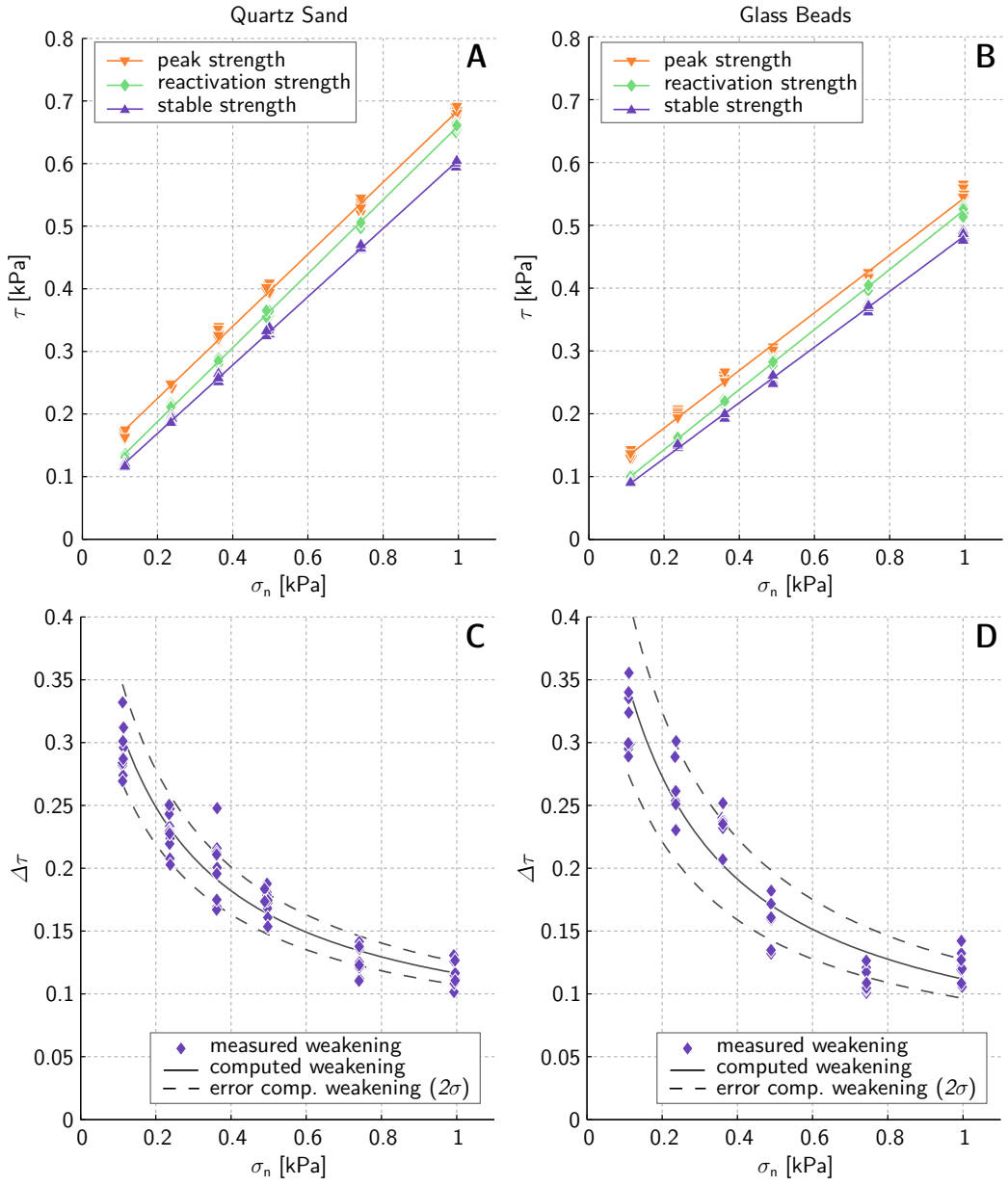

Fig. 2.5: Low-load subset: Shear strength as a function of normal load of quartz sand (**A**) and glass beads (**B**). The lines represent Mohr-Coulomb failure envelopes fitted in a linear least squares sense. Peak friction is much lower than in the high-load subset, especially for quartz sand. This results in the failure envelopes of peak and stable strength being almost parallel, which indicates a weakening mechanism controlled by reduction of cohesion rather than internal friction. (**C**) and (**D**): Relative weakening $\Delta\tau = 1 - \frac{\tau_s}{\tau_p}$ is decreasing with σ_n for both quartz sand and glass beads. Values for glass beads are slightly higher than for quartz sand, due to the glass beads' lower peak strength.

corresponding to our high-load range. Friction coefficients and cohesion they derive for peak and reactivation show the same trend and very similar values as ours. Since they used a Hubbert-type shear box, they could not measure weakening as we define it. Panien et al. (2006) carried out Ring-Shear measurements on several granular materials and determined also the relative weakening. In the high-load range, in which they measured, they find the same slightly increasing trend of the relative weakening as we do (fig. 2.4 (C, D); their fig. 3). Klinkmüller, Schreurs, Rosenau and Kemnitz (2016) measured various materials at normal loads ranging from 430 Pa to 2150 Pa, among them also those used in this study. They used the same ring-shear tester as we did and found friction coefficients that match those of our high-load subset quite well. Their range of normal loads overlaps slightly with our low-load subset, however, they do not report the increase of weakening we observe for low normal loads. The good agreement of the parameters measured in those previous studies with our measurements validates our results for the high-load subset. For the low load subset validation is not possible because of a lack of data in this range.

The only measurements carried out at low normal loads that we are aware of are those of Schellart (2000) and Mechelen (2004). The latter study measured internal friction and cohesion of different sands and glass beads (wet and dry) at normal loads between 200 Pa to 1000 Pa. However, the results are not directly comparable to ours since the materials used are different, and the study of Mechelen (2004) concentrates on low normal loads and could thus not have found the transition to the high-load regime.

Schellart (2000) reports peak strengths of several granular materials for normal loads matching our low-load subset and below, which he measured in a Hubbert-type apparatus. He observed a convex shape of the failure envelope for very low normal loads below 300 Pa, which is not visible in our data. It is possible, however, that this convex shape does also exist in our materials, but only occurs for lower normal loads than we were able to measure.

2.4.2 Consequences for Scaling

In the common scaling approach in tectonic modelling – as described above – the influence of cohesion C is often neglected. Strength in that case only depends on normal load through a constant factor, the friction coefficient. Since strength and normal load both scale as stresses, it is then assumed that strength is properly scaled as long as friction is the same and normal load is scaled, independently of the actual dimensions of the model. Granular materials have been used accordingly to model processes at scales ranging from basin- or accretionary wedge-scale (McClay, 1990), over crustal- or orogenic wedge-scale (Leever et al., 2011; Graveleau et al., 2012) up to even lithospheric scale (Davy and Cobbold, 1988; Luth et al., 2013). Our results, on the contrary, show that for the dimensions of typical analogue models the weakening of granular materials is controlled by cohesion. As a consequence, cohesion should

be taken into account for the scaling of processes in which weakening is important. This renders the initial assumption invalid and introduces a scale-dependence of the material strength which is likely to restrict the possible uses of analogue materials to only some of the above processes. Other models already include cohesion in the scaling, e. g. Galland, Cobbold et al. (2006), Holohan et al. (2013) and Abdelmalak et al. (2016). However, in these studies weakening is usually not considered.

In order to derive dynamic scaling of an analogue material, one has to determine the strength of the natural prototype first. Lohrmann et al. (2003) and Panien et al. (2006) used laboratory-derived rock failure strengths for a qualitative comparison to analogue material strengths, suggesting different analogue materials to model different rock types. This implies the assumption that the strength of small rock samples under laboratory conditions correctly reflects rock strength on a larger, natural scale, and although it is rarely stated explicitly this assumption can be found quite often in the analogue modelling literature.

Studies on crustal rheology, on the other hand, usually assume the brittle part of the crust to be best described by Byerlee's law (Byerlee, 1978; Brace and Kohlstedt, 1980; Bürgmann and Dresen, 2008), which is an empirical law that describes the onset of sliding in a pre-cut, laboratory-scale rock sample under shear stress as a function of normal load. This assumption is based on hydro-fracturing experiments in deep boreholes, which measure crustal fracture strength on a km-scale and consistently find friction coefficients between 0.6 and 1 in most locations (Brudy et al., 1997; Townend and Zoback, 2000), which are the same values as given by Byerlee's law. It is commonly explained by fractures cross-cutting the upper crust in all directions, such that its strength will be determined by the reactivation of these fractures and not the fracturing of intact rock, if a large enough volume of rock is considered (Brace and Kohlstedt, 1980).

Depending on the situation and processes modelled either of these two assumptions might be better suited. In the following, we analyse both and determine to which extent and at what scales our model materials correctly mimic the assumed natural behaviour for each. In either case we define the natural processes to be represented by the analogue material's peak and stable strength and then try to determine suitable scaling parameters by trial-and-error and simple comparisons. Prior to this, we analyse the influence of the weakening mode (by reduction of cohesion or friction).

Influence of Weakening

Strain weakening is crucial to maintain activity of a shear zone and to facilitate its reactivation: With progressing deformation a shear zone often rotates away from the initial, ideal orientation. The weakening determines how long it can still remain active, i. e. how much it can rotate until formation of a new shear zone will be mechanically more favourable than continuing activity on the existing one ("maximum rotation angle"). This can be illustrated in a Mohr-Coulomb diagram (Scholz, 2002).

Fig. 2.6 A shows this for a hypothetical material that weakens by reduction of friction, as commonly assumed for analogue materials. In this case the absolute weakening increases with normal load, but the relative weakening remains constant. The slopes of the failure envelopes (μ) depicted are the same as we measured for quartz sand at high normal loads, but cohesion (C) is set to zero for simplicity. As can be seen from the diagram, the maximum rotation angle is independent of normal stress and always $-18°$ to $13°$ around the dynamically ideal orientation (where the negative sign refers to clockwise rotation in the Mohr-Coulomb diagram).

Fig. 2.6 B shows the same Mohr-Circle construction for a material similar to quartz sand in the low-load regime, with $\mu = 0.57$ and cohesion $C_\mathrm{p} = 110\,\mathrm{Pa}$ and $C_\mathrm{s} = 60\,\mathrm{Pa}$ for peak and stable strength, respectively. In this case, that is representative for the situation in sand-box models, absolute weakening is constant, but relative weakening decreases with increasing normal load. Consequently, the range of orientations facilitating continued shear zone activity decreases with increasing normal load. The two Mohr-Circles shown represent the overburden stress at the base of a 1 cm thick and a 4 cm thick layer of sand. For an overburden of 1 cm sand shear zones may rotate $\pm 15°$ and remain active. For an overburden of 4 cm only $\pm 10°$ of rotation are possible. These angles can be geometrically related to the distance between the failure envelopes at the point of failure and thus to the relative weakening. A similar construction could be carried out for the reactivation strength.

The cases described above are idealised, since for real sand the cohesion in the high-load regime is not exactly zero and friction coefficients in the low-load regime are not exactly the same. Nevertheless, the general trend remains and shows a minimum range of possible shear zone rotation for continued activity at layer thicknesses of around 5 cm. This variable range has implications for any model in which strain is accommodated on networks of faults, in which partitioning of slip on individual structures is controlled by their potential for continued activity or reactivation. A narrower range of allowed shear zone rotation (i. e. smaller relative weakening) results in a shorter lifetime of shear zones and thus in more shear zones to be formed during a certain amount of time. Therefore special care must be taken to properly scale the relative weakening and thereby the range of shear zone activity.

Comparison to Intact Rock

The rock failure data used to compare our measured data to were compiled from literature. Al-Ajmi and Zimmerman (2005) provided data in numerical form, all other data have been digitised from published plots. In Byerlee (1975) they were given in terms of stresses at failure, whereas Byerlee (1968), Bieniawski et al. (1969), Crouch (1970, 1971) and Wawersik and Fairhurst (1970) provided characteristic failure curves from which the stresses at failure were picked by hand. All data were given in terms of principal stresses σ_1 and σ_3. Fig. 2.7 A shows the failure strength as differential stress ($\sigma_1 - \sigma_3$) versus confining pressure (σ_3). This figure shows a

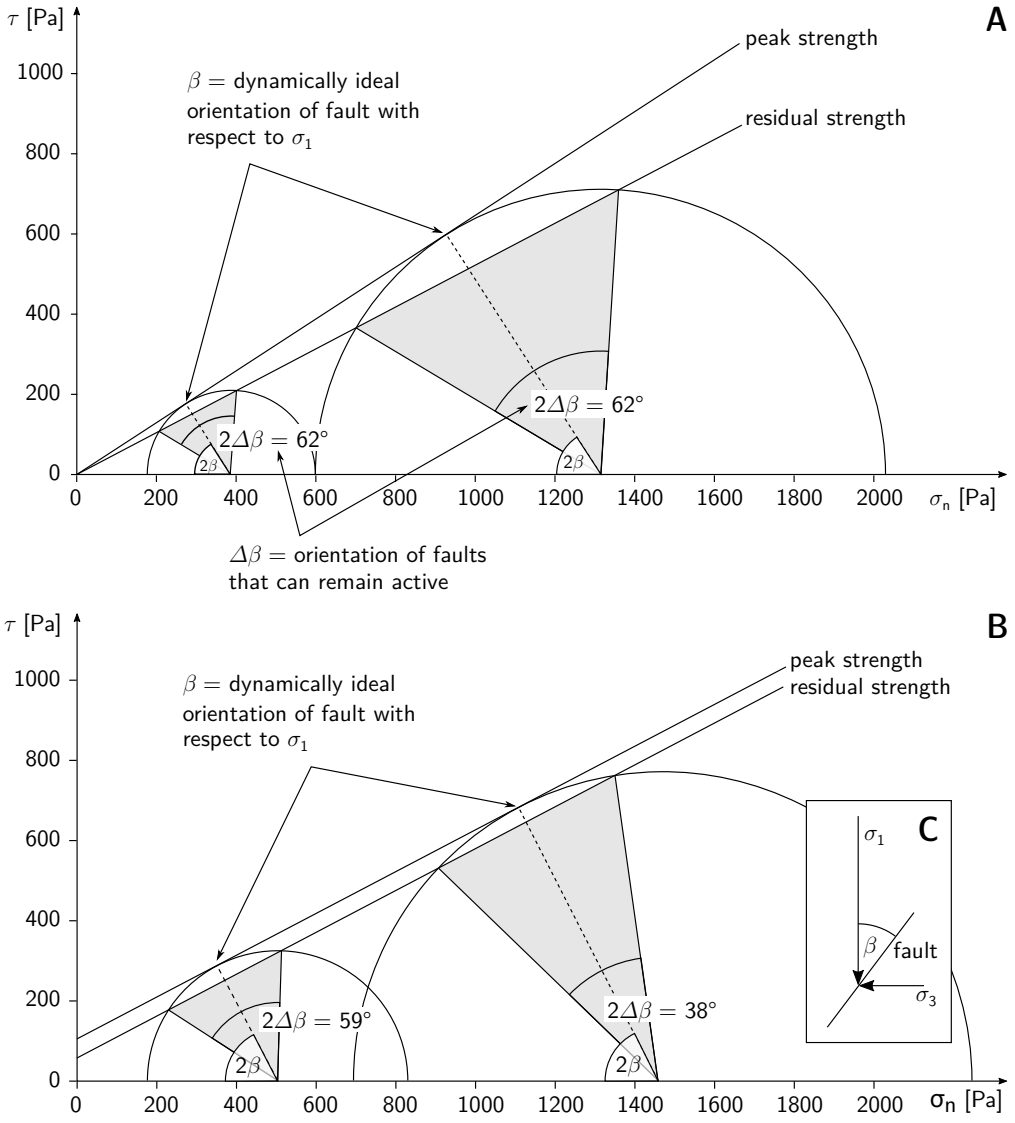

Fig. 2.6: Mohr-Circle constructions showing the influence of weakening on shear zone activity for **A:** a material that weakens by reduction of friction ($\mu_\mathrm{p} = 0.67$, $\mu_\mathrm{s} = 0.52$, $C = 0$; similar to quartz sand under high-load conditions), and **B:** a material that weakens by partial loss of cohesion ($\mu_\mathrm{p} = \mu_\mathrm{s} = 0.57$, $C_\mathrm{p} = 110\,\mathrm{Pa}$, $C_\mathrm{s} = 60\,\mathrm{Pa}$; similar to quartz sand under loading conditions relevant for analogue models). In **A** the relative weakening is constant which results in a constant range of fault orientations, $\Delta\beta$, that can remain active ("maximum rotation angle"). In **B** relative weakening decreases with increasing normal load and so does $\Delta\theta$. The Mohr-Circles show the state of stress at the base of a 1 cm and a 4 cm thick layer of sand, respectively. Both cases are idealised to emphasise the principal behaviour. Inset **C** shows the definition of β. Please note that angles are doubled in Mohr-space.

Tab. 2.2: Mechanical fit parameters of the different rock types used in this study. All numbers refer to peak strength τ_p.

rock type	q	C_0 [MPa]	ϕ [°]	μ	C [MPa]
Oak Hall limestone[1]	2.63	417	26.7	0.503	128
marble[2]	2.98	136	29.8	0.574	39
norite[3]	7.78	279	50.6	1.216	50
norite[4]	11.85	278	57.6	1.575	40
quartzite[5]	12.69	246	58.6	1.641	34
Weber sandstone A[6]	3.23	227	31.8	0.620	63
Weber sandstone B[6]	4.09	217	37.4	0.764	54
Weber sandstone C[6]	4.09	285	37.4	0.764	70
marble[7]	4.23	52.7	38.1	0.785	13
Dunham dolomite [7]	3.66	299	34.8	0.696	78
KTB amphibolite[7]	6.44	220	47.0	1.072	43
Shirahama sandstone[7]	2.31	124	23.4	0.432	41
Solnhofen limestone[7]	2.09	358	20.7	0.378	124
Westerly granite[7]	8.17	250	51.4	1.254	44

(1) Byerlee (1968), (2) Wawersik and Fairhurst (1970), (3) Crouch (1971), (4) Bieniawski et al. (1969), (5) Crouch (1970), (6) Byerlee (1975), (7) Al-Ajmi and Zimmerman (2005)

reasonably good linear correlation for the individual rock types. Therefore a linear Mohr-Coulomb failure criterion can be fitted to each rock data set. In (σ_1, σ_3) - space this takes the form (Jaeger et al., 2007):

$$\sigma_1 = q\sigma_3 + C_0 \tag{2.6}$$

where the parameters q and C_0 can be related to the angle of internal friction ϕ and the cohesion C as

$$q = \frac{1 + \sin\phi}{1 - \sin\phi} \tag{2.7}$$

$$C_0 = 2C\frac{\cos\phi}{1 - \sin\phi}. \tag{2.8}$$

Using these relations, the angle β between σ_1 and the failure plane, i. e. τ, can be calculated (Jaeger et al., 2007):

$$\beta = 45° - \frac{1}{2}\phi \tag{2.9}$$

By constructing the principal stress tensor and rotating it by β each data point can individually be transformed from (σ_1, σ_3) - space to (τ, σ_n) - space in order to use the same coordinate system for all data, rock and sand. The rock fitting parameters for either coordinate system can be found in tab. 2.2.

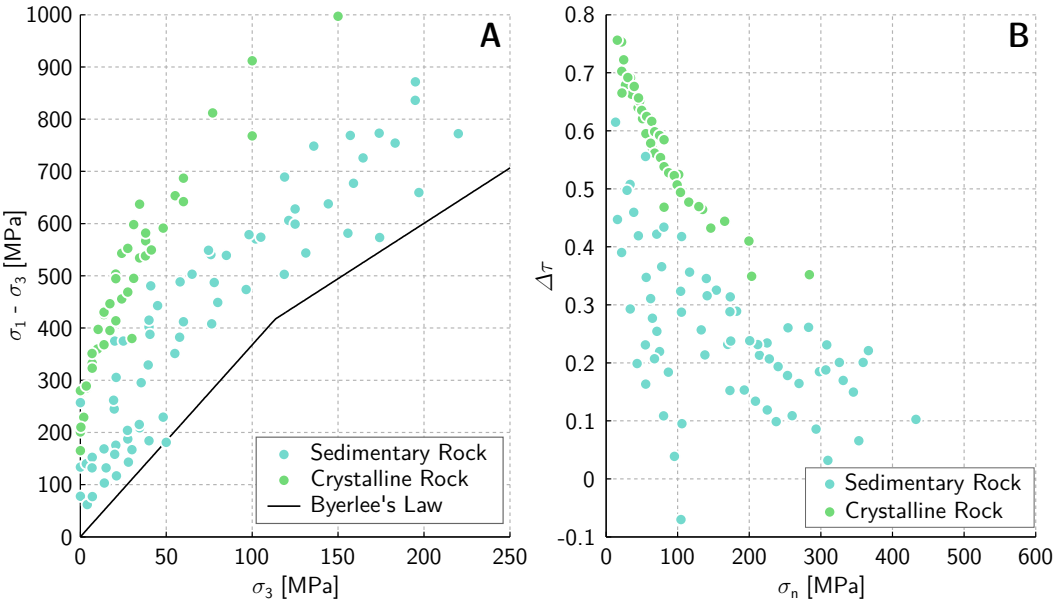

Fig. 2.7: A: Stress at failure for several types of rock in drained biaxial testing at different confining pressures. The solid line marks Byerlee's empirical law (Byerlee, 1978) for initiation of sliding on pre-cut (failed) rock. **B:** Relative weakening $\Delta\tau$ of rock, assuming Byerlee's law (Byerlee, 1978) as the representation of the weakened shear stress τ_s. Note that this is only an upper bound approximation for τ_s, real $\Delta\tau$ will in fact be larger. All data are rotated into (σ_n, τ)-space using the friction angles ϕ given in tab. 2.2. All data are compiled from literature.

Tab. 2.3: Scaling factors for different applications of sandbox models, (H) = hydrostatic pore fluid pressure, (L) = lithostatic confining pressure. l thickness of modelled domain, $\Delta\rho$ density reduced by density of pore fluid, σ stress. g^*, the factor for scaling the acceleration due to gravity, equals 1 in all cases.

Scale	l_{nature} [km]	l_{model} [cm]	$\Delta\rho_{\text{nature}}$ [kg m^{-3}]	$\Delta\rho_{\text{model}}$ [kg m^{-3}]	l^* $\times 10^{-6}$	ρ^*	σ^* $\times 10^{-6}$
Crust (H)	25	5	1800	1700	2	0.94	1.89
Crust (L)	25	5	2800	1700	2	0.61	1.21
Basin (H)	10	10	1400	1700	10	1.21	12.1
Basin (L)	10	10	2400	1700	10	0.71	7.08
Lithosphere (H)	20	1	1800	1700	0.5	0.94	0.472
Lithosphere (L)	20	1	2800	1700	0.5	0.61	0.304

Because of technical issues related to the high stiffness of rock, which is similar to that of common rock-testing machines (Cook, 1965; Wawersik and Fairhurst, 1970), practically no complete stress-strain curves including the stable sliding regime are available for rock. Instead we use Byerlee's empirical law as an estimate for the stable strength. It states that peak shear stress for sliding on a pre-existing fracture plane is independent of rock type and follows (Byerlee, 1978):

$$\begin{aligned} \tau &= 0.85\,\sigma_{\text{n}} && \text{for } \sigma_{\text{n}} \leq 200\,\text{MPa and} \\ \tau &= 0.6\,\sigma_{\text{n}} + 50\,\text{MPa} && \text{for } \sigma_{\text{n}} \geq 200\,\text{MPa}. \end{aligned} \tag{2.10}$$

This corresponds to the reactivation stress τ_{r} as measured in the Ring-Shear tester and can serve as an upper bound for τ_{s} only; however, it is the best approximation available. Byerlee's law is shown in fig. 2.7 A as a black line. Fig. 2.7 B shows the relative weakening $\Delta\tau$ for the different rock types assuming Byerlee's law as describing the weakened state. $\Delta\tau$ shows a strong decrease from about 75 % for very low σ_{n} to 5 % to 35 % for $\sigma_{\text{n}} \approx 400$ MPa. Due to the upper-bound approximation for τ_{s}, these values will be *lower*-bound approximations for $\Delta\tau$. For $\sigma_{\text{n}} = 0$ $\Delta\tau$ will be equal to 100 % for any rock, due to the definition of Byerlee's law.

Crustal Scale A common length scale for modelling processes involving the entire brittle crust, such as formation of orogenic wedges, is $l^* = 2 \times 10^{-6}$, translating to a model thickness of 5 cm for a brittle crust of 25 km. From eq. 2.2 and assuming $\rho_{\text{model}} = 1700\,\text{kg m}^{-3}$ and $\rho_{\text{nature}} = 2800\,\text{kg m}^{-3}$ this results in a stress scale $\sigma^* = 1.214 \times 10^{-6}$ (see tab. 2.3). The data from the Ring-Shear tester are scaled up using this factor and the rock data are transformed into $(\tau, \sigma_{\text{n}})$-space as described above and using the parameters listed in tab. 2.2. The result is shown in fig. 2.8 A.

The peak strength of quartz sand plots in the lower range of the rock failure data and more or less parallel to it. The stable strength of quartz sand plots below and

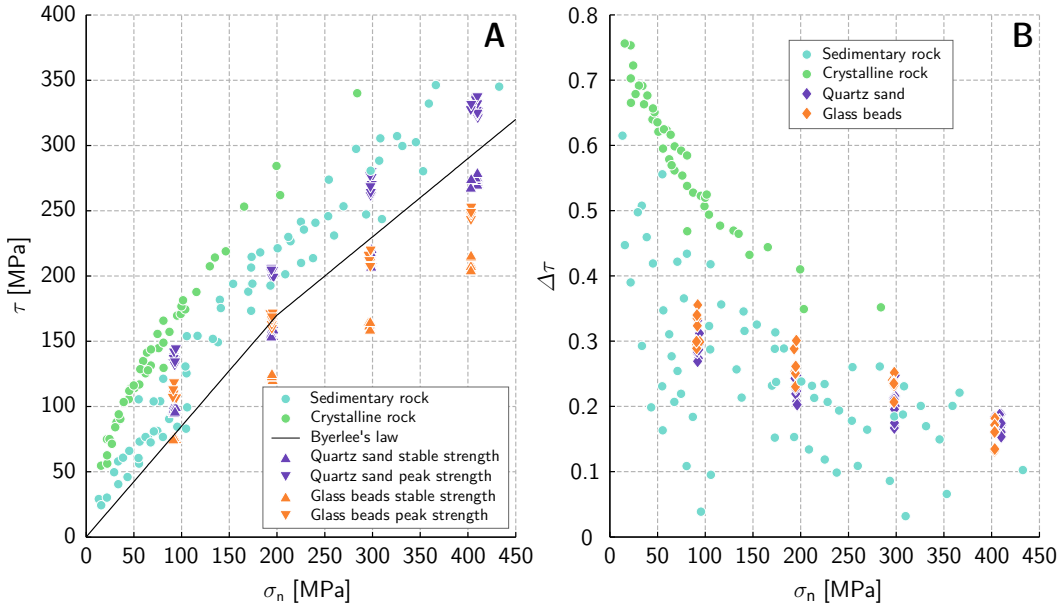

Fig. 2.8: A: Failure of natural rock and analogue materials, scaled for crustal scale processes and assuming lithostatic stress at depth. The data for the analogue materials has been scaled up using a scaling factor of $\sigma^* = \frac{\sigma_{\text{model}}}{\sigma_{\text{nature}}} = 1.214 \times 10^{-6}$. σ^* has been derived from geometry and density according to eq. 2.2. The rock data have been transformed to $(\tau, \sigma_{\text{n}})$-space using friction coefficients from fitted Mohr-Coulomb failure envelopes (original data shown in fig. 2.7 A). Quartz sand matches the natural data rather well, with the peak strength being in the range of natural data and the stable strength somewhat below Byerlee's law (Byerlee, 1978), which is an upper bound for natural stable strength. Glass beads are generally too weak to match the natural data. **B:** Relative weakening $\Delta\tau$ for rock and analogue materials, scaling factor $\sigma^* = \frac{\sigma_{\text{model}}}{\sigma_{\text{nature}}} = 1.241 \times 10^{-6}$. Both analogue materials show very similar $\Delta\tau$ and plot right within the range of natural data.

approximately parallel to the curve defined by Byerlee's law. These are both rather good matches, since Byerlee's law marks the upper limit of stable strength. However, for $\sigma_n \leq 200\,\mathrm{MPa}$ the quartz sand data do not follow the kink in Byerlee's law and are thus relatively too high for low normal loads. The strength of glass beads follows the same trend, but since it is generally lower it does not match the natural data as well as the quartz sand.

As discussed above, the relative weakening $\Delta\tau$ is even more important for the dynamic evolution of a shear zone than the absolute strength, because it can be directly linked to the reactivation potential of a shear zone. $\Delta\tau$ for this scaling is displayed in fig. 2.8 B. It is almost the same for both analogue materials, which fully plot in the range of the natural rock data. For very low loads, however, the weakening of rock becomes much larger than that of the analogue materials, due to natural rocks' complete loss of strength under these conditions.

Other Scales Sandbox models have been used not only for crustal scale tectonic models (tab. 2.3), but also to investigate processes on a basin scale (e. g. basin inversion) and granular materials have even been used to represent the entire brittle crust in lithospheric scale models. Length scales for these cases are on the order of $l^* = 10^{-5}$ and $l^* = 5 \times 10^{-7}$, respectively. This translates to basin scale models being about 10 cm thick (for 10 km of sedimentary rock), and the crust in lithospheric scale models being represented by a 1 cm thick layer of sand (tab. 2.3). For either case fig. 2.9 A shows that the shear strengths of the analogue materials are offset with respect to the rock data. For lithospheric scale models the shear strength of the analogue materials is too high, and only the measurements carried out at the lowermost normal load are within the rock data's range of confining pressures. A quantitative comparison is therefore difficult. For the basin scale case, on the other hand, the analogue material's shear strength is too low, the slopes of the failure envelopes do not match the natural ones and the weakening is too small.

This could potentially be improved by using more cohesive materials, an approach that is in fact common in the volcanotectonic community. In fig. 2.9 A this would ideally shift the peak strength upwards into the field of natural rock data without affecting the coefficient of internal friction. Tab. 4 in Galland, Holohan et al. (2015) lists the properties of frequently applied materials, and Abdelmalak et al. (2016) present a material of tunable cohesion. However, only peak strengths of the materials are reported and additional measurements would be required for quantitative comparison.

Strain at Failure An ideally scaled analogue material should not only withstand the same (scaled) load as its natural prototype, it should also fail after a similar amount of strain. For the rock data that were digitised from failure curves (Bieniawski et al., 1969; Crouch, 1970, 1971) we know this strain threshold to increase slightly with

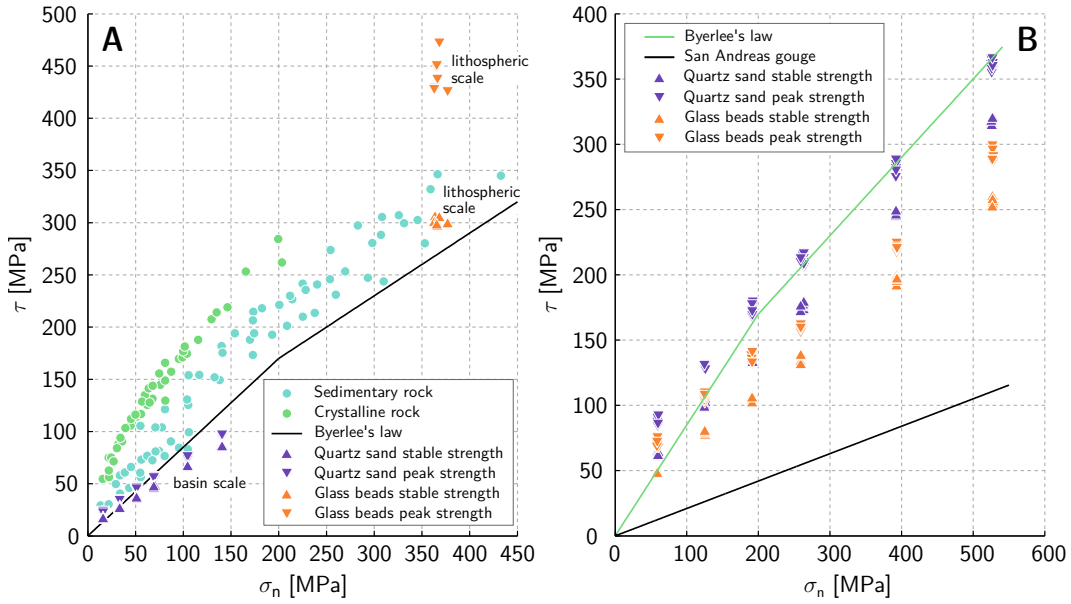

Fig. 2.9: A: Strength of analogue materials for basin- and lithospheric scale models in comparison to natural rock data. For the lithospheric scale case the weaker glass beads are shown, for the basin scale case the stronger quartz sand, but yet the analogue materials are to strong respectively too weak in either case. The rock data have been transformed to (τ, σ_n) - space using friction coefficients from fitted Mohr-Coulomb failure envelopes (original data shown in fig. 2.7). **B:** Strength of analogue materials scaled to a crust behaving according to Byerlee's law (Byerlee, 1978) and under hydrostatic conditions. San Andreas gouge refers to material recovered from drilling the San Andreas Fault, California (Lockner et al., 2011). Scaling factors in tab. 2.3.

confining pressure, and to generally range from 0.2 % to 1 %, with some measurements reaching up to 4 %. These numbers refer to the change of axial sample length normalised to the initial sample length.

To define a similar "bulk axial strain" value for the Ring-Shear tests, we construct a strain ellipse for each deformation increment during a measurement. We then calculate the length of the short axis of each strain ellipse and call its change in length normalised to its initial length the "axial strain" of these measurements. This yields the following formula for the axial strain in Ring-Shear tests, ϵ_{rst}:

$$\epsilon_{\mathrm{rst}} = 1 - \frac{h}{\sqrt{h^2 + d^2}} \tag{2.11}$$

Here h is the height of the shear zone and d the cumulative displacement at the moment under consideration. However, h cannot be measured during the experiments and therefore needs to be estimated. Panien et al. (2006) found the height of a mature shear zone in granular media to be 11 to 16 times the mean grain size, which would correspond to 3.3 mm to 4.8 mm for our quartz sand. Adam et al. (2005), on the other hand, observed an approximately 4 cm wide zone of diffuse deformation prior to localisation in compressive wedge experiments, using a quartz sand very similar to ours. We assume that this diffuse deformation is also present in our Ring-Shear experiments at the onset of deformation. Since the maximum possible height of the shear zone in our shear cell (i. e. the height of the shear cell minus the height of the blades at the bottom of the lid) is only 35 mm we expect the initial shear zone to span the entire shear cell. With progressive deformation localisation will take place and the shear zone will become narrower until it is only 3.3 mm to 4.8 mm wide. Localisation and narrowing of the shear zone will be completed shortly after peak stress (Lohrmann et al., 2003), i. e. at peak stress ("failure") the shear zone width will be something between 35 mm and 3.3 mm. This provides a range of possible strain values which lies between 0.03 % to 0.11 % for 35 mm shear zone width and 3 % to 12 % for 3.3 mm (quartz sand low-load subset, see displacement data in Ritter et al. (2016a)). These values are very similar for both quartz sand and glass beads.

Accordingly, rock strain at failure falls within the field of possible values of the analogue material's strain at failure. The latter are admittedly still very crude, however, we see no feasible way of deriving more precise values from our data at present.

Comparison to a Fractured Crust

When assuming the crust to be fractured throughout, Byerlee's law (eq. 2.10) should describe its peak strength. Obtaining values for the weakened strength of crustal faults is difficult, as this is subject of an ongoing debate. Current estimates range from "comparable to the surrounding rock" (Scholz, 2000) to friction coefficients as low as 0.2 (Lockner et al., 2011). The latter were measured in shear tests on natural gouge material recovered from drilling the San Andreas Fault, California, whereas the first was

estimated from rotation of horizontal stress directions at the same location. We will assume the weakest estimate, keeping in mind that it represents a very mature fault.

Townend and Zoback (2000) showed that in most cases the strength of the brittle crust is not controlled by σ_3, but by the effective stress $\sigma_3 - P_\mathrm{f}$, where P_f is the hydrostatic pore fluid pressure. We include this in our scaling by calculating the natural stress as $\sigma_\mathrm{nature} = (\rho_\mathrm{crust} - \rho_\mathrm{fluid})gh$, where ρ_fluid is the density of the pore fluid (water). For crustal scale models ($l^* = 2 \times 10^{-6}$) this leads to a stress scale $\sigma^* = 1.889 \times 10^{-6}$ (tab. 2.3). The scaled strengths are shown in fig. 2.9 B. For $\sigma_\mathrm{n} \geq 200\,\mathrm{MPa}$ the upscaled peak strength of quartz sand matches that of the crust nearly perfectly. For lower normal loads it is slightly too high, because it does not follow the kink in Byerlee's law. This kink corresponds to a depth of roughly 7 km in nature or 1.4 cm in a crustal scale model.

The stable strength of quartz sand is much higher than the strength given by the friction coefficient of 0.2 measured for San Andreas gouge. The glass beads' stable strength is similarly too high, moreover, their peak strength is well below the strength given by Byerlee's law. Since for both analogue materials the stable strength is much higher than for the natural example, weakening is too low to properly represent large mature faults.

2.5 Conclusion

Using a Ring-Shear tester we measured frictional properties of two granular materials that are typically applied in analogue tectonic modelling. Our results show a change of the frictional properties with normal load, that divides the data into a "high-load" and a "low-load" subset. While the high-load subset behaves similar to measurements previously published (weakening through reduction of internal friction, Krantz (1991), Lohrmann et al. (2003) and Panien et al. (2006)), the low-load subset shows a behaviour that had not been observed so far: Weakening through reduction of cohesion. The range of normal loads for which this different frictional behaviour is important coincides roughly with the range of normal loads common in analogue models and thus our findings affect the suitability of these materials for modelling. Importantly, the weakening through reduction of cohesion introduces a scale dependence of material strength, which had previously not been recognised. As a consequence, the tested granular materials are best suited for modelling crustal scale processes, regardless of whether the actual behaviour of the crust is closer to Byerlee's law or laboratory-derived failure envelopes of intact rock. We suggest a length scaling factor of $l^* = 2 \times 10^{-6}$ to obtain the correct dynamically scaled material strength for sand-box models using loose quartz sand. For other length scaling factors the relative weakening and thus the lifetime and reactivation potential of shear zones are likely to be different than in the natural prototype. Glass beads are generally less suited, but might be the right choice to model particularly weak structures.

Acknowledgments

M. C. R. and K. L. are funded by the Helmholtz Graduate School GeoΣim. The data used in this paper are available under the following DOI: 10.5880/GFZ.4.1.2016.005. The authors thank Kirsten Elger and the GFZ Data Service for publishing the data.

An edited version of this article has been published in the Journal of Geophysical Research: Solid Earth.

References

Abdelmalak, M., C. Bulois, R. Mourgues, O. Galland, J.-B. Legland and C. Gruber (2016): 'Description of new dry granular materials of variable cohesion and friction coefficient: Implications for laboratory modeling of the brittle crust'. In: *Tectonophysics* 684, pp. 39–51. DOI: 10.1016/j.tecto.2016.03.003.

Adam, J., J. L. Urai, B. Wieneke, O. Oncken, K. Pfeiffer, N. Kukowski, J. Lohrmann, S. Hoth, W. van der Zee and J. Schmatz (2005): 'Shear localisation and strain distribution during tectonic faulting—new insights from granular-flow experiments and high-resolution optical image correlation techniques'. In: *Journal of Structural Geology* 27.2, pp. 283–301. DOI: 10.1016/j.jsg.2004.08.008.

Al-Ajmi, A. M. and R. W. Zimmerman (2005): 'Relation between the Mogi and the Coulomb failure criteria'. In: *International Journal of Rock Mechanics and Mining Sciences* 42, pp. 431–439. DOI: 10.1016/j.ijrmms.2004.11.004.

Bieniawski, Z., H. Denkhaus and U. Vogler (1969): 'Failure of fractured rock'. In: *International Journal of Rock Mechanics and Mining Sciences & Geomechanics Abstracts* 6.3, pp. 323–341. DOI: 10.1016/0148-9062(69)90009-6.

Brace, W. F. and D. L. Kohlstedt (1980): 'Limits on lithospheric stress imposed by laboratory experiments'. In: *Journal of Geophysical Research* 85.B11, p. 6248. DOI: 10.1029/JB085iB11p06248.

Brudy, M., M. D. Zoback, K. Fuchs, F. Rummel and J. Baumgärtner (1997): 'Estimation of the complete stress tensor to 8 km depth in the KTB scientific drill holes: Implications for crustal strength'. In: *Journal of Geophysical Research: Solid Earth* 102.B8, pp. 18453–18475. DOI: 10.1029/96JB02942.

Brun, J.-P. (1999): 'Narrow rifts versus wide rifts: inferences for the mechanics of rifting from laboratory experiments'. In: *Philosophical Transactions of the Royal Society A: Mathematical, Physical and Engineering Sciences* 357.1753, pp. 695–712. DOI: 10.1098/rsta.1999.0349.

Buchanan, P. and K. McClay (1991): 'Sandbox experiments of inverted listric and planar fault systems'. In: *Tectonophysics* 188.1-2, pp. 97–115. DOI: 10.1016/0040-1951(91)90317-L.

Burchardt, S. and T. R. Walter (2010): 'Propagation, linkage, and interaction of caldera ring-faults: comparison between analogue experiments and caldera collapse at Miyakejima, Japan, in 2000'. In: *Bulletin of Volcanology* 72.3, pp. 297–308. DOI: 10.1007/s00445-009-0321-7.

Bürgmann, R. and G. Dresen (2008): 'Rheology of the Lower Crust and Upper Mantle: Evidence from Rock Mechanics, Geodesy, and Field Observations'. In: *Annual Review of Earth and Planetary Sciences* 36.1, pp. 531–567. DOI: 10.1146/annurev.earth.36.031207.124326.

Byerlee, J. D. (1968): 'Brittle-ductile transition in rocks'. In: *Journal of Geophysical Research* 73.14, pp. 4741–4750. DOI: 10.1029/JB073i014p04741.

– (1975): 'The fracture strength and frictional strength of Weber Sandstone'. In: *International Journal of Rock Mechanics and Mining Sciences & Geomechanics Abstracts* 12.1, pp. 1–4. DOI: 10.1016/0148-9062(75)90736-6.

– (1978): 'Friction of rocks'. In: *Pure and Applied Geophysics* 116.4-5, pp. 615–626. DOI: 10.1007/BF00876528.

Cobbold, P. R., S. Durand and R. Mourgues (2001): 'Sandbox modelling of thrust wedges with fluid-assisted detachments'. In: *Tectonophysics* 334.3-4, pp. 245–258. DOI: 10.1016/S0040-1951(01)00070-1.

Cook, N. (1965): 'The failure of rock'. In: *International Journal of Rock Mechanics and Mining Sciences & Geomechanics Abstracts* 2.4, pp. 389–403. DOI: 10.1016/0148-9062(65)90004-5.

Crouch, S. L. (1970): 'Experimental determination of volumetric strains in failed rock'. In: *International Journal of Rock Mechanics and Mining Sciences and* 7, pp. 589–603. DOI: 10.1016/0148-9062(70)90020-3.

– (1971): 'The post-failure behaviour of norite in triaxial compression'. In: *Engeneering Geology* 6.6, pp. 19–30. DOI: 10.1126/science.ns-5.112.260.

Cubas, N., C. Barnes and B. Maillot (2013): 'Inverse method applied to a sand wedge: Estimation of friction parameters and uncertainty analysis'. In: *Journal of Structural Geology* 55, pp. 101–113. DOI: 10.1016/j.jsg.2013.07.003.

Cubas, N., B. Maillot and C. Barnes (2010): 'Statistical analysis of an experimental compressional sand wedge'. In: *Journal of Structural Geology* 32.6, pp. 818–831. DOI: 10.1016/j.jsg.2010.05.010.

Davy, P. and P. R. Cobbold (1988): 'Indentation tectonics in nature and experiment. 1. Experiments scaled for gravity'. In: *Bulletin of the Geological Institutions of Uppsala* 14, pp. 129–141.

Desrues, J. and G. Viggiani (2004): 'Strain localization in sand: an overview of the experimental results obtained in Grenoble using stereophotogrammetry'. In: *International Journal for Numerical and Analytical Methods in Geomechanics* 28.4, pp. 279–321. DOI: 10.1002/nag.338.

Dooley, T. P. and G. Schreurs (2012): 'Analogue modelling of intraplate strike-slip tectonics: A review and new experimental results'. In: *Tectonophysics* 574-575, pp. 1–71. DOI: 10.1016/j.tecto.2012.05.030.

Duerto, L. and K. McClay (2009): 'The role of syntectonic sedimentation in the evolution of doubly vergent thrust wedges and foreland folds'. In: *Marine and Petroleum Geology* 26.7, pp. 1051–1069. DOI: 10.1016/j.marpetgeo.2008.07.004.

Galland, O., S. Burchardt, E. Hallot, R. Mourgues and C. Bulois (2014): 'Dynamics of dikes versus cone sheets in volcanic systems'. In: *Journal of Geophysical Research: Solid Earth* 119.8, pp. 6178–6192. DOI: 10.1002/2014JB011059.

Galland, O., P. R. Cobbold, E. Hallot, J. de Bremond d'Ars and G. Delavaud (2006): 'Use of vegetable oil and silica powder for scale modelling of magmatic intrusion in a deforming brittle crust'. In: *Earth and Planetary Science Letters* 243.3-4, pp. 786–804. DOI: 10.1016/j.epsl.2006.01.014.

Galland, O., E. Holohan, B. van Wyk de Vries and S. Burchardt (2015): 'Laboratory Modelling of Volcano Plumbing Systems: A Review'. In: *Advances in Volcanology*. Berlin, Heidelberg: Springer, pp. 1–68. DOI: 10.1007/11157_2015_9.

Graveleau, F., J. Malavieille and S. Dominguez (2012): 'Experimental modelling of orogenic wedges: A review'. In: *Tectonophysics* 538-540, pp. 1–66. DOI: 10.1016/j.tecto.2012.01.027.

Gutscher, M.-A., N. Kukowski, J. Malavieille and S. E. Lallemand (1996): 'Cyclical behavior of thrust wedges: Insights from high basal friction sandbox experiments'. In: *Geology* 24.2, pp. 135–138. DOI: 10.1130/0091-7613(1996)024.

Herbert, J. W., M. L. Cooke, P. Souloumiac, E. H. Madden, B. C. Mary and B. Maillot (2015): 'The work of fault growth in laboratory sandbox experiments'. In: *Earth and Planetary Science Letters* 432, pp. 95–102. DOI: 10.1016/j.epsl.2015.09.046.

Holohan, E. P., T. R. Walter, M. P. Schöpfer, J. J. Walsh, B. van Wyk de Vries and V. R. Troll (2013): 'Origins of oblique-slip faulting during caldera subsidence'. In: *Journal of Geophysical Research: Solid Earth* 118.4, pp. 1778–1794. DOI: 10.1002/jgrb.50057.

Hubbert, M. K. (1937): 'Theory of scale models as applied to the study of geologic structures'. In: *Bulletin of the Geological Society of America* 48, pp. 1459–1520.

Jaeger, J. C., N. Cook and R. W. Zimmerman (2007): *Fundamentals of Rock Mechanics*. 4th ed. Oxford: Blackwell Publishing, p. 468.

Klinkmüller, M., G. Schreurs, M. Rosenau and H. Kemnitz (2016): 'Properties of granular analogue model materials: A community wide survey'. In: *Tectonophysics* 684, pp. 23–38. DOI: 10.1016/j.tecto.2016.01.017.

Klinkmüller, M., G. Schreurs and M. Rosenau (2016): *GeoMod2008 materials benchmark: The ring shear test data set*. DOI: 10.5880/GFZ.4.1.2016.002.

Kolymbas, D. and W. Wu (1990): 'Recent results of triaxial tests with granular materials'. In: *Powder Technology* 60.2, pp. 99–119. DOI: 10.1016/0032-5910(90)80136-M.

Krantz, R. W. (1991): 'Measurements of friction coefficients and cohesion for faulting and fault reactivation in laboratory models using sand and sand mixtures'. In: *Tectonophysics* 188.1-2, pp. 203–207. DOI: 10.1016/0040-1951(91)90323-K.

Leever, K. A., R. H. Gabrielsen, D. Sokoutis and E. Willingshofer (2011): 'The effect of convergence angle on the kinematic evolution of strain partitioning in transpressional brittle wedges: Insight from analog modeling and high-resolution digital image analysis'. In: *Tectonics* 30.2. DOI: 10.1029/2010TC002823.

Lockner, D. A., C. Morrow, D. Moore and S. Hickman (2011): 'Low strength of deep San Andreas fault gouge from SAFOD core'. In: *Nature* 472.7341, pp. 82–85. DOI: 10.1038/nature09927.

Lohrmann, J., N. Kukowski, J. Adam and O. Oncken (2003): 'The impact of analogue material properties on the geometry, kinematics, and dynamics of convergent sand wedges'. English. In: *Journal of Structural Geology* 25.10, pp. 1691–1711. DOI: 10.1016/S0191-8141(03)00005-1.

Luth, S., E. Willingshofer, D. Sokoutis and S. Cloetingh (2013): 'Does subduction polarity changes below the Alps? Inferences from analogue modelling'. In: *Tectonophysics* 582, pp. 140–161. DOI: 10.1016/j.tecto.2012.09.028.

Mandl, G., L. N. J. Jong and A. Maltha (1977): 'Shear zones in granular material'. In: *Rock Mechanics Felsmechanik Mécanique des Roches* 9.2-3, pp. 95–144. DOI: 10.1007/BF01237876.

McClay, K. (1990): 'Extensional fault systems in sedimentary basins: a review of analogue model studies'. In: *Marine and Petroleum Geology* 7.3, pp. 206–233. DOI: 10.1016/0264-8172(90)90001-W.

Mechelen, J. L. M. van (2004): 'Strength of moist sand controlled by surface tension for tectonic analogue modelling'. In: *Tectonophysics* 384.1-4, pp. 275–284. DOI: 10.1016/j.tecto.2004.04.003.

Nieuwland, D. A., J. L. Urai and M. Knoop (2000): 'In-situ stress measurements in model experiments of tectonic faulting'. In: *Aspects of Tectonic Faulting*. Ed. by F. K. Lehner and J. L. Urai. Berlin, Heidelberg: Springer Berlin Heidelberg, pp. 155–166. DOI: 10.1007/978-3-642-59617-9_8.

Panien, M., G. Schreurs and O. A. Pfiffner (2006): 'Mechanical behaviour of granular materials used in analogue modelling: insights from grain characterisation, ring-shear tests and analogue experiments'. English. In: *Journal of Structural Geology* 28.9, pp. 1710–1724. DOI: 10.1016/j.jsg.2006.05.004.

Ritter, M. C., K. A. Leever, M. Rosenau and O. Oncken (2016a): *Supplement to: Scaling the Sand Box - Mechanical (Dis-) Similarities of Granular Materials and Brittle Rock*. DOI: 10.5880/GFZ.4.1.2016.005.

Ritter, M. C., K. Leever, M. Rosenau and O. Oncken (2016b): 'Scaling the sandbox — Mechanical (dis-) similarities of granular materials and brittle rock'. In: *Journal of Geophysical Research: Solid Earth* 121.9, pp. 6863–6879. DOI: 10.1002/2016JB012915.

Rosenau, M., J. Lohrmann and O. Oncken (2009): 'Shocks in a box: An analogue model of subduction earthquake cycles with application to seismotectonic forearc evolution'. In: *Journal of Geophysical Research* 114.B1, B01409. DOI: 10.1029/2008JB005665.

Schellart, W. (2000): 'Shear test results for cohesion and friction coefficients for different granular materials: scaling implications for their usage in analogue modelling'. In: *Tectonophysics* 324.1-2, pp. 1–16. DOI: 10.1016/S0040-1951(00)00111-6.

Scholz, C. H. (2000): 'Evidence for a strong San Andreas fault'. In: *Geology* 28.2, p. 163. DOI: 10.1130/0091-7613(2000)28<163:EFASSA>2.0.CO;2.

– (2002): *The Mechanics of Earthquakes and Faulting*. 2nd editio. Cambridge: Cambridge University Press, p. 471.

Schulze, D. (1994): 'Development and application of a Novel Ring Shear Tester'. In: *Aufbereitungstechnik* 35.10, pp. 524–535.

Townend, J. and M. D. Zoback (2000): 'How faulting keeps the crust strong'. In: *Geology* 28.5, pp. 399–402. DOI: 10.1130/0091-7613(2000)28<399:HFKTCS>2.0.CO.

Tron, V. and J.-P. Brun (1991): 'Experiments on oblique rifting in brittle-ductile systems'. In: *Tectonophysics* 188.1-2, pp. 71–84. DOI: 10.1016/0040-1951(91)90315-J.

Wawersik, W. R. and C. Fairhurst (1970): 'A study of brittle rock fracture in laboratory compression experiments'. In: *International Journal of Rock Mechanics and Mining Science and Geomechanics Abstracts* 7, pp. 561–575. DOI: 10.1016/0148-9062(70)90007-0.

Weijermars, R. and H. Schmeling (1986): 'Scaling of Newtonian and non-Newtonian fluid dynamics without inertia for quantitative modelling of rock flow due to gravity (including the concept of rheological similarity)'. In: *Physics of the Earth and Planetary Interiors* 43.4, pp. 316–330. DOI: 10.1016/0031-9201(86)90021-X.

2.6 Additional Measurements

After preparation of the above manuscript we have undertaken additional analyses in order to shed light on the possible causes for the observed increase of peak strength τ_p with normal load σ_n. We investigated two possibilities, compaction and "healing".

In the first case an increase of compaction at the onset of deformation would effectively increase the bulk density of the sample and thereby increase the peak strength (e. g. Krantz, 1991). Our data allows to quantify initial compaction as the downward movement of the lid of the RST (fig. 2.10). As can be seen from the figure, initial compaction is always around 0.2 % of the initial volume, or 0.08 mm and thus an order of magnitude smaller than the average grain size. Although the scatter increases at low normal loads, there is no systematic variation apparent. We therefore conclude that the reported changes in τ_p with increasing normal load are not due to an increase of sample density caused by compaction.

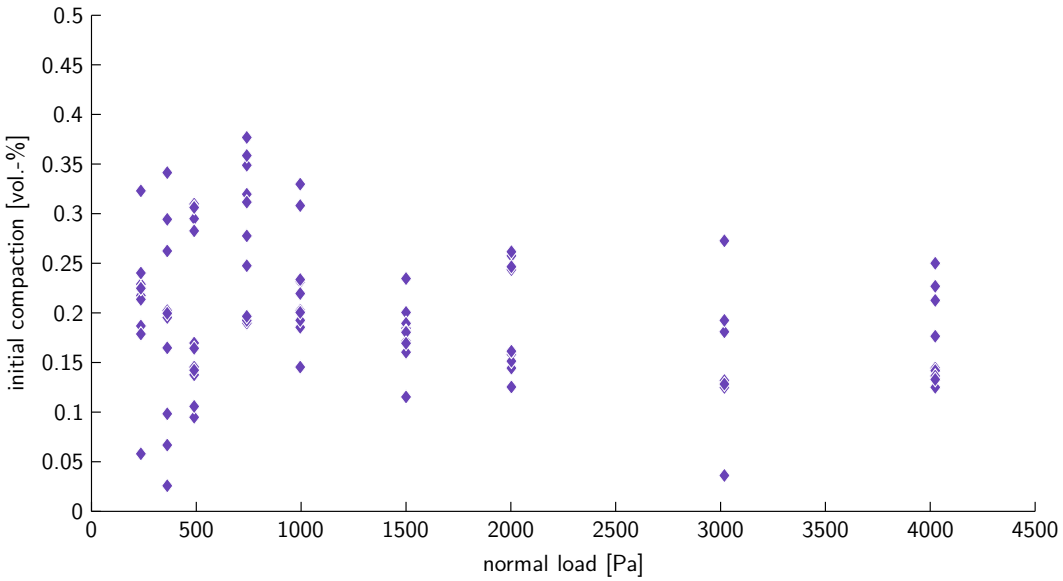

Fig. 2.10: Initial sample compaction in RST experiments measured as lid subsidence. The data show increased scatter for low normal loads, but no systematic variation. The observed increase in τ_p with σ_n is thus probably not caused by increased compaction.

In the second case, the so-called healing, the grain-grain contact area and thus the frictional resistance increase with normal load through elastic indentation and possibly through limited, local plastic yielding of the highly stressed grain contacts. This process is proportional to normal load and to the logarithm of contact time (Dieterich and Kilgore, 1994; Schulze, 2003). It can be measured using slide-hold-slide tests in the ring-shear tester, in which a sample is first sheared at a constant rate

until stable shear stress is achieved; then shearing is suspended without relaxing the applied normal and shear stresses. After a given holding time, during which the material relaxes partly, shearing is resumed and the reactivation stress is measured relative to the stable sliding stress before shearing was suspended.

We have performed such tests on samples of our quartz sand for holding times from 1 s to 10^3 s and normal loads from 0.5 kPa to 10 kPa. The results are shown in fig. 2.11 as the increase of reactivation stress per order of magnitude holding time, versus the normal load. The data clearly show an increase from no detectable healing at 0.5 kPa normal load to approximately 30 Pa per order of magnitude holding time at 10 kPa. Therefore, a load dependent healing process is evident, which we interpret as a possible cause of the load-dependency of friction coefficients, i. e. we argue that in the high-load regime healing becomes an additional significant micro-mechanical mechanism controlling friction which is not detectable – within the precision of the measurement – at low loads.

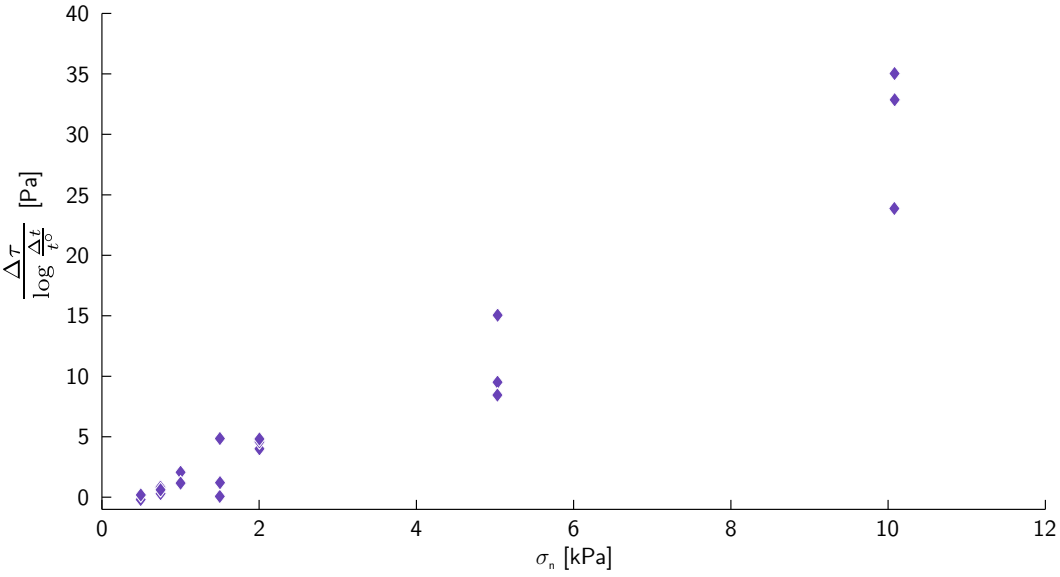

Fig. 2.11: Healing of quartz sand from slide-hold-slide tests. The data shown reflect the increase of reactivation stress per order of magnitude holding time with normal load. Here, $\Delta\tau$ is the hardening during holding, log is the logarithm to the base ten, Δt is the holding time and t° is the unit time.

In the original experiments presented in the manuscript, some time elapses between loading a sample and starting the deformation, which is needed to double-check all settings. During this time healing can take place. At reactivation, on the other hand, the time needed for stopping deformation, relaxing the sample and resuming deformation is less than 1 s, which is why the friction coefficient for reactivation is

less sensitive to normal load. The amount of healing we measure is not sufficient to explain the observed increase of the peak friction coefficient, however, it has to be taken into account that healing is measured in a pre-sheared sample where the density of grain-grain contacts is significantly less, thus reducing the potential for healing.

References

Dieterich, J. H. and B. D. Kilgore (1994): 'Direct observation of frictional contacts: New insights for state-dependent properties'. In: *Pure and Applied Geophysics* 143.1-3, pp. 283–302. DOI: 10.1007/BF00874332.

Krantz, R. W. (1991): 'Measurements of friction coefficients and cohesion for faulting and fault reactivation in laboratory models using sand and sand mixtures'. In: *Tectonophysics* 188.1-2, pp. 203–207. DOI: 10.1016/0040-1951(91)90323-K.

Schulze, D. (2003): 'Time- and Velocity-Dependent Properties of Powders Effecting Slip-Stick Oscillations'. In: *Chemical Engineering & Technology* 26.10, pp. 1047–1051. DOI: 10.1002/ceat.200303112.

3 A New Experimental Device to Simultaneously Measure Stress and Strain in Tectonic Sandbox Experiments

Abstract

Geodynamic processes are often too slow to be monitored directly, while at the same time being too fast to be accurately reconstructed from the geological record. Furthermore, measurements of the driving stresses are principally impossible for past tectonic events. Analogue sandbox experiments do not have these limitations and have thus been used for a long time to understand tectonic processes. Despite their long history, force measurements in analogue sandbox experiments have only emerged recently and combined measurements of forces and deformation are still rare to date and the reported force data is often noisy.

In this article we present an experimental device that facilitates precise measurements of boundary forces and surface deformation at high temporal and spatial resolution. We demonstrate its capabilities in one experiment of strike-slip and compressional deformation, respectively. In these we are able to directly observe correlations between strain weakening and strain localisation that had previously only been inferred. Our data additionally shows that deformation in the often applied Riedel-type set-up is controlled mainly by the boundary conditions and not by the mechanical properties of the material.

3.1 Introduction

Understanding of geodynamic processes based on natural data alone is difficult, because of the large temporal and spatial scales involved: The observational, seis-

Manuscript in preparation intended for publication in *Tectonophysics*, with authors: Malte C. Ritter, Tasca Santimano, Matthias Rosenau, Karen Leever, Onno Oncken.

Individual Contributions: M. C. R. planned research was involved in developing the set-up and performed the strike-slip experiment, analysed and interpreted results of both experiments, wrote the paper; T. S. was involved in developing the set-up and performed wedge experiment (preliminary results of a similar experiment are presented in her thesis (Santimano, 2016)), participated in writing the paper; M. R. was involved in developing the set-up and analysis and interpretation of the data, participated in writing the paper; K. L. was involved in planning the research and interpretation of the data, participated in writing the paper; O. O. was involved in planning the experiments, supervised the research.

motectonic and paleotectonic history of features such as fault systems or orogens spans a few decades to thousands of years at most, while the underlying processes are active over thousands to millions of years. Information from the geological record, on the other hand, is generally sparse and of a temporal accuracy too limited to reconstruct the evolution of the features in detail.

Scaled analogue sandbox experiments can fill this gap, as they provide physical models that can be subjected to all kinds of measurements at virtually any resolution required, only limited by the scale of granular material used. Traditionally, analogue experiments have mostly been observed by optical means, ranging from photography and stereo-photogrammetry via laser interferometry to Digital Image Correlation (DIC) of surface images (see Graveleau et al., 2012, for a review). Internal structures have commonly been analysed by wetting and cutting the model post mortem. Recently, also X-ray computed tomography has been used to non-destructively monitor the evolution of internal structures during deformation (Schreurs et al., 2003). All of these observations aim at the kinematic evolution of the model and thus the effects of deformation. In an attempt to link those kinematic observations to dynamics some authors (Adam et al., 2005; Dotare et al., 2016) have drawn analogies between their models and mechanical testing results (e. g. Lohrmann et al., 2003; Ritter et al., 2016). Finally, analytical and numerical models have been used to analyse sandbox dynamics (Cubas, Leroy et al., 2008; Cubas, Barnes et al., 2013). However, a quantitative understanding of sandbox dynamics requires the knowledge of both stress and strain to formulate constitutive laws of their deformation.

Only recently, experimenters have begun to carry out force measurements on analogue models in order to gain a better understanding of their dynamics and thus the driving factors of deformation (Nieuwland et al., 2000). The data have been used e. g. to quantify the effect of side wall friction in sand box experiments (Cubas, Maillot et al., 2010; Souloumiac et al., 2012), and to assess the work done during fault formation (Herbert et al., 2015). All of these studies concentrated on the mechanical evolution. The next step in the development of experimental set-ups would be to combine both observation techniques – high resolution optical imaging and force measurements – in a single experiment to analyse the interplay between mechanical and kinematic evolution. In this article we present an experimental device that facilitates such studies and verify it using a set of preliminary experiments.

3.2 Experimental Set-Up

3.2.1 Experimental Device

The experimental deformation device introduced in this study is designed to be versatile for use in different settings. In this article we describe two principal

applications: an accretionary wedge setting and a strike-slip setting. In both set-ups a stationary sand pack of a few centimetres thickness is deformed by a moving back-wall. In its most straightforward application this back-wall is used directly as an indenter that is pushed into the sand pack, creating a convergent wedge setting. We will first describe the basic device as it is used for this kind of experiments, and later show the modifications that can be made to adapt it to model strike-slip deformation.

The Basic Device: Convergent Wedge Setting

The basic device consists of a tank made of acrylic glass (100 cm × 100 cm × 30 cm). Its flat bottom can be covered with various materials to control the basal strength within a wide range from virtually zero (using e. g. a silicone-based lubricant) to high friction (sandpaper). The box is watertight and all parts inside the box are waterproof to allow the realisation of floating models, if desired. Two parallel linear actuators consisting each of a ball screw and a stepper motor are installed at the top of the tank to impose accurate and precise deformation on the model inside the tank (fig. 3.1 A). The nuts of the two ball screws are connected by an aluminium beam from which the moving back-wall is suspended. The stepper motors are computer-controlled and synchronised to prevent tilting of the beam. The horizontal velocity of the beam can be varied between 0.01 mm s^{-1} and 6 mm s^{-1}, with a maximum pushing force at the beam of about 2.5 kN. This is orders of magnitude beyond what is actually needed in typical sandbox experiments, but it provides a comfortable buffer and immediate acceleration in case of applications featuring velocity changes in viscous materials.

The moving back-wall consists of an aluminium plate (thickness 1 cm, to prevent bending) that is connected to the horizontal beam by two precision hinges designed for minimum backlash. A vertical beam connected to the backside of the plate acts as a lever that holds the back-wall upright and couples it to a sensor registering the force required for this (fig. 3.1 B). Any push against the back-wall will result in a corresponding pulling force at the sensor. A load at the upper end of the beam compensates the mass of the back-wall itself, such that in the initial state the force sensor is without load. The sensor's position along the vertical beam can be adjusted to optimally exploit its full range; the reading from the sensor must then be corrected with the ratio of the lever arms to get the actual force integrated over the back wall. Several force sensors are currently available and can be chosen depending on the expected force, with maximum load capacities ranging from 50 N to 10 kN (S-beam type, *KM1401*- and *KM1501*-series by *Megatron GmbH & Co. KG*, Munich, Germany). In the following experiments the 50 N-sensor has been used unless stated otherwise. Its output is recorded at a sampling rate of 1 kHz by the same computer that controls the stepper motors. Besides performing experiments with controlled velocity, this set-up allows in principle also force-controlled routines. An algorithm sensitive enough to balance the subtle force changes expected in analogue experiments

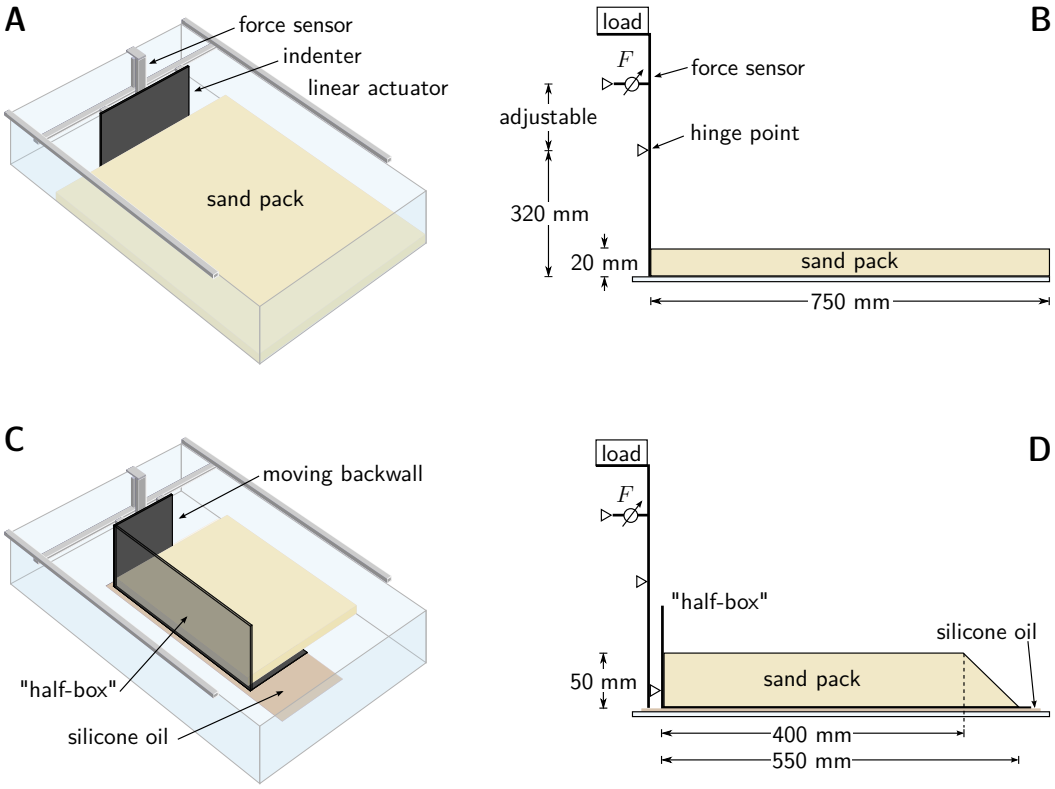

Fig. 3.1: A and **B**: Experimental set-up for indenter experiment. An indenter is pushed into a stationary layer of sand (20 mm) overlying a basal detachment layer made of 5 mm glass beads (diameter: 40 µm to 70 µm), resting on sand paper. The indenter is driven by two linear actuator located along the edges of the box made of acrylic glass. Via a lever arm the force acting on the bottom of the indenter is transmitted to a force sensor. The force sensor's vertical position is adjustable to match the expected force to the load capacity of the sensor and operate it in its optimum range.
C and **D**: Experimental set-up for strike-slip experiment. The indenter from A is replaced by a "half box" consisting of a basal plate with a back-wall and one sidewall. It is underlain by a 5 mm thin layer of low viscosity silicone oil ($\eta = 1520\,\mathrm{Pa\,s}$) for lubrication and underlies half of the sand pack. The other half of the sand pack is underlain directly by the bottom of the acrylic glass box. Upon displacing the half box a shear zone forms above the edge of the half box. This set-up is thus a variation of the classical Riedel set-up modified for force measurements.

is currently in a testing phase. This operating mode will be particularly interesting for experiments containing visco-elastic materials.

Strike-Slip Modifications

To convert the indenter device into a strike-slip device of the classical Riedel-type, in which a sand pack is sheared above a basal discontinuity (Cloos, 1928; Riedel, 1929), a "half-box" is placed in front of the moving back-wall (fig. 3.1 C, D). This half-box is a combination of a back-wall, one sidewall and a base, made from 2.5 mm stainless steel. It is coupled to the moving back-wall by another hinge to prevent it from turning sideways, while at the same time transmitting horizontal forces only. The dimensions of the half-box are such that its base underlies only half of the sand pack (hence the name "half-box"), while the other half of the sand pack rests on the stationary base of the acrylic glass tank. When the half-box is pushed forward, the sand pack is sheared at the discontinuity along the edge of the half-box and a strike-slip shear zone develops. Underneath the half-box a 5 mm thin layer of a low-viscosity silicone paste ($\eta = 1520\,\mathrm{Pa\,s}$) provides lubrication. By keeping the deformation rate low ($30\,\mu\mathrm{m\,s^{-1}}$), the basal drag can be minimised to 10 Pa which is about an order of magnitude lower than the cohesion of the sand used. Moreover, as it is a constant value, it can be easily accounted for in the analysis of forces.

Optical monitoring

In addition to the force measurements, the experiments are optically monitored from the top using one digital camera (*ImagerProX* by *LaVision GmbH*, Göttingen, Germany) that produces uncompressed, 14-bit greyscale images with a spatial resolution of $2600\,\mathrm{px} \times 4000\,\mathrm{px}$ (pixel) at a recording rate of up to 5 Hz. The camera is controlled by a separate computer. The two systems (force sensor and optical recording) are synchronised manually by first starting the camera and then, after typically ten still images, the displacement of the moving back-wall, such that the onset of deformation is captured by the camera and the time shift can be reconstructed. From the images capturing the deforming model surface displacement fields can be derived by means of DIC (Adam et al., 2005), using the software *StrainMaster* distributed by *LaVision GmbH*. The noise of the displacement fields is estimated using the initial still images captured before the onset of back-wall displacement.

3.2.2 Analogue materials used

We use quartz sand G23T as brittle analogue material. This is a medium-grained, moderately sorted fluvial sand with rounded grains and a mean grain size of 300 µm (Klinkmüller et al., 2016). Its mechanical behaviour under experimental conditions can be described by two Mohr-Coulomb failure envelopes, $\tau_\mathrm{p} = 0.58\,\sigma_\mathrm{n} + 110\,\mathrm{Pa}$ for the peak strength and $\tau_\mathrm{s} = 0.55\,\sigma_\mathrm{n} + 60\,\mathrm{Pa}$ for the stable sliding strength after failure

(Ritter et al., 2016). In the compressional wedge experiments, sand paper is used to gain higher basal friction. This sandpaper is made by sifting the same quartz sand onto an adhesive tape. The resulting basal friction is significantly lower than the internal friction ($\mu_p = 0.41$ and $\mu_s = 0.34$, Klinkmüller et al., 2016). Reactivation of existing faults is described by Lohrmann et al. (2003), Panien et al. (2006) and Klinkmüller et al. (2016), among others.

3.3 Observations and interpretations

3.3.1 Strike-slip experiment

In this experiment a 5 cm thick layer of sifted sand is used, which is 32 cm wide and 40 cm long. The input displacement rate is 30 µm s^{-1} and the optical recording rate is set to 1 Hz. The effective spatial resolution of the camera images is 0.1 mm px^{-1}.

Kinematic observations

At the beginning of the experiment, and for the first 3 mm of back-wall displacement, shearing is taken up by a broad, through-going shear zone (fig. 3.2, A). Deformation subsequently localises into three narrow Riedel-shears that are initially oriented at an angle of 15° to the trace of the basal discontinuity (fig. 3.2, B). They form one after another, starting at the end further away from the back-wall. The shears then grow in length (fig. 3.2, C) and slowly rotate inwards until they finally connect and form once again a through-going, but this time localised, slightly anastomosing shear zone (fig. 3.2, D). The anastomosing shape stems from the fact that the shear zones do not connect directly tip-to-tip, but rather curve around each other and link up with some overlap. This general evolution is consistent with observations from earlier experiments described e. g. by Dooley and Schreurs (2012).

To visualise deformation through time, a "width evolution map" of the shear zone is created from the displacement fields. This is done by measuring the width of the active shear zone for each displacement increment and at each position along strike (x-direction). These values are projected onto profile lines, one per displacement increment, and the profile lines are then assembled to form the width map (fig. 3.3). In the resulting map the formation of localised shear zones can be traced as transition from blue (wide) to yellow (narrow) colours. It clarifies the timing of shear zone formation, starting with a short localised shear zone at the rear end of the box. A second and a third one form subsequently in the middle of the box and at the moving back-wall, respectively. The map further shows that shear zone growth is not a continuous process but occurs step-wise. It also shows the locations of overlapping branches of shear zones as patches of intermediate shear zone width, due to summation of their respective widths.

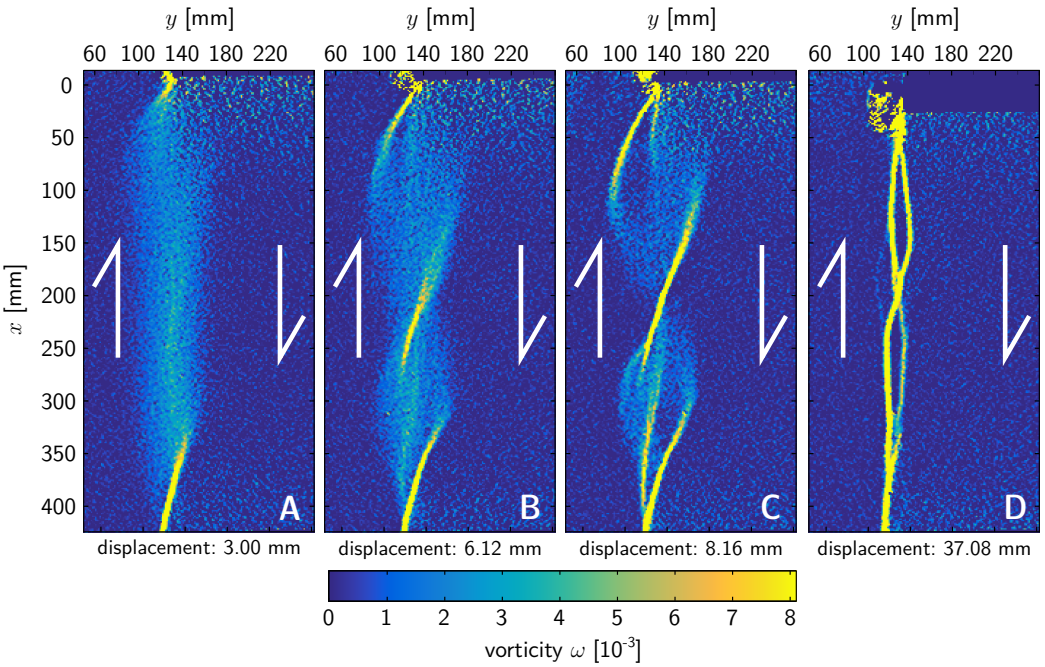

Fig. 3.2: Deformation maps showing the evolution of the shear zone in the strike-slip experiments: Initially, displacement is taken up by a broad, diffuse shear zone (**A**). Subsequently, three localised Riedel-shears form at an angle of 14° to the trace of the basal discontinuity (**B**), which then grow and rotate towards each other (**C**). Instead of rotation of the existing shears, new shears at a more favourable orientation can also form (**C**, bottom). Finally, the shears link up and form an anastomosing shear zone (**D**). The maps use the vorticity ω of the displacement field for visualising the shear zones, i.e. the difference between the off-diagonal components of the 2-D strain tensor at each point: $\omega = \frac{\partial u_y}{\partial x} - \frac{\partial u_x}{\partial y}$, where u is the displacement vector at the respective point.

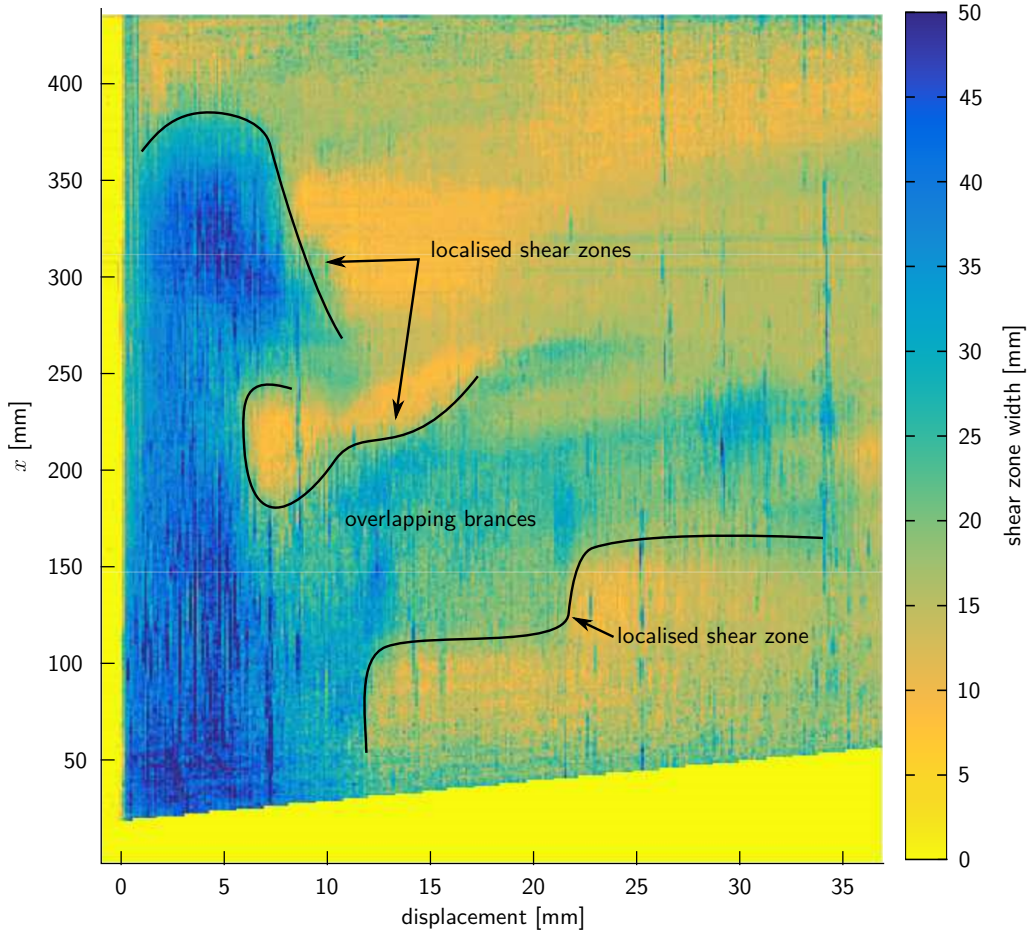

Fig. 3.3: Map showing the bulk width of the strike-slip shear zone along strike over time. Bulk width is defined here as the total width of the area affected by deformation at a given displacement increment and is determined separately for each point along strike. The map shows the formation of Riedel-shears as the transition from blue to yellow colours (reduction of width). It clearly shows their timing, the first Riedel-shear occurring at the far end away from the moving back-wall, the next one in the centre and then at the back-wall. Overlapping shears are shown as an increase (more blueish colours), since the width of both shears gets added up.

Fig. 3.4 shows the average width of the shear zone for each displacement increment, calculated by simply averaging along the profile lines that compose the width map of fig. 3.3. It serves as a 1D-proxy for localisation. Average shear zone width increases until approximately 6 mm of back-wall displacement and then decreases towards a stable state which it achieves after about 15 mm back-wall displacement in total. Based on the known material behaviour of sand featuring strain hardening and weakening associated with localisation (Lohrmann et al., 2003; Ritter et al., 2016), we expect this localisation proxy to correlate with the measured bulk force.

Dynamic observations and correlation with structural evolution

In fig. 3.4 back-wall force is plotted against back-wall displacement. The curve shows a clear hardening – weakening behaviour: At the start of the experiment, force increases quickly towards a maximum value, after which it decreases again, to finally reach a stable plateau. The total decrease with respect to the maximum value is roughly 20 %. Similar behaviour has been observed in axial (Kolymbas and Wu, 1990) and ring-shear tests (Lohrmann et al., 2003; Ritter et al., 2016). The maximum force is measured at about 5 mm of back-wall displacement, which is shortly before we observe at the surface the localised shear zone forming in the centre of the sand pack (fig. 3.3), close to the time of maximum surface shear zone width (fig. 3.4) and at the onset of formation of the second, isolated Riedel-shear.

The temporal relation between average fault width (strain localisation) and back-wall force (hardening – weakening) is displayed in fig. 3.5. It shows a four-phase evolution: 1. the shear zone widens and simultaneously hardens (steep increase of the curve); 2. hardening continues without further widening; 3. the shear zone narrows again (strain localisation) at the same time as the weakening begins (curve descending to the left); 4. the force remains constant while the shear zone width slightly changes up and down, due to different segments of the final shear zone becoming active and inactive in turns.

3.3.2 Compressional wedge experiment

In this experiment a flat layer of sand is used that is initially 20 mm thick. It is overlying a detachment horizon made of a 5 mm thick layer of glass micro beads which are resting on a base made of sand paper. The velocity of the indenting back-wall is 0.5 mm s^{-1}; the image recording rate of the camera is set to 1 Hz. The effective spatial resolution of the camera images is 0.2 mm px^{-1}.

Kinematic observations

While the indenter progresses, a compressional wedge forms in front of it. The wedge is bounded by an initially straight frontal thrust and oblique ramps along the sides that are connecting the frontal thrust to the indenter edges. The frontal thrust

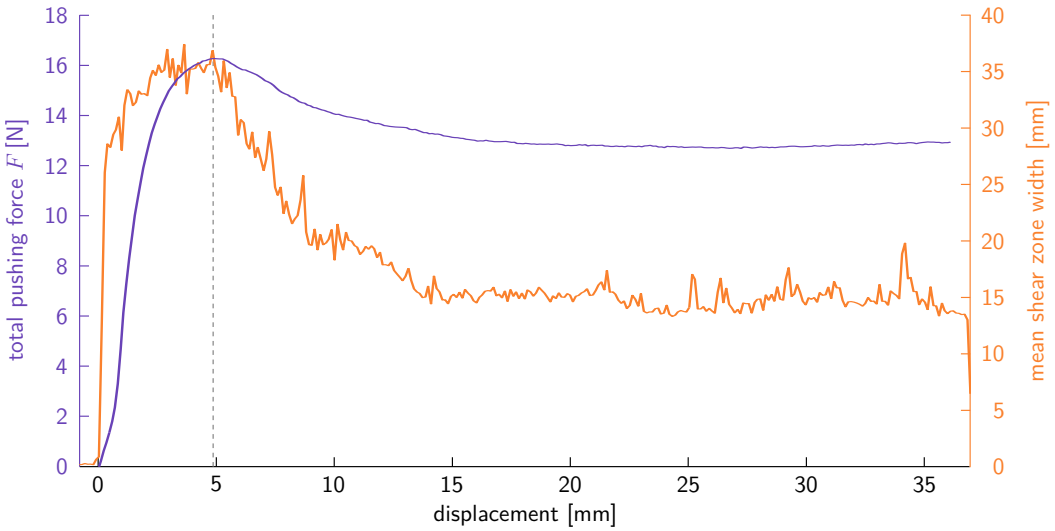

Fig. 3.4: 1-D average of shear zone width (orange, right axis), calculated as arithmetic mean of all points from the width map for a given displacement increment. The reduction to 1-D is necessary to compare width to force. Evolution of back-wall-force during the strike-slip experiment (violet, right axis), as function of back-wall displacement. The plot shows the typical hardening-weakening behaviour of sand. The structural complexity observable in the model as several Riedel-shears is not reflected in the force.

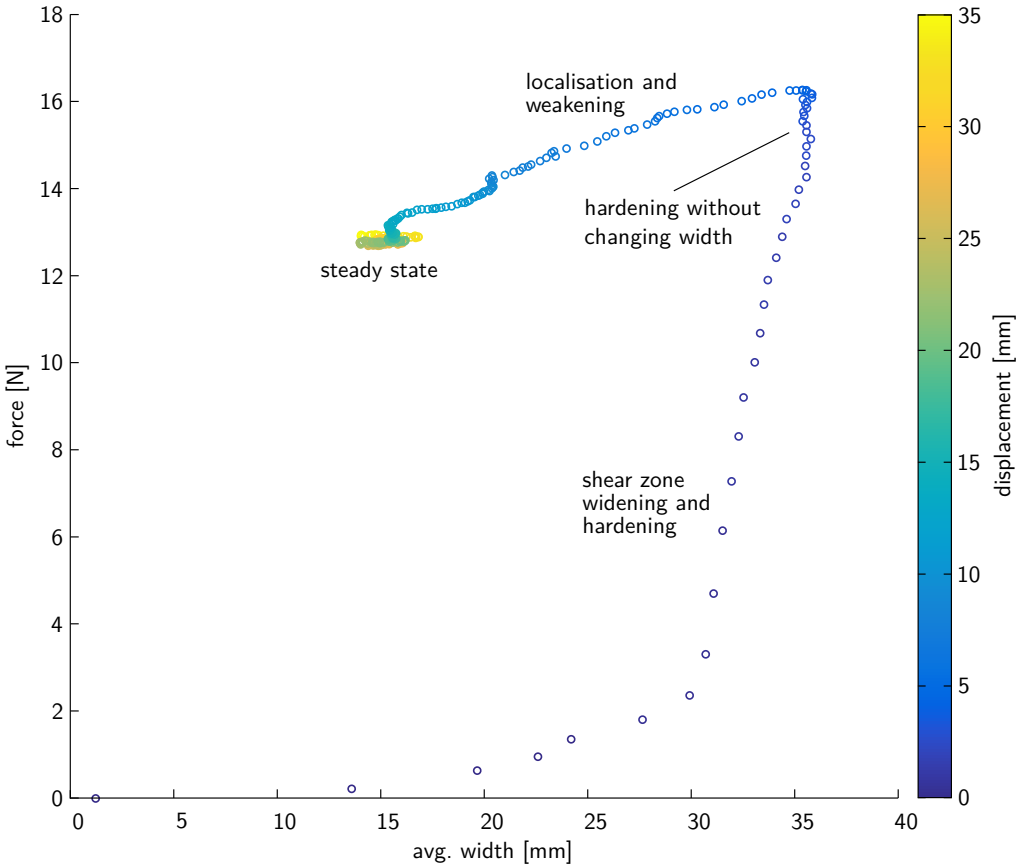

Fig. 3.5: Temporal relation of bulk force and average shear zone width for the strike-slip experiment. The plot shows hardening (increase of force) to coincide with de-localisation (increase of width), and weakening to coincide with localisation. The transition from hardening to weakening happens at the same time as the onset of localisation. Prior to localisation a period of stagnant shear zone width can be observed.

develops a slight curvature over time. Accretion of material occurs typically through several cycles, each beginning with the formation of a new thrust fault and two ramp segments, followed by accommodation of convergence along the fault, translation along the ramps and the building of topography. A new cycle begins with the renewed localisation of strain ahead of the active front and formation of the next thrust-ramp system.

The data derived from DIC allows us to zoom in and analyse the processes during formation of a single thrust fault. In accordance with literature (Dotare et al., 2016) we divide the formation of a thrust (i. e. one accretionary cycle) into four stages (fig. 3.6). In the first stage, stage 0, the old thrust is active and all displacement is localised onto it. This is followed by a stage during which most deformation is still localised onto the old thrust, but some is also distributed in the foreland of the wedge (stage 1). The zone of distributed deformation is approximately 5 cm wide, and the amount of deformation tapers out away from the wedge. In stage 2, a new thrust localises in front of the wedge and within the area of diffuse deformation, which immediately ceases. However, there is still activity on the old thrust, as different displacements of the new and the old part of the wedge show. This difference could alternatively be due to a backthrust forming at the toe of the wedge, which in top view could not be distinguished. In stage 3 the formation of the new thrust is finished and activity on the old thrust has nearly stopped. Stage 3 would at the same time be stage 0 of a new accretionary cycle.

Dynamic observations and correlation with structural evolution

Fig. 3.7 shows the back-wall force as a function of back-wall displacement along with the total area of the active wedge (A_{tot}) as a 1-D proxy for strain due to wedge growth. It is calculated by summing up the area of all pixels whose norm of the displacement is above a threshold of 12 µm, which is the noise level determined from the still images taken prior to the experiment. The stages of the accretionary cycle defined above can be easily identified in fig. 3.7: During stage 0, A_{tot} is slightly decreasing due to minor internal shortening of the wedge that is accommodated by reactivation of older thrusts or distributed deformation. In stage 1, a rapid increase of A_{tot} shows the period of diffuse deformation ahead of the wedge, whereas localisation onto the new thrust during stage 2 is reflected by a decrease of A_{tot}. Stage 3 is again characterised by a slightly decreasing A_{tot}, although at a higher level than during stage 0.

The back-wall force (fig. 3.7) shows three characteristics: A long-term trend of increasing force, on top of which midterm periods of transiently increased rate of force build-up occur that are followed by short-term force drops. The long-term trend defines a constant rate of force build-up that is consistent with growth of the wedge in mass and the consequent increase in basal drag. Based on known material behaviour of sand, the transient increase of forces followed by a force drop likely

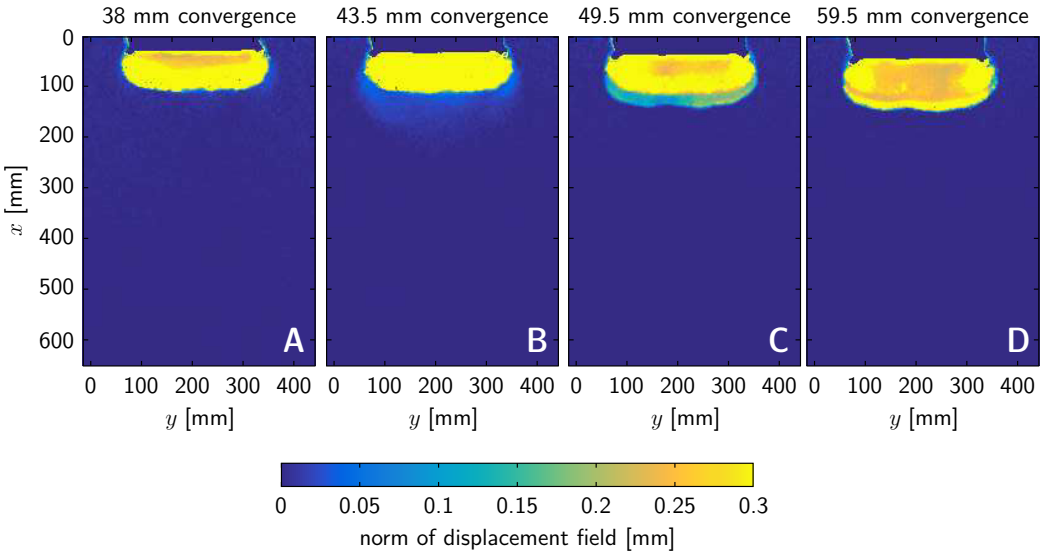

Fig. 3.6: Maps showing the displacement (norm of displacement field) in indenter experiments in top view. The indenter is moving at a constant convergence rate of 0.5 mm s^{-1} from top to bottom. The sequence shows the initiation of a thrust fault in four stages: In stage 0 (**A**) the old thrust fault is active and all deformation is localised onto it, which is visible as a sharp transition from yellow to blue colours. In stage 1 (**B**) most deformation is still localised onto the thrust but some is also diffusely distributed in the footwall in front of the wedge. This is visible in the map as light blue halo around the yellow patch. The zone of diffuse deformation reaches approximately 10 cm ahead of the active thrust and the amount of deformation decreases away from the wedge. Stage 2 (**C**): A new thrust fault has just formed in front of the old one, in the area where previously the diffuse deformation had occurred. Diffuse deformation has ceased, and the area covered by the new thrust fault is significantly less than the one covered previously by diffuse deformation (2.5 cm ahead of the previous thrust). Both thrust faults are still active in this picture, recognisable as displacement contrast between the two parts of the wedge. Alternatively, this displacement contrast could be due to activity on a possibly existing backthrust instead of the old thrust. In stage 3 (**D**) relative displacement between the two parts of the wedge has nearly ceased and almost all deformation is localised onto the new thrust.

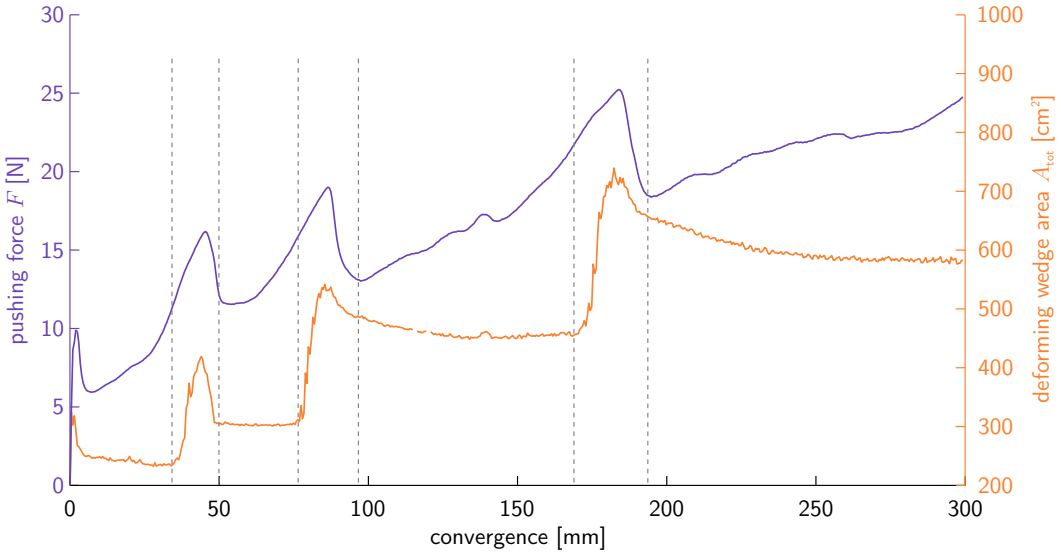

Fig. 3.7: Area of the actively deforming region of the wedge (green, right axis). The initiation of new thrusts is clearly visible as a drastic increase of area, followed by a decrease to a level still higher than before propagation. The increase reflects the period of diffuse deformation and the subsequent decrease reflects the localisation onto a new thrust. Corresponding force evolution as measured at the indenter is shown in violet (left axis). Each new thrust is characterised by a steep increase of force prior to localisation, followed by a force drop during localisation. The overall increasing trend reflects the increasing frictional strength on the thrust and basal detachment due to growth of the wedge. Although the size of the wedge grows in a step-wise manner, the increase of force is smooth and gradual (except for the propagation events).

reflects strain-hardening and -weakening during localisation of a new thrust – ramp system. Accordingly, the peaks made by transient force increases and subsequent force drops are generally correlated to, but broader than, the corresponding peaks of A_{tot}. Force build-up starts already before the diffuse deformation of stage 1 can be seen optically. However, the subsequent force-drop coincides rather well with stage 2.

The covariation of force and A_{tot} is synoptically visualised in fig. 3.8, in which these two variables are plotted against each other. The plot shows a recurring pattern in which each cycle of the graph represents an accretionary cycle of the sand wedge. A cycle begins with the build-up of stress, visible as slow increase of back-wall force while A_{tot} first decreases slightly and then stagnates. This is stage 0 of wedge growth (sub-vertical part of the graph). It is followed by a rapid increase of A_{tot}, during which the back-wall force further increases (stage 1, nearly horizontal part of the graph). The increase of A_{tot} becomes faster and larger with every cycle, which is indicated by the respective sections of the graph becoming shallower and longer every time. Stage 2, localisation, is characterised by a decrease of A_{tot}. The small loop at the transition from stage 1 to stage 2 indicates that during the first few increments of localisation the force still increases, i. e. the force drop lags behind the localisation. At the end of localisation the decrease of (A_{tot}) shortly pauses before convergence on the newly formed thrust sets in and force increases again (stage 3).

3.4 Discussion

3.4.1 Strike-slip Experiment

In the strike-slip experiment we observe initially diffuse deformation in combination with hardening registered at the force sensor. At the onset of localisation in the centre of the shear zone, hardening changes to weakening. This is in accordance with observations from mechanical testing and experiments in granular physics (Lohrmann et al., 2003; Rechenmacher, 2006), where the hardening – weakening behaviour has been attributed to reorganisation of grains and the build-up and subsequent break-down of force chains within the material. Lohrmann et al. (2003) observed the onset of weakening to correlate with the maximum dilation rate of their samples, which they interpreted as measure for localisation. In our experiments, however, the onset of weakening and the onset of directly observed localisation coincide. Additionally, in our experiment most of the internal complexity of shear zone evolution, which includes rotation and linkage of several shear zones, is not reflected in the force measurements. These differences are likely due to the strong kinematic boundary condition of a pre-existing basal discontinuity: As shown by Ueta et al. (2000), the developing Riedel shears are always linked down to the through-going, localised shear zone at the base. Therefore, deformation is essentially of the mode-III type ("tearing"). This involves the crack front propagating perpendicular to the direction

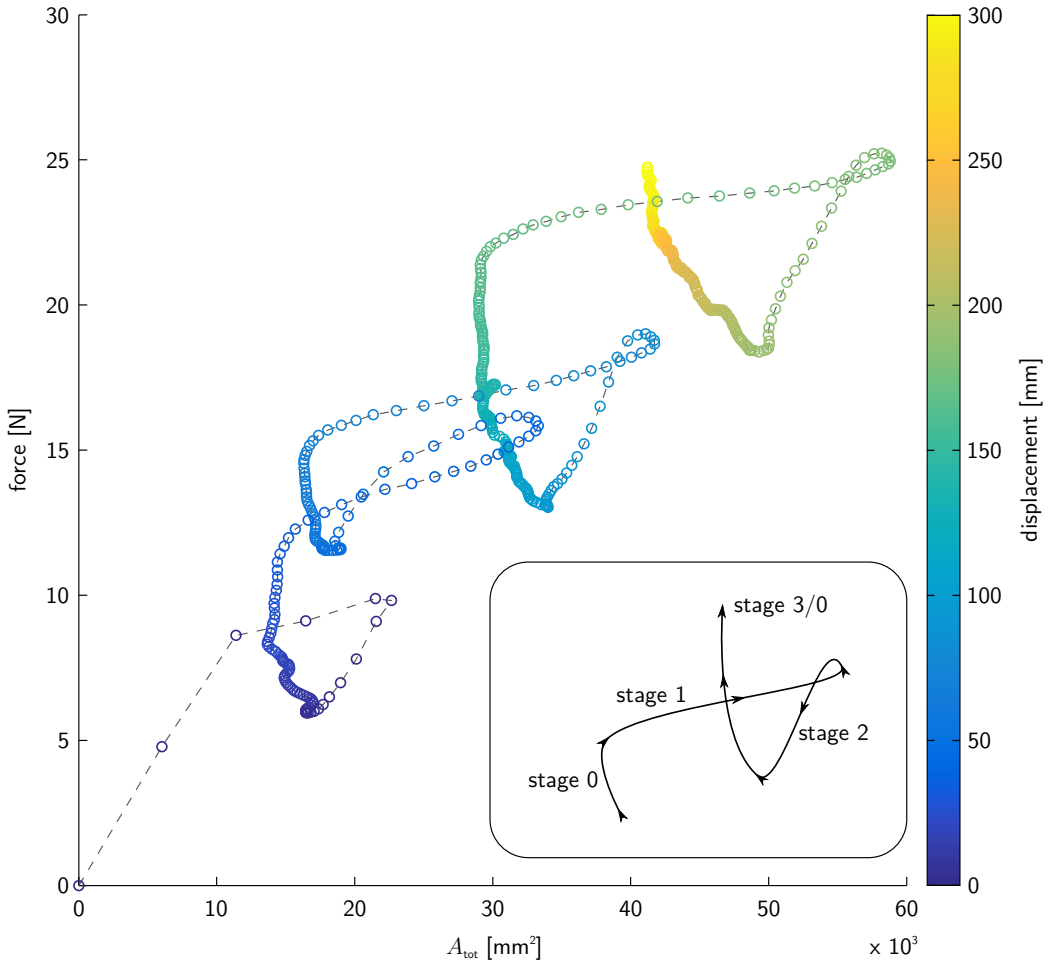

Fig. 3.8: Plot showing the temporal relation of back wall force and deformation, represented by the area of the deforming region. The distance between two circles is always 0.5 mm of displacement, i. e. the wider the circles' spacing along one axis, the quicker is the change of the respective property. The plot shows a cyclic pattern, in which each cycle can be attributed to the formation of one thrust fault. A cycle begins with the slow increase of force while the deforming area slightly decreases (sub-vertical parts of the graph). This is stage 0 of the thrust formation, during which the wedge grows in a self-similar way. It is followed by a sudden increase of the deforming area, during which the force still increases. This is stage 1 of the wedge (diffuse deformation, nearly horizontal part of the graph). At the end of stage 1 deformation begins to localise (deforming area decreases). Only after the onset of localisation the force starts to drop. Localisation takes several tens of seconds, during which force and deforming area decrease at a constant ratio (stage 2). At the end of the localisation a new cycle begins (stage 3).

of deformation, which in our case can be translated to localisation propagating from the basal shear zone upwards. The degree of localisation observed (i. e. the average shear zone width) is thus rather a measure of how close the "crack front" is to the surface than describing accurately the deformation within the sand pack.

Contrasting with this, the force measurements are integrating the hardening–weakening behaviour over the entire volume of the sand pack. We presume that weakening in this bulk measure occurs when the volume that is undergoing weakening exceeds the volume that is still undergoing hardening, which is probably the case when localisation is halfway through the sand pack. Consequently we speculate that the good correlation between average shear zone width and force drop observed in fig. 3.5 is rather coincidental and depends on the distance between the surface of the sand pack and its centre, i. e. its thickness.

To truly link the optical observations to a force evolution, a set-up needs to be designed in which the propagation of deformation occurs in a direction that can be optically observed. In case of a strike-slip shear zone that is observed from the top this means deformation must propagate horizontally, resulting in mode-II deformation ("shearing"). We designed such a set-up by removing the basal plate from the Riedel set-up and pushing a part of the sand layer directly over a thin layer of silicone oil without a pre-existing basal shear zone. In chapter 4 we will use this modified set-up to investigate the interplay of localisation and weakening.

3.4.2 Compressional wedge experiment

In the compressional wedge experiment we observe cyclic thrust propagation, in which the formation of each new thrust is preceded by a stage of diffuse deformation in front of the current thrust, similar to what was observed by Adam et al. (2005). Dotare et al. (2016) showed through high-resolution imaging that this initial stage of diffuse deformation is in fact composed of localised deformation along several ephemeral shear zones. They divided the initiation of a new thrust into four stages, which we are able to recognise in our experiment.

The two studies cited above drew an analogy to results from Ring-shear tests (Lohrmann et al., 2003) in which a phase of compaction and associated hardening was observed. According to this analogy the diffuse or ephemerally localised deformation corresponds to the compaction phase and thus to hardening. With our combined approach we are now for the first time able to directly observe the correlation between hardening and localisation. Our force measurements, however, show that hardening starts prior to visible deformation. Notably, this time lag becomes more pronounced with each accretionary cycle. During this first part of the hardening period, we interpret, deformation is partly accommodated through reactivation of older thrusts that are now within the wedge. Only when this reactivation potential is exploited does the wedge attain an internal strength that is high enough for the formation of an additional fault being energetically favourable.

While hardening precedes the onset of diffuse deformation, weakening seems to lag behind the onset of localised deformation, as visualised by the small loops in fig. 3.8 between stages 1 and 2. This can be related to the episodic behaviour of localisation, which in fig. 3.7 can be recognised by the flat peaks in the curve showing deforming area: A_{tot} increases to a certain value, which it retains while hardening still continues. It then quickly decreases, with the rate of decrease being maximal directly after the plateau. The onset of weakening thus coincides with the maximum rate of localisation. This is in accordance with results from mechanical testing (Lohrmann et al., 2003), but had never been observed at the larger scale of accretionary wedges.

3.5 Conclusion

We developed an experimental device that facilitates simultaneous measurements of stress and strain in analogue experiments. We tested this device in two different tectonic settings, a strike-slip one and a convergent one. For the strike-slip setting we find that the classical Riedel-type set-up that we applied is not ideally suited for investigating the interplay of mechanical and kinematic behaviour, due to the dominating kinematic boundary condition. This leads to vertical propagation of deformation, which is thus not observable.

In the accretionary wedge set-up we are able to observe a correlation between hardening and diffuse deformation that so far had been only inferred. Additionally, we observe a time lag between strain localisation and strain weakening that we interpret to be a consequence of the episodic character of deformation.

In total, our experiments show that simultaneous observation of deformation and force at high resolution are feasible and can provide valuable new insights into links between processes which so far had only been investigated individually.

Acknowledgements

Thomas Ziegenhagen and Frank Neuman are thanked for the design and engineering of the experimental set-up. Malte C. Ritter and Karen Leever are supported by the Helmholtz Graduate School GeoΣim. Tasca Santimano is supported by the European Union FP7 Marie Curie ITN project TOPOMOD (project #264517).

References

Adam, J., J. L. Urai, B. Wieneke, O. Oncken, K. Pfeiffer, N. Kukowski, J. Lohrmann, S. Hoth, W. van der Zee and J. Schmatz (2005): 'Shear localisation and strain distribution during tectonic faulting—new insights from granular-flow experiments and high-resolution optical image correlation techniques'. In: *Journal of Structural Geology* 27.2, pp. 283–301. DOI: 10.1016/j.jsg.2004.08.008.

Cloos, H. (1928): 'Experimente zur inneren Tektonik'. In: *Centralblatt für Mineralogie, Geologie und Paläontologie*, pp. 609–621.

Cubas, N., C. Barnes and B. Maillot (2013): 'Inverse method applied to a sand wedge: Estimation of friction parameters and uncertainty analysis'. In: *Journal of Structural Geology* 55, pp. 101–113. DOI: 10.1016/j.jsg.2013.07.003.

Cubas, N., Y. M. Leroy and B. Maillot (2008): 'Prediction of thrusting sequences in accretionary wedges'. In: *Journal of Geophysical Research* 113.B12, B12412. DOI: 10.1029/2008JB005717.

Cubas, N., B. Maillot and C. Barnes (2010): 'Statistical analysis of an experimental compressional sand wedge'. In: *Journal of Structural Geology* 32.6, pp. 818–831. DOI: 10.1016/j.jsg.2010.05.010.

Dooley, T. P. and G. Schreurs (2012): 'Analogue modelling of intraplate strike-slip tectonics: A review and new experimental results'. In: *Tectonophysics* 574-575, pp. 1–71. DOI: 10.1016/j.tecto.2012.05.030.

Dotare, T., Y. Yamada, J. Adam, T. Hori and H. Sakaguchi (2016): 'Initiation of a thrust fault revealed by analog experiments'. In: *Tectonophysics* 684, pp. 148–156. DOI: 10.1016/j.tecto.2015.12.023.

Graveleau, F., J. Malavieille and S. Dominguez (2012): 'Experimental modelling of orogenic wedges: A review'. In: *Tectonophysics* 538-540, pp. 1–66. DOI: 10.1016/j.tecto.2012.01.027.

Herbert, J. W., M. L. Cooke, P. Souloumiac, E. H. Madden, B. C. Mary and B. Maillot (2015): 'The work of fault growth in laboratory sandbox experiments'. In: *Earth and Planetary Science Letters* 432, pp. 95–102. DOI: 10.1016/j.epsl.2015.09.046.

Klinkmüller, M., G. Schreurs, M. Rosenau and H. Kemnitz (2016): 'Properties of granular analogue model materials: A community wide survey'. In: *Tectonophysics* 684, pp. 23–38. DOI: 10.1016/j.tecto.2016.01.017.

Kolymbas, D. and W. Wu (1990): 'Recent results of triaxial tests with granular materials'. In: *Powder Technology* 60.2, pp. 99–119. DOI: 10.1016/0032-5910(90)80136-M.

Lohrmann, J., N. Kukowski, J. Adam and O. Oncken (2003): 'The impact of analogue material properties on the geometry, kinematics, and dynamics of convergent sand wedges'. English. In: *Journal of Structural Geology* 25.10, pp. 1691–1711. DOI: 10.1016/S0191-8141(03)00005-1.

Nieuwland, D. A., J. L. Urai and M. Knoop (2000): 'In-situ stress measurements in model experiments of tectonic faulting'. In: *Aspects of Tectonic Faulting*. Ed. by F. K. Lehner and J. L. Urai. Berlin, Heidelberg: Springer Berlin Heidelberg, pp. 155–166. DOI: 10.1007/978-3-642-59617-9_8.

Panien, M., G. Schreurs and O. A. Pfiffner (2006): 'Mechanical behaviour of granular materials used in analogue modelling: insights from grain characterisation, ring-shear tests and analogue experiments'. English. In: *Journal of Structural Geology* 28.9, pp. 1710–1724. DOI: 10.1016/j.jsg.2006.05.004.

Rechenmacher, A. L. (2006): 'Grain-scale processes governing shear band initiation and evolution in sands'. In: *Journal of the Mechanics and Physics of Solids* 54.1, pp. 22–45. DOI: 10.1016/j.jmps.2005.08.009.

Riedel, W. (1929): 'Zur Mechanik geologischer Brucherscheinungen'. In: *Centralblatt für Mineralogie, Geologie und Paläontologie*, pp. 354–368.

Ritter, M. C., K. Leever, M. Rosenau and O. Oncken (2016): 'Scaling the sandbox — Mechanical (dis-) similarities of granular materials and brittle rock'. In: *Journal of Geophysical Research: Solid Earth* 121.9, pp. 6863–6879. DOI: 10.1002/2016JB012915.

Santimano, T. (2016): 'Kinematic complexity of accretionary wedges – Insights from analogue models towards understanding natural wedges'. Dissertation. Freie Universität Berlin, p. 107.

Schreurs, G., R. Hanni, M. Panien and P. Vock (2003): 'Analysis of analogue models by helical X-ray computed tomography'. In: *Geological Society, London, Special Publications* 215.1, pp. 213–223. DOI: 10.1144/GSL.SP.2003.215.01.20.

Souloumiac, P., B. Maillot and Y. Leroy (2012): 'Bias due to side wall friction in sand box experiments'. In: *Journal of Structural Geology* 35, pp. 90–101. DOI: 10.1016/j.jsg.2011.11.002.

Ueta, K., K. Tani and T. Kato (2000): 'Computerized X-ray tomography analysis of three-dimensional fault geometries in basement-induced wrench faulting'. In: *Developments in Geotechnical Engineering* 84.C, pp. 233–246. DOI: 10.1016/S0165-1250(00)80019-X.

4 Growing Faults in the Lab: Insights into the Scale Dependence of the Fault Zone Evolution Process

Abstract

Analogue sandbox experiments of strike-slip deformation show the work required to create a fault system, W_{prop}, to scale approximately with the square of the fault system length, l. This is consistent with theory of fault growth in nature. Through quantitative measurements of both W_{prop} and strain, we are able to show that W_{prop} is mainly spent on diffuse deformation prior to localisation, which we regard as analogous to distributed deformation on small-scale faults below seismic resolution in natural fault networks. We show the strain threshold at which localisation occurs to be a function of l, whereas the total stress drop remains independent of system size.

4.1 Introduction

Localisation of strain into discrete shear zones and fault networks is a characteristic feature in the deformation of Earth materials on all scales from single grains to tectonic plates. In laboratory experiments on brittle rock the localisation of strain into cracks and their subsequent coalescence to a through-going fracture are closely linked to a decrease of material strength known as strain weakening (Brady et al., 1973; Lockner et al., 1991; Scholz, 2002; Paterson and Wong, 2004). On the larger scale of entire sedimentary basins strain localisation can be observed as deformation being initially distributed onto several small faults and subsequently concentrating onto one master fault (e. g. McLeod et al., 2000; Cowie, Underhill et al., 2005). In the Andes, Oncken et al. (2012) were able to link this reduction of the number of active faults to a concurrent decrease of crustal strength. Their study uses field data to convincingly show the general behaviour; however, the scarcity of geological data and the accuracy of available dating methods make it difficult to understand in detail the process of localisation and its quantitative relation to strength evolution. Scaling laws

Manuscript in preparation, with authors: Malte C. Ritter, Matthias Rosenau, Onno Oncken.
Individual Contributions: M. C. R. planned and performed research, carried out experiments and analysed results, wrote the paper; M. R. participated in writing the paper; O. O. supervised the research.

have been employed to derive estimates regarding slip on faults below the resolution of a dataset (Scholz and Cowie, 1990), but their results remain untested.

Scaled analogue sandbox experiments provide physical models in which the processes of interest can be observed directly and practically without limitations of resolution apart from the particle size of the selected material. Previous experiments have shown a phase of diffuse (Adam et al., 2005) or ephemerally localised (Dotare et al., 2016) deformation to precede formation of localised faults in sand. This can be linked to global material hardening (Lohrmann et al., 2003; Rechenmacher, 2006) and is thus an essential part of the localisation process (Tordesillas and Muthuswamy, 2009). By analogy it has been related to distributed deformation preceding localisation in nature (e. g. Dotare et al., 2016). However, quantitative proof for this analogy is still missing.

Furthermore, the energy budget of the localisation process has recently received increased attention, due to its application in predicting fault growth through minimum-work models (Mitra and Boyer, 1986; Hardy et al., 1998; Masek and Duncan, 1998; Cooke and Murphy, 2004; Dempsey et al., 2012; Cooke and Madden, 2014). In this context the work of fault propagation, W_{prop}, is recognised as the crucial parameter determining strain distribution and -localisation (Del Castello and Cooke, 2007). As usual in these studies, we define W_{prop} to be the work per unit height of the fault, where height refers to the in-plane extent of the fault perpendicular to the slip direction. The unit of W_{prop} is thus $\mathrm{J\,m^{-1}}$. The common estimate used in all the above studies assumes W_{prop} to depend on the volume of the fault zone. Its width depends on the displacement on the fault (e. g. Scholz, 1987) and thus on fault length l (Cowie and Scholz, 1992; Dawers et al., 1993). This leads to an overall scaling of fault zone volume, and thus W_{prop}, with l^2.

In contrast to this, shear zone width in sandbox experiments is depending on grain size and is otherwise constant (Panien et al., 2006). Accordingly, Herbert et al. (2015) have reported results from which W_{prop} can be deduced to be directly proportional to l, although this relationship was not in the focus of their study. If this linear relationship is valid, it carries severe implications for the applicability of sandbox experiments to understanding natural systems.

To resolve these issues we carry out analogue sandbox experiments varying the fault system length l systematically over a wide range. By determining diffuse deformation and W_{prop}, as well as their mutual relation, we show that diffuse deformation in sandbox experiments is indeed analogous to distributed deformation in natural fault systems. Our data also verifies the scalability of sandbox models with respect to energy, i. e. it shows a similar scaling of W_{prop} with fault length as in nature. In order to facilitate the formation of a sufficiently large fault system, we choose the tectonic setting of strike-slip deformation, in which l (defined here as the extent in slip direction) is not limited by crustal thickness. To further extend the range of l, we complement these experiments with measurements in a Ring-Shear tester that facilitates very precise measurements of forces for short l at the cost of not allowing direct observation of the shear zone.

4.2 Experimental Approach

4.2.1 Analogue Material

The analogue material used in this study is quartz sand of type G23T, which is the standard sand used for analogue modelling at GFZ Potsdam. It is a medium-grained and moderately sorted fluvial sand with rounded grains (mean grain size 300 µm). Standard mechanical testing has been carried out on this sand by Klinkmüller et al. (2016) and Ritter et al. (2016, cf. chapter 2), among others. The latter study found tectonic models using this material to be scaled for a length scaling factor of $l^* = 2 \times 10^{-6}$, i. e. for the case of 1 cm in the model relating to 5 km in the natural prototype.

4.2.2 Deformation Rigs

Strike-Slip Shear Box

The strike-slip shear box is a custom built apparatus that is based on the deformation rig introduced in chapter 3. It essentially consists of a sand pack, one part of which is pushed forward by a combination of an indenter and a moving sidewall, while the other part is held in place by a stationary back- and sidewall (fig. 4.1). The sand pack is resting on a layer of low-viscosity silicone oil that, in combination with a low deformation rate of 30 µm s^{-1}, reduces the basal traction to approximately 10 Pa. This is about 4 % of the average sand strength and thus enables the sand pack to be pushed forward as a whole without internal thrusting (average sand strength $\tau_{\mathrm{prop}} = 0.5\,\mu\sigma_{\mathrm{n}} = 0.5\,\rho g h \mu \approx 255\,\mathrm{Pa}$). A strike-slip shear zone develops between the edges of the indenter and the stationary back-wall. The force required to push the indenter forward is measured by a sensor attached to it (sampling rate: 1 kHz), and a digital camera captures images of the sand pack's surface (rate of recording: 1 Hz), from which the surface deformation field is calculated by means of DIC (Digital Image Correlation).

The fundamental novelty of this shear box is the total absence of any pre-existing basal shear boundary condition, either distributed or discrete, which distinguishes it from the typical Riedel-type shear box and its derivates (Dooley and Schreurs, 2012). Such basal shear zone would result in mode-III deformation of the sand pack and vertical propagation of the already localised basal shear zone (cf. chapter 3). Here only the starting and ending points are given as stress singularities, between which a fault can freely develop. This leads to mode-II deformation and does not prescribe localisation away from the end points.

In all strike-slip experiments presented here the sand pack is 50 mm high and 750 mm wide. The sand is sifted into the box to ensure a reproducibly high density, and it is levelled by carefully scraping off the topmost approximately 1 mm to a uniform height. The variable parameter is the initial distance between indenter and

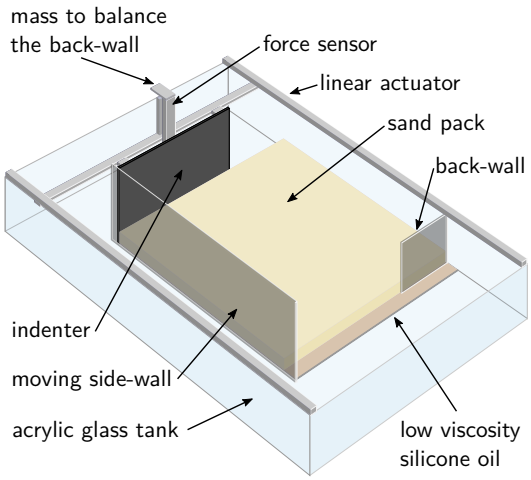

Fig. 4.1: Experimental set-up for strike-slip experiments (SL). The sand pack is pushed by the indenter moving at a constant velocity. Due to a layer of low viscosity silicone oil the drag at the base of the sand pack is very small (≈10 Pa), such that when pushed the sand pack moves as a whole. A stationary back-wall holds back a part of the sand pack, which causes a shear zone to develop between the edges of the indenter and the back-wall. The parameters recorded are the force needed to push the indenter and its displacement. Additionally, a stereoscopic camera system (not shown) mounted above the set-up monitors the surface deformation of the sand pack.

stationary back-wall, which is the fault system length l. It is set to $l = 200\,\mathrm{mm}$, $l = 300\,\mathrm{mm}$ and $l = 400\,\mathrm{mm}$ in this study.

Ring-Shear Tester

In order to extend the range of l towards lower values we carry out complementary experiments in a ring-shear tester (RST). The RST is an industrial standard device (model *RST-01.pc*, manufactured by *Dr.-Ing. Dietmar Schulze Schüttgutmesstechnik, Wolfenbüttel, Germany*) that has already been used in several other studies in the analogue modelling community (e. g. Lohrmann et al., 2003; Panien et al., 2006; Klinkmüller et al., 2016; Ritter et al., 2016). It was first introduced by Schulze (1994). The RST consists of an annular shear cell and a matching lid between which the sample is contained. The shear cell is 40 mm high; it has an inner radius of 50 mm and an outer radius of 100 mm. The lid is pressed onto the sample at a preset normal load, σ_n. The shear cell is then rotated (angular velocity $\omega = 0.39\,\mathrm{rad\,s^{-1}}$, corresponding to an average shearing velocity $v = 0.5\,\mathrm{mm\,s^{-1}}$) while the lid is kept stationary by tie rods (fig. 4.2). Thereby the sample is sheared. Sensors record the torque and the normal load applied to the lid, as well as its vertical displacement due to volume changes of the sample.

The lid is equipped with small radial blades pointing vertically downwards from its base to provide sufficient mechanical coupling with the sample. These blades are 5 mm high and extend over the whole width of the ring. Upon rotating the shear cell, shear zones will nucleate at the tip of each of these blades and propagate towards the respective next one. The distance between two such blades is therefore the equivalent to the fault system length l in the strike-slip set-up and the parameter we vary in this study. We define the average circumferential distance between two blades as the

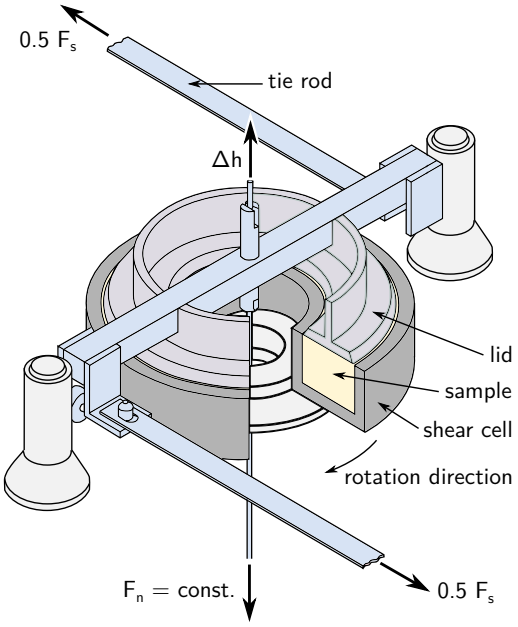

Fig. 4.2: Experimental set-up for ring-shear tests (RST). The sample is sifted into the shear cell, which is then covered with the lid. A constant normal load is applied to the lid and the shear cell is rotated at a constant angular velocity, while the lid is kept stationary by tie rods. Radial vertical blades at the base of the lid (not shown) ensure mechanical coupling between lid and sample. The spacing l of these blades is varied between experiments. Sensors register the shear force F_s, the normal load F_n and the decompaction of the sample Δh. Modified from Schulze (1994).

distance along the imaginary circumferential line that separates the surface of the lid into two parts of equal area. For the sake of simplicity we will call this the "blade distance" from here on.

In the standard configuration of the lid there are 20 blades ($l = 24.4\,\mathrm{mm}$). From this configuration blades were removed systematically, to realise blade distances of $l = 48.8\,\mathrm{mm}$ (10 blades) and $l = 97.6\,\mathrm{mm}$ (5 blades). Samples are sifted into the shear cell and then scraped off to the correct height. Normal load is set to $\sigma_\mathrm{n} = 500\,\mathrm{Pa}$ and is constant over the entire fault plane, whereas slip rate increases outwards.

Deformation in the RST is not strike-slip deformation sensu strictu, since the shear plane is horizontal. However, it is plane-strain, mode-II deformation with a negligible vertical component. We therefore regard it as equivalent to strike-slip for our purposes.

Kinematic and Mechanical Differences Between the Set-Ups

Deformation in the two experimental set-ups is different to some degree: In the strike-slip box, normal load across the shear zone is due to lithostatic load, which increases from 0 Pa at the surface to approximately 850 Pa at the bottom of the sand pack. Thus, there is a gradient of normal load across the fault from the surface to the bottom. At the same time, the slip rate is constant over the entire height of the sand pack. This is exactly opposite in the RST, where a constant normal load of 500 Pa is applied on the entire fault surface by the lid, while the slip rate

increases outwards due to constant angular velocity. Since deformation of sand follows a velocity-independent Coulomb-type rheology (e. g. Lohrmann et al., 2003), we presume the slip rate gradient in the RST to not affect our measurements. The gradient of normal load, on the other hand, has a direct influence on fault strength, which in this case increases with depth. However, the relationship between normal load and strength is linear; thus average values for normal loads, strengths and forces should be reasonably good quasi-2D representations of the actual processes.

4.2.3 Work of Fault Propagation

According to Herbert et al. (2015) the total work balance for analogue sandbox experiments is:

$$W_{\text{ext}} = W_{\text{prop}} + W_{\text{fric}} + W_{\text{grav}}. \tag{4.1}$$

W_{ext} is the external work done on the system, W_{fric} is the frictional work along the (localised) shear zone and W_{grav} is the work done against gravity. In the case of strike-slip deformation the vertical component of deformation is negligible, such that $W_{\text{grav}} \approx 0$ in our models. The remaining parameters can be easily determined from the experiments: Measurements of bulk shear force in either experiment yield shear curves (fig. 4.3), that reveal a hardening – weakening cycle during deformation. According to Lohrmann et al. (2003), this is associated to a compaction – dilation cycle. Based on the micro-mechanical model of Tordesillas and Muthuswamy (2009) we suggest the onset of dilation to be equivalent to the onset of localisation. As can be seen from the figure, this coincides with the onset of hardening. We therefore define the work of fault propagation W_{prop} as the area under the hardening – weakening peak, and the work done in frictional sliding on the shear zone W_{fric} as the remaining area under the shear curve. Both values are normalised to fault height. Please note that our definition of W_{prop} is slightly different from other definitions that can be found in literature, which often exclude the period of hardening prior to the force maximum (e. g. Cooke and Madden, 2014; Herbert et al., 2015).

4.3 Results

4.3.1 Optical Monitoring: Diffuse versus Localised Deformation

In the strike-slip set-up a total of nine experiments were carried out for different l. Displacement fields derived from DIC are used to analyse the fault evolution in these experiments. Fig. 4.4 exemplarily shows maps of the curl of the incremental displacement field for a representative experiment with $l = 300\,\text{mm}$. The general pattern described in this example is independent of l in all experiments, as shown later.

In the beginning, deformation is diffuse and widely distributed in a sigmoidal patch between the edges of back-wall and indenter. Directly at the edges, however,

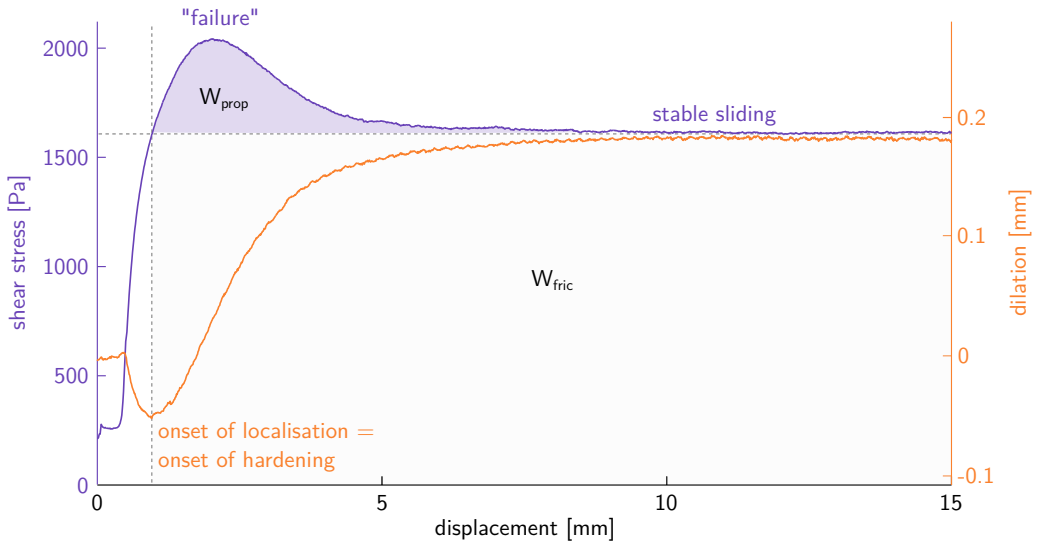

Fig. 4.3: Shear stress and (blue) and sample dilation (orange) in a ring-shear experiment at $\sigma_{\mathrm{n}} = 3\,\mathrm{kPa}$. Shear stress increases towards a maximum ("failure") and then decreases ("weakening") again towards a stable sliding stress. At the same time dilation takes place, which can be taken as a proxy for localisation. The work required for fault propagation (W_{prop}) is defined as the area under the hardening–weakening peak, as shown by the blue-shaded area, and normalised to fault height. W_{fric} is the work for continued frictional sliding on the fault, which is the area under the shear stress curve that does not belong to W_{prop}, as indicated by the grey shading.

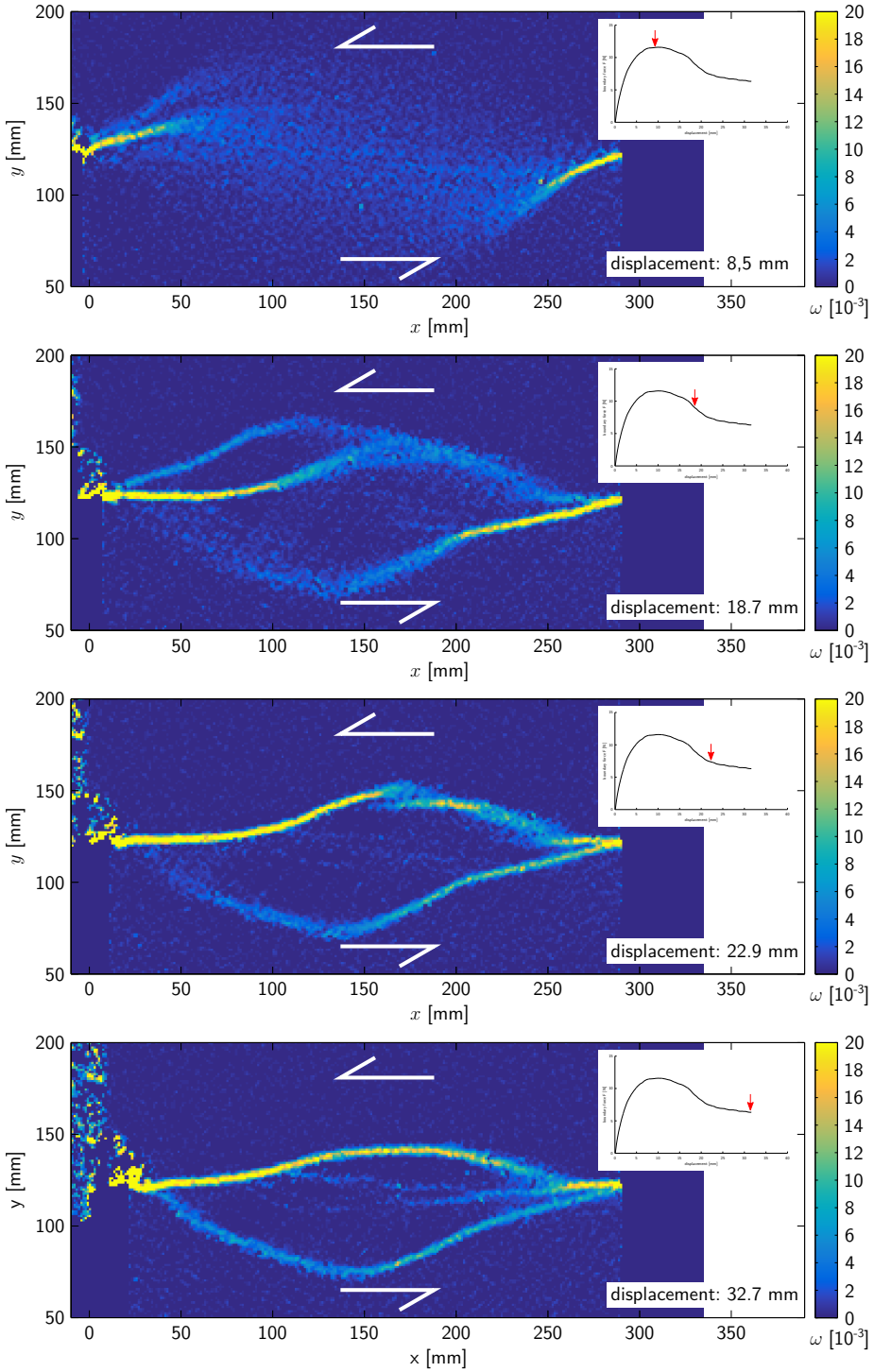

Fig. 4.4: Evolution of a shear zone in strike-slip experiments, $l = 300\,\text{mm}$. Data shown is the curl of the incremental displacement field. The shear zones evolve in a complex pattern until finally an approximately straight shear zone is formed. See text for detailed analysis.

it becomes quickly localised into narrow shear zones that are a few centimetres long. They are rotated about 25° to 30° outwards with respect to the trace of the ideal, i. e. direct, connection between the edges of indenter and back-wall. This corresponds to the angle predicted by the Mohr-Coulomb failure criterion, if one assumes the pushing direction to be equal to the direction of maximum compressive stress. In the gap between the two shear zones deformation remains diffuse.

After accumulating some more displacement without growing significantly, the two initial shear zones become replaced by new ones that are oriented closer to the direction of imposed deformation; however, their tips are still bending outwards and away from each other (fig. 4.4). The new shear zones grow in a step-wise manner and eventually become replaced by a new, even more favourably oriented one. Before a new shear zone takes over the deformation, both shear zones, new and old, show simultaneous activity for a short time span.

In this way the shear zones grow towards and around each other until they eventually connect. When they finally do so, they connect not to the other fault's tip but somewhere close to its starting point, such that there are two adjacent fault branches, both connecting back-wall and indenter. In between the two branches, slight uplift (a few millimetres) can be observed. Activity then usually ceases on the more curved branch such that one main shear zone remains. It might straighten out slightly, but apart from that, deformation appears to have reached a steady state at this point.

To compare the evolution of experiments with different l, the cumulative displacement fields at the end of the experiments are used. Fig. 4.5 shows maps of their curl for one experiment of each l. It is clear from the figures that the general behaviour of fault growth is the same independent of l: In all cases there are several distinct, abandoned shear zones at decreasing angles towards the deformation direction, and two main branches that connect to the other side. Due to the maps showing the cumulative deformation, the main shear zone at the end of the experiment cannot be clearly identified from the figure. This is only possible in the case of $l = 200\,\mathrm{mm}$ (bottom), where an additional straight and through-going shear zone forms in the centre.

To quantify the extent of diffuse and localised deformation, we measure the deformed area by counting the number of pixels that have undergone measurable deformation. We use the second component of the displacement gradient tensor ($\partial u_x/\partial y$, where u_x is displacement along strike and y is in the direction perpendicular to it) and apply the algorithm of Otsu (1979) to find the best threshold between noise and measurably deformed area. This algorithm is designed to extract features from their background in an image based on intensity histograms. Because this relies on relative intensity differences, we are able to either include or exclude diffuse deformation in the pixel counting by applying the algorithm to displacement fields at two different, well-defined points during deformation: At peak stress practically no localised deformation has taken place yet. The al-

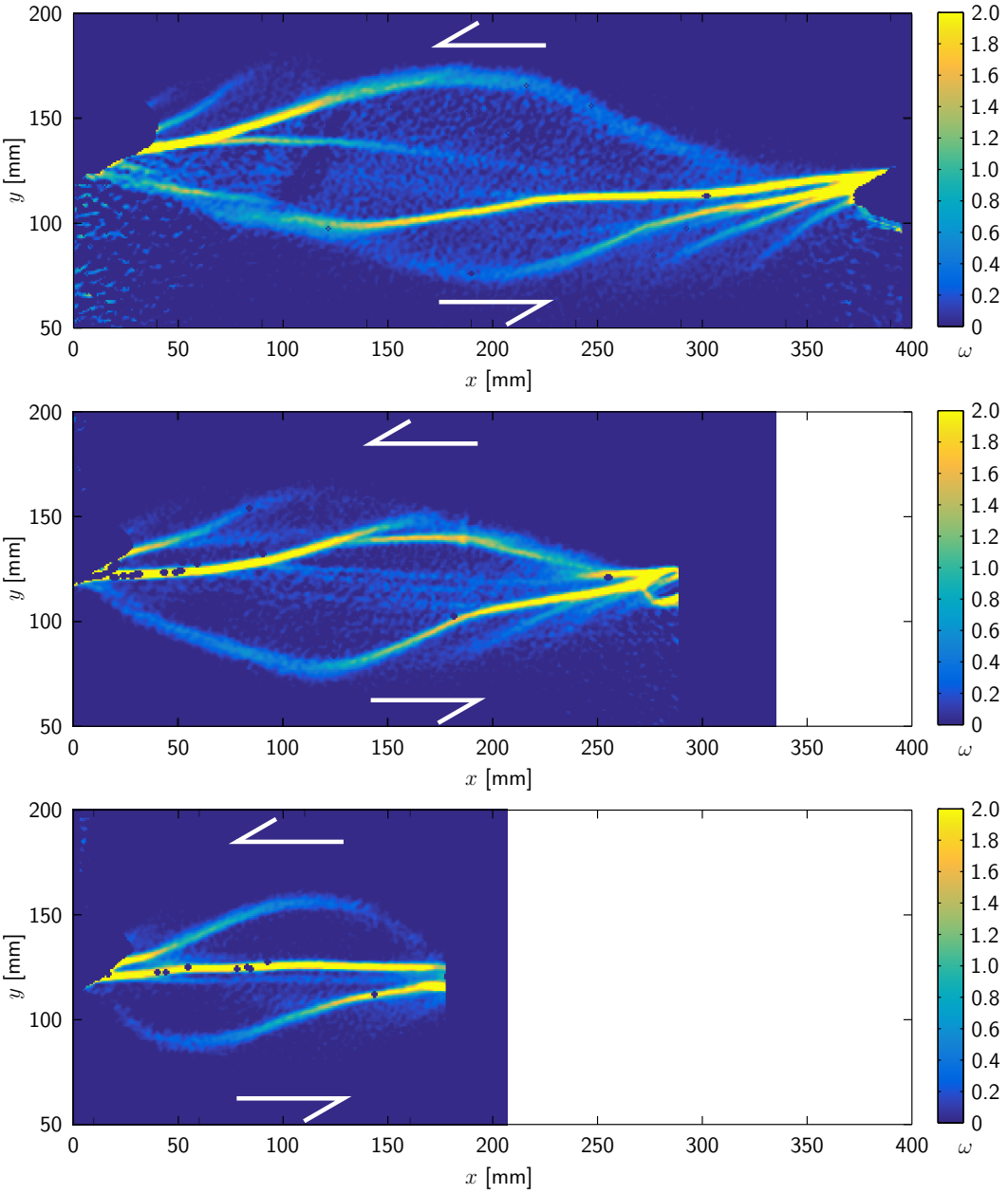

Fig. 4.5: Maps of curl of cumulative displacement fields comparing experiments with different l. The overall structure is similar with shear zones curving around each other. However, the number of abandoned shorter shear zones and the amount of diffuse deformation increase significantly with l.

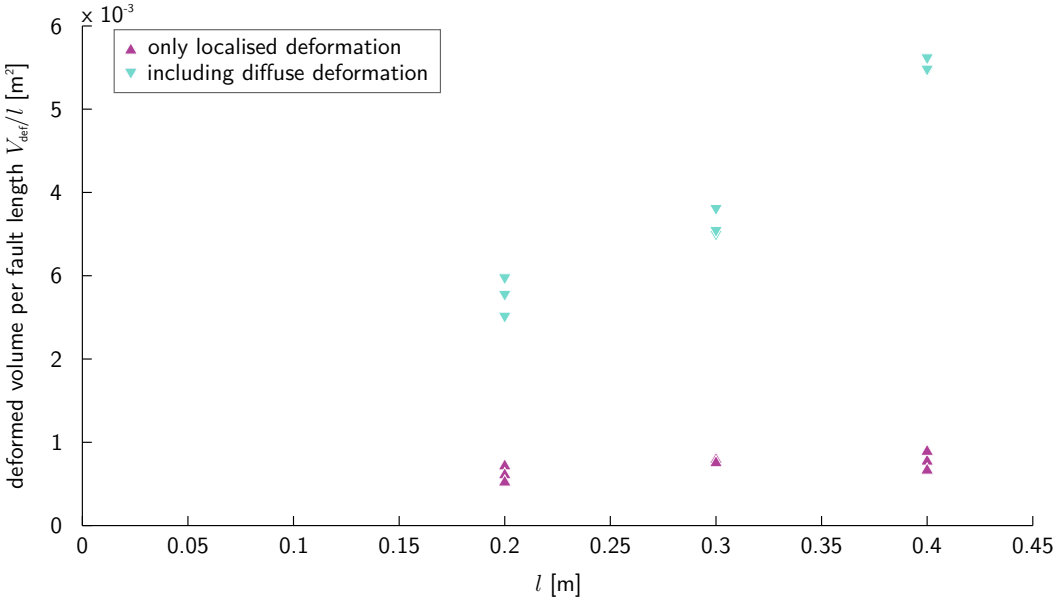

Fig. 4.6: Deformed volume normalised to fault length in strike-slip experiments. The volume of the localised deformation is approximately constant, whereas the total volume including diffuse deformation shows a more-than-linear increase with l.

gorithm thus finds a threshold that separates diffuse deformation from noise. This threshold can subsequently be applied to the final time step to measure overall diffuse deformation during the experiment. Applying the algorithm directly to the final time step, on the other hand, returns a threshold that retains only localised deformation. This is due to the fact that the intensity difference between distributed and localised deformation is much larger than between distributed deformation and noise. We are thus able to measure total deformation (of which localised deformation is only a minor fraction) and localised deformation separately.

Assuming plane strain deformation, the number of pixels displaying deformation can be transformed to the total volume V that has undergone deformation at any time during the experiment. Fig. 4.6 shows V normalised by l as a function of l. Without diffuse deformation, the volume per fault length (V_{loc}) is approximately constant. If, on the other hand, diffuse deformation is included, the volume per fault length (V_{diff}) increases overproportionately with l.

Fig. 4.7 shows along-strike profiles of distributed, cumulative slip for each experiment. These profiles are compiled by first masking out (i. e. setting to zero) areas of localised deformation and then summing up in y-direction all values $\partial u_x/\partial y$. The profiles show a maximum in the centre of the shear zones, which is in accordance with the propagation of localisation described above. Their maxima are slightly below the

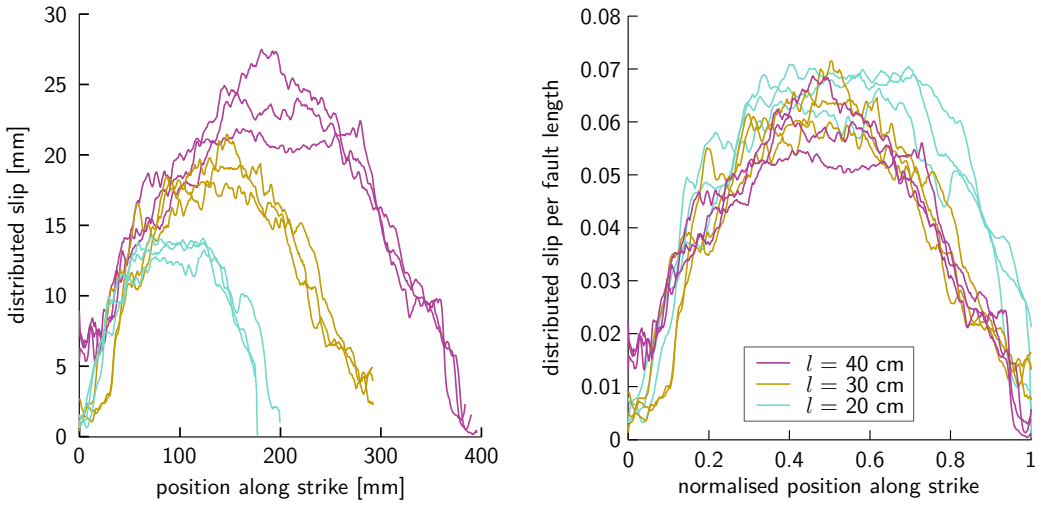

Fig. 4.7: Distributed slip profiles for the strike-slip experiments. The profiles show a maximum in the centre that corresponds to the amount of slip accumulated before weakening. Normalising both axes to fault length results in a collapse of all experiments to one profile line with a maximum at about 6 % of the fault length.

displacements required for formation of a through-going fault zone in the respective experiments, and correspond to the displacements at which weakening is complete (see below). When normalising both the position along strike and the displacement to l, the profiles show a good data collapse, with the maximum distributed slip in the centre of the shear zone being about 6 % of the fault length.

4.3.2 Force Measurements: Strain Hardening – Weakening and Work Budget

In the strike-slip set-up the pushing force was measured in all nine experiments. Fig. 4.8 exemplarily shows the shear force (corrected for basal drag) for one experiment of each l. The general behaviour is similar for each of them: The curves show a hardening – weakening peak followed by a stable sliding phase in the end. Both peak height and stable sliding force increase with l, in accordance with an increasing fault surface area. The amount of displacement needed to achieve stable sliding increases with l, too, from approximately 15 mm for $l = 200$ mm to 30 mm for $l = 400$ mm (cf. fig. 4.7).

In addition to the experiments with undisturbed sand packs, experiments with a pre-cut shear zone were carried out for $l = 400$ mm and $l = 200$ mm. As shown in fig. 4.8, they do not exhibit hardening – weakening, but, after an initial increase, directly start into the regime of stable sliding that in the undisturbed experiments

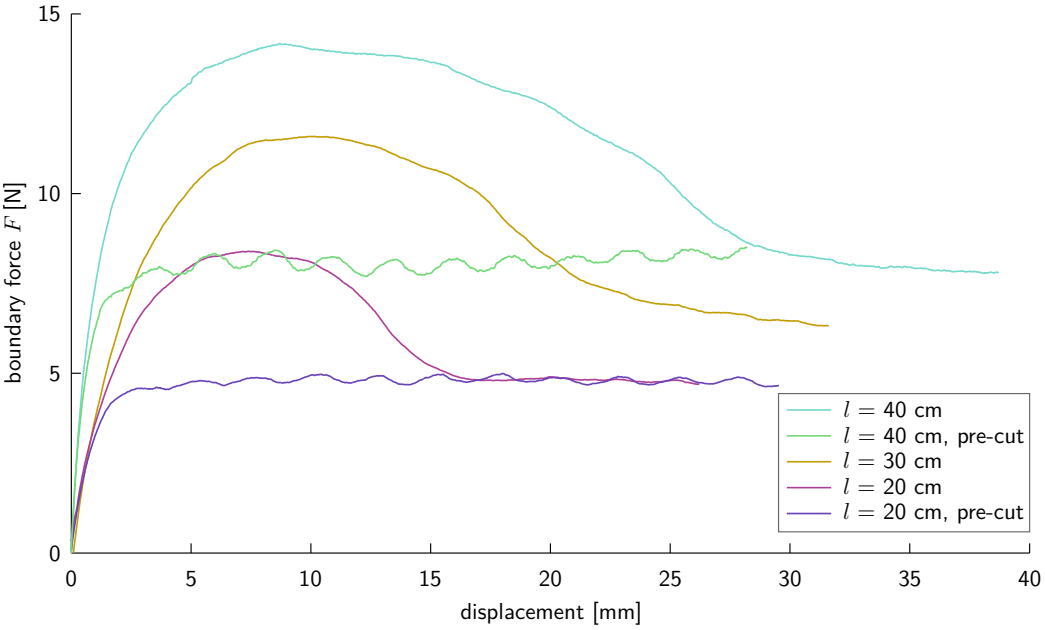

Fig. 4.8: Boundary force vs. displacement in strike-slip experiments for different shear zone lengths l. Both peak and stable sliding force increase with l, which can be explained by an increased shear zone area. Reference measurements with a pre-cut sand pack were carried out for $l = 200$ mm and $l = 400$ mm. They do not exhibit any hardening – weakening behaviour, but begin directly in the regime of stable sliding. The oscillatory pattern in these curves is probably due to the limited mechanical accuracy of the ball screws driving the deformation. The oscillation frequency corresponds to the angular frequency of the ball screws.

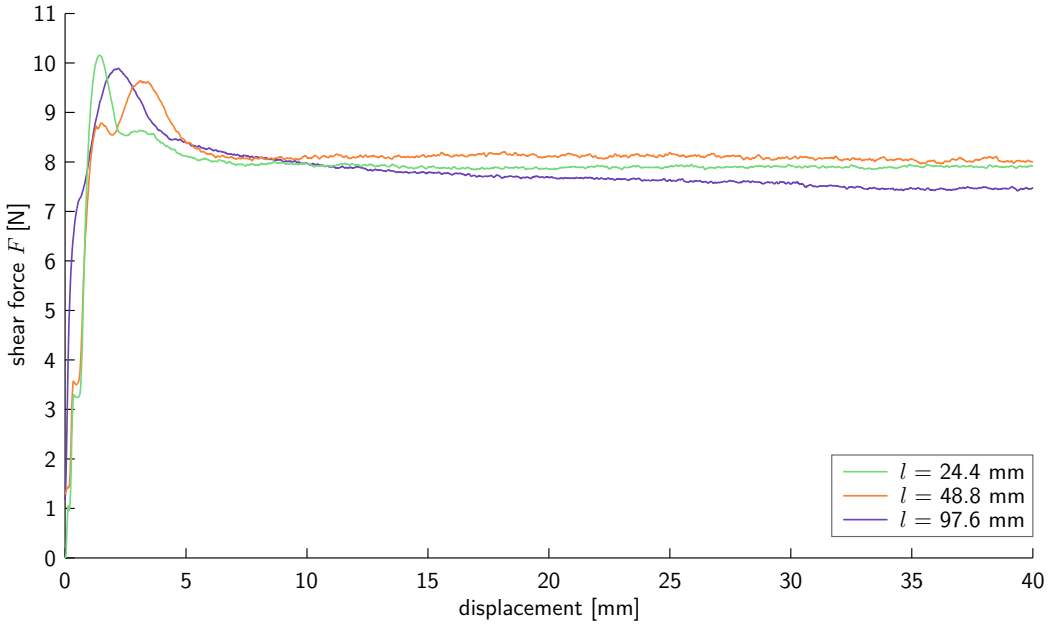

Fig. 4.9: Shear curves from RST experiments for different shear zone lengths l. Peak and stable sliding strength are similar for all curves, but the peak width changes with l. All measurements carried out at $\sigma_n = 500\,\mathrm{Pa}$. All measurements are for total force at the sensors, i. e. integrated over all fault systems.

was attained after weakening. The force in these experiments shows a cyclic variation of maximally $\pm 0.5\,\mathrm{N}$ which is considered an artefact. It reflects the limited precision of the ball screws used to drive the deformation (repeat accuracy $\pm 0.02\,\mathrm{mm}$). The frequency of the variation corresponds to the angular frequency of the ball screws. The average level of the force is very similar to the stable sliding force at the end of the undisturbed experiments.

In the RST five independent measurements were carried out for each blade configuration. The normal load was set to $\sigma_n = 500\,\mathrm{Pa}$, which corresponds roughly to the average overburden load in the centre of a 5 cm thick layer of sand, as used in the strike-slip experiments. Fig. 4.9 shows one example of a shear curve for each blade configuration. The measurements are the total force at the sensors, which is integrated over the number of fault systems created, i. e. the number of blades. As the final fault surface area is the same in all experiments independent of blade configuration, all three curves show almost identical stable shear forces and similar peak heights. The peak width, however, measured to the point where the shear force reaches a stable value, increases with blade distance, similar to what we observe in the strike-slip experiments.

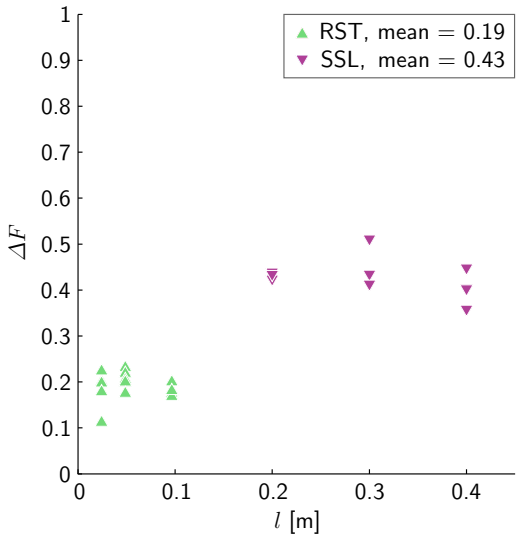

Fig. 4.10: Relative weakening in the strike-slip (SSL) is about twice as much as in the RST. Within the respective set-ups it is independent of l.

To compare the weakening during fault formation for the different fault areas that occur in the two set-ups, we define the relative weakening in terms of force, ΔF:

$$\Delta F = 1 - \frac{F_\mathrm{s}}{F_\mathrm{p}} \tag{4.2}$$

where F_p and F_s are the maximum of the stress curve ("peak") and the subsequent plateau value ("stable"), respectively. ΔF will be between zero (no force drop, i. e. no peak) and one (drop to zero after the maximum; cf. eq. 2.4). It is shown in fig. 4.10 for all experiments of either set-up. The figure clearly demonstrates that ΔF is independent of l, but differs between the two set-ups, being on average 0.19 in the RST and 0.43 in the strike-slip. This difference of approximately a factor of two is is due to the different ways shear zones are induced in the two set-ups: In the RST, stress concentrations at the tip of each blade initiate one fault per blade. These faults propagate in the direction of shear (i. e. rotation) until they meet the faults initiated at the respective next blade. Consequently, there is only one fault evolving per fault system, with the number of blades being equal to the number of fault systems. This is sketched in fig. 4.11.

In the strike-slip experiments, on the other hand, two faults evolve in one fault system, one initiating at either side of the set-up (figs. 4.4 and 4.11). They evolve in parallel and overlap until finally one of the two faults is abandoned. The total area of the fault planes is hence twice as large as it would be in the RST for the same l, which for a given material strength results in the force being twice as high, too. This changes towards the end of an experiment when one of the fault branches is abandoned. Consequently, the stable sliding force is the same as it would be in the RST for the respective l, and thus the weakening is twice as high.

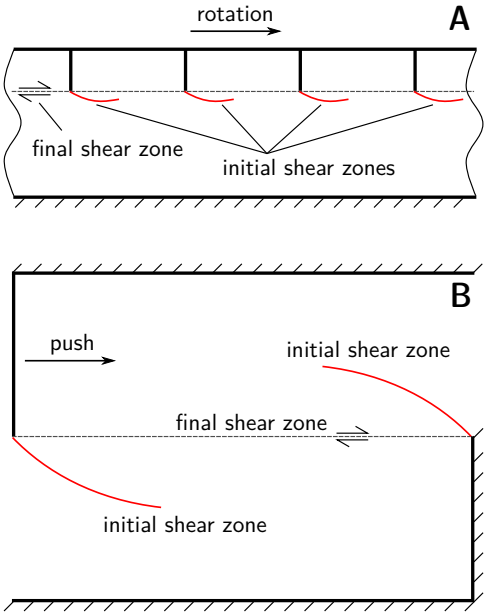

Fig. 4.11: Conceptual sketch of shear zone formation in the two different set-ups.
A: Section of the Ring-shear tester. One shear zone forms at the tip of each blade and propagates in rotation direction towards the next blade. The fault system under consideration extents from one blade towards the next; several fault systems develop simultaneously.
B: Strike-silp set-up. Only one fault system develops, that contains two faults. The work required to deform this fault system on a given scale is twice as much as in the RST. Sketches are not to scale.

From the shear curves the work for fault propagation W_{prop} is determined: The transition from weakening to stable sliding is picked by hand in each shear curve and the area under the thus confined peak is measured (see definition in fig. 4.3). The values obtained in this way represent the formation of two faults in case of the strike-slip experiments, and of a variable number of faults depending on blade configuration in case of the RST (see above). Therefore, all measurements from the strike-slip experiments are divided by two, and all measurements form the RST are divided by the number of blades in the respective experiment, before being normalised to fault height. The resulting W_{prop} as a function of l is shown in fig. 4.12. The plot shows a strongly non-linear increase of W_{prop}, with values ranging from $1\,\mathrm{mJ\,m^{-1}}$ to $1260\,\mathrm{mJ\,m^{-1}}$ for the range of l covered by our data.

Fig. 4.13 shows W_{prop} normalised to the deformed surface area A. As W_{prop} is defined as work per height, dividing by the surface area effectively results in a work per volume. It increases with l, if $A = A_{\mathrm{loc}}$ i. e. only localised deformation is taken into account. If the total diffuse deformation is considered as well ($A = A_{\mathrm{diff}}$), the work per volume is constant and about $55\,\mathrm{J\,m^{-3}}$.

4.4 Discussion

4.4.1 Assessing the Complementarity of the Two Set-Ups

Optical monitoring of the strike-slip experiments shows that the final shear zone is often curved; thus it often deviates from the shortest possible fault path which

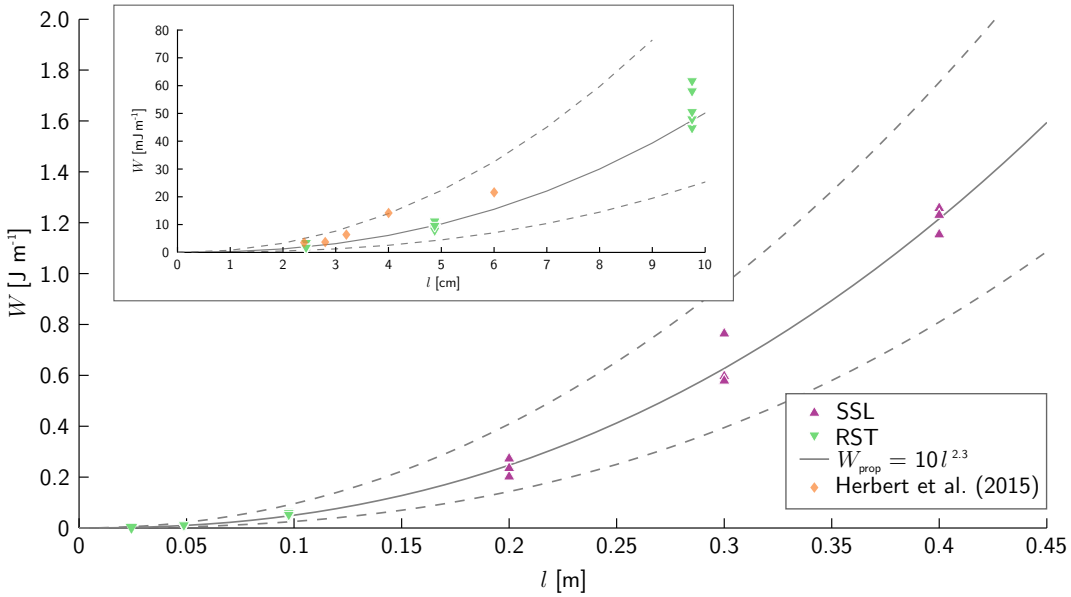

Fig. 4.12: Work required for propagation of a single fault in Ring-Shear tests (inset shows a close-up) and strike-slip experiments increases overproportionately with fault system length l. The grey lines show a power-law fit to the data (solid) and its error (dashed). Data from Herbert et al. (2015) are shown for comparison.

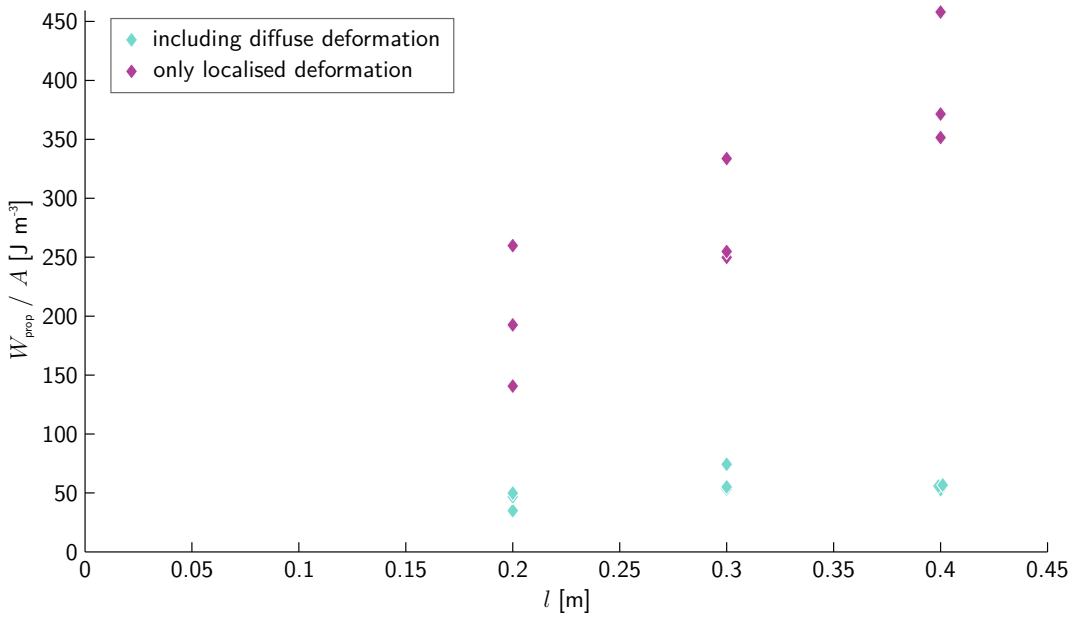

Fig. 4.13: W_{prop} normalised to the surface area of the localised shear zone increases linearly with fault length l, while it is constant at $55\,\mathrm{J\,m^{-3}}$, if diffuse deformation is included into the surface area.

might be considered the energetically preferred one. Hence it is conceivable that the evolution of the shear zone at the end of our experiments is not in a stable state yet, and more weakening might be possible. In this case ΔF and W_{prop} determined in our experiments would underestimate the true values. However, the average level of shearing force in the experiments with pre-cut, straight shear zones is similar to the stable sliding force in the experiments with undisturbed sand packs. From this we conclude that, despite the shear zones still being curved, weakening is largely complete at the end of an experiment and our estimates for ΔF and W_{prop} are good representations of the true values.

Furthermore, we have set the normal load in the RST-experiments to $\sigma_{\mathrm{n}} = 500\,\mathrm{Pa}$, which is roughly the overburden load in the centre of a 5 cm thick sand pack. By comparing the result of RST and strike-slip experiments we have implicitly assumed that this overburden load reflects the normal load on the shear zone, and that variations with depth cancel out in total. This assumption can be justified by comparing the stable sliding forces in the two set-ups: In either one, the RST and the strike-slip one (for $l = 40\,\mathrm{cm}$), stable sliding requires a force of approximately 7.9 N. The fault area is $A_{\mathrm{RST}} = 226.19\,\mathrm{cm}^2$ for the RST and $A_{\mathrm{SSL}} = 200\,\mathrm{cm}^2$ for the strike-slip experiment. Stable sliding stress is thus slightly higher in the strike-slip case than in the RST, but the difference is still within the range of measurement

variations of the strike-slip experiments. The two set-ups therefore can in fact be regarded as complementary with respect to the load conditions.

4.4.2 Interpretation at the Laboratory Scale

Our experiments show that in sand the work of fault propagation, W_{prop}, increases with fault length in a nonlinear way. In search for a law that describes both our data subsets, RST and strike-slip, with a common set of parameters, we find the closest fit with a function of the form

$$W_{\mathrm{prop}} = a l^b. \tag{4.3}$$

Here, a and b are free parameters that we determine through least squares fitting. Doing so for both subsets individually returns similar values for a and b, respectively (tab. 4.1). A joint fit to the complete dataset ("combined" in tab. 4.1) yields the empirical relation for W_{prop} in sand under the given normal load conditions:

$$W_{\mathrm{prop}} = (10 \pm 2)\,\mathrm{J\,m^{-1}} \left(\frac{l}{l^\circ}\right)^{2.3 \pm 0.2} \tag{4.4}$$

where l° is the unit length. This relation is also shown in fig. 4.12. The errors given refer to the uncertainty of the fit only (95 %-interval of confidence) and do not include the accuracy of the measurements themselves. Considering the low number of experiments conducted, it is reasonable to assume that the total error might be larger. Our data therefore do not exclude a simple quadratic dependency. Nonetheless, they are in definite contrast with the interpretation of Herbert et al. (2015) that implies a linear relationship on l. This discrepancy probably stems from the fact that their study only included a narrow range of values for l, as it was not intended to test for a relationship of W_{prop} on l but focussed on normal load instead. They used a convergent wedge setting and varied the sand pack thickness from 12 mm to 20 mm to realise different normal load conditions. However, from the specifications of their experiments we are able to derive an approximate comparison of their data to ours: We transform the sand pack thicknesses to fault lengths (assuming a fault dip of 30°) and remove the normalisation to fault length from their work data. The resulting data we project to a normal load of 500 Pa to make them comparable to our normal load conditions. The results of this projection are shown along with our RST-data in the inset in fig. 4.12. The two datasets show a good congruence which verifies the experimental approaches used in either study.

The good correlation between W_{prop} and A_{diff} that we observe in our data (fig. 4.13), supports our hypothesis of diffuse deformation being the main energy sink during fault formation in sand. As the width of the total area affected by deformation, i. e. the distance between the two outermost faults in the maps in fig. 4.5, is more or less constant, the total volume that is available for diffuse deformation increases

	a [J m^{-1}]	b
RST	19 ± 22	2.3 ± 0.5
strike-slip	10 ± 4	2.3 ± 0.4
combined	10 ± 2	2.3 ± 0.2

Tab. 4.1: Parameter returned from fitting a function of the form $W_{\text{prop}} = al^b$ to measurements of W_{prop}. The data were normalised to the number of faults and to fault heigh h prior to fitting. See text for explanation.

only linearly with l. Nevertheless, the fraction of the volume that actually becomes deformed increases according to the above power-law, resulting in an increasing density of deformed pixels in the recordings. Consequently, the maximum shear strain the material in the deformed area undergoes prior to failure is not a material property, but depends on the size of the system. This is confirmed by the observation that failure on the system scale in all experiments occurs when the distributed slip has reached about 6 % of the fault system length. Taken together, this leads to the conclusion of the average rate of fault propagation being constant over the range of l tested. We interpret this to be an indicator for localisation to be at least partially driven by the kinematic boundary condition at the edges of indenter and back-wall.

4.4.3 Application to Natural Systems

Comparison of Work Estimates

Estimates of W_{prop} in natural rock are subject to large uncertainties, mainly because of the difficulty to directly measure it at the relevant scales. A common approach assumes W_{prop} to be the sum of the work done in creating the fault itself and the work done in creating a damage zone around it (Mitra and Boyer, 1986):

$$W_{\text{prop}} = \gamma l + \gamma l r w \tag{4.5}$$

As all expressions for W_{prop} in this article, this is a two-dimensional, plane-strain formulation that implicitly assumes a unit length in the third dimension. γ is the surface energy per unit area, ranging from 10^1 J m^{-2} to 10^4 J m^{-2} for common rock-forming minerals (Wong, 1982; Cox and Scholz, 1988; Del Castello and Cooke, 2007). l is the length over which the fault grows and r is the density of fractures in the damage zone around and ahead of the fault tip, which is around 500 m^{-1} according to Mitra and Boyer (1986). w is the width of the damage zone that is 0.1 times to 0.01 times the fault displacement (Scholz, 1987). This in turn is linearly related to l by some material constant c' (Cowie and Scholz, 1992; Dawers et al., 1993), such that $w = c\,l$, where c is a material parameter of the order of 10^{-2} (Scholz, 2002). Substituting w with $c\,l$ results in:

$$W_{\text{prop}} = \gamma \left(l + c r l^2 \right) \tag{4.6}$$

The quadratic term refers to the damage zone around the fault and the linear one to the fault itself. This dependence of the spatial dimension of the damage zone on l^2 is also in accordance with modern fracture mechanics (Scholz, 2002). However, the linear term implies the fault to be a discrete, planar feature that forms in a separate process, which is probably not the case. Instead, most faults encompass a granulated core of finite width that forms by frictional wear from the intensely fractured material of the damage zone (e. g. Scholz, 2002). This process occurs whenever a fault slips and does not cease after localisation. Hence, we argue that formation of the fault core is not part of the localisation process itself. A more accurate estimate of W_{prop} would thus omit the linear term in eq. 4.6 and rather include the formation of the fault core in W_{fric} instead. However, the discrepancy between these two estimates is negligible; it is on the order of 0.1 % to 1 % for $l = 100\,\mathrm{m}$ and quickly decreases for longer faults. Following this, we assume W_{prop} in nature to be a function of l^2 which is, within the range of measurement accuracy, similar to our experimentally found values for sandbox models.

Another approach to determine W_{prop} in nature is to measure the surface area created by a single earthquake, determine the surface energy spent, and sum this over the number of earthquakes experienced by the fault. For the 100 m Bosman fault, South Africa, that formed in just one earthquake and was sampled immediately afterwards, Wilson et al. (2005) report the surface energy consumed to be in the range of approximately $3\,\mathrm{MJ\,m^{-2}}$ to $10\,\mathrm{MJ\,m^{-2}}$. For the Punchbowl fault in the San Andreas system, California, Chester et al. (2005) determine the fracture surface energy per earthquake to be approximately $0.5\,\mathrm{MJ\,m^{-2}}$. They estimate the total 44 km of displacement to have accumulated over about 10 000 earthquakes, which results in the total energy required for creation of a fault of comparable size to be $5 \times 10^9\,\mathrm{J\,m^{-2}}$ to $10^{11}\,\mathrm{J\,m^{-2}}$. Assuming a fault length of 440 km (Scholz, 2002), eq. 4.6 results in values ranging from $2.2 \times 10^7\,\mathrm{J\,m^{-2}}$ to $2.2 \times 10^{10}\,\mathrm{J\,m^{-2}}$ for the same situation.

Using the scaling factors derived in Ritter et al. (2016, chapter 2 of this thesis) we determine a model fault length of 0.88 m to be analogous to this case. From eq. 4.4 this results in $W_{\mathrm{prop}} = 8.47\,\mathrm{J\,m^{-2}}$ in the model. The scaling factor for energy per area can be calculated as the product of the scaling factors for stress and length, $\sigma^* l^* = 2.42 \times 10^{-12}$ (Ritter et al., 2016). Scaling the model result up to nature with this factor yields $W_{\mathrm{prop}} = 3.5 \times 10^{12}\,\mathrm{J\,m^{-2}}$. This is slightly higher than the values derived for natural faults above, but still acceptably close considering the uncertainty of four orders of magnitude for the natural estimates. Consequently, our results are also numerically similar to natural fault systems.

Analysis of Strain Distribution

We interpret the fault system evolving in our experiments as representing a transfer fault system linking two segments of dip-slip faults, where the two displacement

singularities (indenter and back-wall) correspond to the edges of the dip-slip faults. This termination by conversion into a dip-slip fault is one of three geometrically possible terminations of a strike-slip fault (Ramsay, 1980; Mouslopoulou et al., 2007). Natural examples include the Tjörnes Fracture zone in Iceland (Gudmundsson, 1995) and the Las Vegas Valley Shear Zone in Nevada (Duebendorfer and Black, 1992).

The pattern of overlap of the shear zones we observe in our experiments is similar to that in restraining double bends occurring in natural strike-slip shear zones (e. g. Cunningham and Mann, 2007). The uplift we observe resembles – although negligibly small with respect to the work calculations – the pop-up or positive flower structure that usually can be found in natural structures in this context (Cunningham and Mann, 2007; Cunningham, 2007). Commonly, natural restraining bends are interpreted to be related to inherited structures within the trace of a strike-slip shear zone, such as a step-over in a pre-existing basement fault (Cunningham and Mann, 2007). Our results contrastingly suggest that an inherited structure is not a necessary condition; instead restraining bends seem to develop whenever two fault segments that follow the same fault trace approach each other. This is particularly well exemplified in fig. 4.5 for the case of $l = 30\,\mathrm{cm}$, where the two segments first propagate directly towards each other before they turn outwards. We interpret this as being due to the stress distribution around each fault segment which makes it impossible for the segments to link directly tip to tip.

Furthermore, we observe a succession of short-lived shear zones that occur directly at the edges of indenter and back-wall during the hardening regime. They appear at decreasing angles with respect to the final fault trace, and their number is highest for long fault systems. Their initial orientation according to a Mohr-Coulomb failure criterion suggests that the first such shear zone represents the dynamically favoured path. The final direction of the through-going shear zone, however, is strongly predetermined by the fixed kinematic boundary condition. We therefore interpret the succession of these shear zones as being the result of a competition between the dynamically preferred and the kinematically imposed shear zone direction. To our knowledge, similar shear zone patterns have not been reported from any natural fault system so far. This might be either due to lack of preservation of such features, or due to the edge of the dip-slip fault in nature being more compliant than the indenter in the experiment, resulting in a weaker kinematic boundary condition.

In natural basin-scale fault systems, the formation of a through-going, localised fault is preceded by deformation on multiple smaller-scale, but nevertheless localised faults (McLeod et al., 2000; Cowie, Underhill et al., 2005). This precursory fault network cannot be resolved as such in the sandbox. Instead, we regard the diffuse deformation observed in our experiments as analogous to this diffusely-localised fault network, since it is persistent plastic deformation which in brittle rock always takes the form of micro-cracks, fractures and faults. From our measurements of diffuse strain we interpret the density of such fracture networks to be a function of fault system size in nature, too. This carries implications for bulk rock permeability in

sedimentary basins and reservoir rock affected by faulting, which are often controlled by fractures that are below seismic resolution. Our findings provide a relative scaling for such fracture systems based on system size. Additionally, such increase of fracture density away from the through-going fault is identical to a decrease of strain localisation. Therefore, no unique quantitative relation between strain localisation and the constant strain weakening can be formulated.

4.5 Conclusion

We have carried out analogue sandbox experiments of strike-slip deformation in which we simultaneously monitored stress and strain. We find the work of fault propagation, W_{prop}, to be directly proportional to the volume of diffusely deformed material, V_{diff}, with a numerical value of about $55\,\mathrm{J\,m^{-3}}$. In contrast to earlier sandbox studies, but consistent with theory of fault growth in nature, both W_{prop} and V_{diff} show an approximately quadratic dependence on fault system size, while at the same time the total stress drop during localisation is constant. Numerical values of W_{prop} scale well to estimates from natural fault zones. Additionally, our data for the first time show quantitatively that distributed deformation in sandbox models mimics natural damage zone evolution and can be interpreted as a proxy for deformation below seismic resolution in crustal-scale fault systems.

Acknowledgements

We thank Karen Leever for numerous fruitful discussions during the early stages of this work. Frank Neumann and Thomas Ziegenhagen provided invaluable help in designing and engineering of the experimental set-up which we gratefully acknowledge. Malte C. Ritter was supported by the Helmholtz Graduate School GeoΣim.

References

Adam, J., J. L. Urai, B. Wieneke, O. Oncken, K. Pfeiffer, N. Kukowski, J. Lohrmann, S. Hoth, W. van der Zee and J. Schmatz (2005): 'Shear localisation and strain distribution during tectonic faulting—new insights from granular-flow experiments and high-resolution optical image correlation techniques'. In: *Journal of Structural Geology* 27.2, pp. 283–301. DOI: 10.1016/j.jsg.2004.08.008.

Brady, B. T., W. I. Duvall and F. G. Horino (1973): 'An experimental determination of the true uniaxial stress-strain behavior of brittle rock'. In: *Rock Mechanics Felsmechanik Mécanique des Roches* 5.2, pp. 107–120. DOI: 10.1007/BF01240161.

Chester, J. S., F. M. Chester and A. K. Kronenberg (2005): 'Fracture surface energy of the Punchbowl fault, San Andreas system'. In: *Nature* 437.7055, pp. 133–136. DOI: 10.1038/nature03942.

Cooke, M. L. and E. H. Madden (2014): 'Is the Earth Lazy? A review of work minimization in fault evolution'. In: *Journal of Structural Geology* 66, pp. 334–346. DOI: 10.1016/j.jsg.2014.05.004.

Cooke, M. L. and S. Murphy (2004): 'Assessing the work budget and efficiency of fault systems using mechanical models'. In: *Journal of Geophysical Research: Solid Earth* 109.B10, pp. 1–13. DOI: 10.1029/2004JB002968.

Cowie, P. A. and C. H. Scholz (1992): 'Physical explanation for the displacement-length relationship of faults using a post-yield fracture mechanics model'. In: *Journal of Structural Geology* 14.10, pp. 1133–1148. DOI: 10.1016/0191-8141(92)90065-5.

Cowie, P. A., J. R. Underhill, M. D. Behn, J. Lin and C. E. Gill (2005): 'Spatio-temporal evolution of strain accumulation derived from multi-scale observations of Late Jurassic rifting in the northern North Sea: A critical test of models for lithospheric extension'. English. In: *Earth and Planetary Science Letters* 234.3-4, pp. 401–419. DOI: DOI10.1016/j.epsl.2005.01.039.

Cox, S. and C. H. Scholz (1988): 'On the formation and growth of faults: an experimental study'. In: *Journal of Structural Geology* 10.4, pp. 413–430. DOI: 10.1016/0191-8141(88)90019-3.

Cunningham, D. (2007): 'Structural and topographic characteristics of restraining bend mountain ranges of the Altai, Gobi Altai and easternmost Tien Shan'. In: *Geological Society, London, Special Publications* 290.1, pp. 219–237. DOI: 10.1144/SP290.7.

Cunningham, W. D. and P. Mann (2007): 'Tectonics of strike-slip restraining and releasing bends'. In: *Geological Society, London, Special Publications* 290.1, pp. 1–12. DOI: 10.1144/SP290.1.

Dawers, N. H., M. H. Anders and C. H. Scholz (1993): 'Growth of normal faults: Displacement-length scaling'. In: *Geology* 21.12, pp. 1107–1110. DOI: 10.1130/0091-7613(1993)021<1107:gonfdl>2.3.co;2.

Del Castello, M. and M. L. Cooke (2007): 'Underthrusting-accretion cycle: Work budget as revealed by the boundary element method'. In: *Journal of Geophysical Research* 112.B12, B12404. DOI: 10.1029/2007JB004997.

Dempsey, D., S. Ellis, R. Archer and J. Rowland (2012): 'Energetics of normal earthquakes on dip-slip faults'. In: *Geology* 40.3, pp. 279–282. DOI: 10.1130/G32643.1.

Dooley, T. P. and G. Schreurs (2012): 'Analogue modelling of intraplate strike-slip tectonics: A review and new experimental results'. In: *Tectonophysics* 574-575, pp. 1–71. DOI: 10.1016/j.tecto.2012.05.030.

Dotare, T., Y. Yamada, J. Adam, T. Hori and H. Sakaguchi (2016): 'Initiation of a thrust fault revealed by analog experiments'. In: *Tectonophysics* 684, pp. 148–156. DOI: 10.1016/j.tecto.2015.12.023.

Duebendorfer, E. M. and R. A. Black (1992): 'Kinematic role of transverse structures in continental extension: An example from the Las Vegas Valley shear zone,

Nevada'. In: *Geology* 20.12, p. 1107. DOI: 10.1130/0091-7613(1992)020<1107:KROTSI>2.3.CO;2.
Gudmundsson, A. (1995): 'Ocean-ridge discontinuities in Iceland'. In: *Journal of the Geological Society* 152.6, pp. 1011–1015. DOI: 10.1144/GSL.JGS.1995.152.01.22.
Hardy, S., C. Duncan, J. Masek and D. Brown (1998): 'Minimum work, fault activity and the growth of critical wedges in fold and thrust belts'. In: *Basin Research* 10.3, pp. 365–373. DOI: 10.1046/j.1365-2117.1998.00073.x.
Herbert, J. W., M. L. Cooke, P. Souloumiac, E. H. Madden, B. C. Mary and B. Maillot (2015): 'The work of fault growth in laboratory sandbox experiments'. In: *Earth and Planetary Science Letters* 432, pp. 95–102. DOI: 10.1016/j.epsl.2015.09.046.
Klinkmüller, M., G. Schreurs, M. Rosenau and H. Kemnitz (2016): 'Properties of granular analogue model materials: A community wide survey'. In: *Tectonophysics* 684, pp. 23–38. DOI: 10.1016/j.tecto.2016.01.017.
Lockner, D. A., J. D. Byerlee, V. Kuksenko, A. Ponomarev and A. Sidorin (1991): 'Quasi-Static Fault Growth and Shear Fracture Energy in Granite'. English. In: *Nature* 350.6313, pp. 39–42. DOI: Doi10.1038/350039a0.
Lohrmann, J., N. Kukowski, J. Adam and O. Oncken (2003): 'The impact of analogue material properties on the geometry, kinematics, and dynamics of convergent sand wedges'. English. In: *Journal of Structural Geology* 25.10, pp. 1691–1711. DOI: 10.1016/S0191-8141(03)00005-1.
Masek, J. G. and C. C. Duncan (1998): 'Minimum-work mountain building'. In: *Journal of Geophysical Research: Solid Earth* 103.B1, pp. 907–917. DOI: 10.1029/97JB03213.
McLeod, A. E., N. H. Dawers and J. R. Underhill (2000): 'The propagation and linkage of normal faults: insights from the Strathspey-Brent-Statfjord fault array, northern North Sea'. English. In: *Basin Research* 12.3-4, pp. 263–284. DOI: 10.1046/j.1365-2117.2000.00124.x.
Mitra, G. and S. E. Boyer (1986): 'Energy balance and deformation mechanisms of duplexes'. In: *Journal of Structural Geology* 8.3-4, pp. 291–304. DOI: 10.1016/0191-8141(86)90050-7.
Mouslopoulou, V., A. Nicol, T. Little and J. Walsh (2007): 'Displacement transfer between intersecting regional strike-slip and extensional fault systems'. In: *Journal of Structural Geology* 29.1, pp. 100–116. DOI: 10.1016/j.jsg.2006.08.002.
Oncken, O., D. Boutelier, G. Dresen and K. Schemmann (2012): 'Strain accumulation controls failure of a plate boundary zone: Linking deformation of the Central Andes and lithosphere mechanics'. In: *Geochemistry, Geophysics, Geosystems* 13.12. DOI: 10.1029/2012GC004280.
Otsu, N. (1979): 'A Threshold Selection Method from Gray-Level Histograms'. In: *IEEE Transactions on Systems, Man, and Cybernetics* 9.1, pp. 62–66. DOI: 10.1109/TSMC.1979.4310076.
Panien, M., G. Schreurs and O. A. Pfiffner (2006): 'Mechanical behaviour of granular materials used in analogue modelling: insights from grain characterisation, ring-

shear tests and analogue experiments'. English. In: *Journal of Structural Geology* 28.9, pp. 1710–1724. DOI: 10.1016/j.jsg.2006.05.004.

Paterson, M. S. and T.-f. Wong (2004): *Rock Deformation – The Brittle Field*. 2nd ed. Berlin, Heidelberg: Springer-Verlag, p. 347.

Ramsay, J. (1980): 'Shear zone geometry: A review'. In: *Journal of Structural Geology* 2.1-2, pp. 83–99. DOI: 10.1016/0191-8141(80)90038-3.

Rechenmacher, A. L. (2006): 'Grain-scale processes governing shear band initiation and evolution in sands'. In: *Journal of the Mechanics and Physics of Solids* 54.1, pp. 22–45. DOI: 10.1016/j.jmps.2005.08.009.

Ritter, M. C., K. Leever, M. Rosenau and O. Oncken (2016): 'Scaling the sandbox — Mechanical (dis-) similarities of granular materials and brittle rock'. In: *Journal of Geophysical Research: Solid Earth* 121.9, pp. 6863–6879. DOI: 10.1002/2016JB012915.

Scholz, C. H. (1987): 'Wear and gouge formation in brittle faulting'. In: *Geology* 15.6, p. 493. DOI: 10.1130/0091-7613(1987)15<493:WAGFIB>2.0.CO;2.

– (2002): *The Mechanics of Earthquakes and Faulting*. 2nd editio. Cambridge: Cambridge University Press, p. 471.

Scholz, C. H. and P. A. Cowie (1990): 'Determination of total strain from faulting using slip measurements'. In: *Nature* 346.6287, pp. 837–839. DOI: 10.1038/346837a0.

Schulze, D. (1994): 'Development and application of a Novel Ring Shear Tester'. In: *Aufbereitungstechnik* 35.10, pp. 524–535.

Tordesillas, A. and M. Muthuswamy (2009): 'On the modeling of confined buckling of force chains'. In: *Journal of the Mechanics and Physics of Solids* 57.4, pp. 706–727. DOI: 10.1016/j.jmps.2009.01.005.

Wilson, B., T. Dewers, Z. Reches and J. Brune (2005): 'Particle size and energetics of gouge from earthquake rupture zones'. In: *Nature* 434.7034, pp. 749–752. DOI: 10.1038/nature03433.

Wong, T.-f. (1982): 'Shear fracture energy of Westerly granite from post-failure behavior'. In: *Journal of Geophysical Research: Solid Earth* 87.B2, pp. 990–1000. DOI: 10.1029/JB087iB02p00990.

5 Conclusion and Outlook

I have carried out deformation experiments on granular material as an analogue for crustal rock. In these experiments I have investigated the evolution of transient mechanical properties and the corresponding strain evolution in a complex fault system for different normal load conditions and different fault system sizes. The study is divided into three parts:

In the first one (chapter 2), scaling parameters are established for the following experiments and for analogue tectonic sandbox experiments in general. Ring-Shear tests with a fixed fault system length are applied to determine material strength, strain weakening, and the amount of strain at failure for quartz sand and glass beads. The measurements reveal strain weakening to be highly dependent on normal load conditions. In particular, under normal load conditions usually met in tectonic sandbox experiments weakening in the tested materials is characterised by a reduction of cohesion, instead of friction as previously assumed. This introduces a scale dependence of strain weakening and consequently of scaling. In order to obtain a dynamically correct scaling for sandbox experiments using loose quartz sand, a length scaling factor $l^* = 2 \times 10^{-6}$ is suggested for which the measured parameters match natural data compiled from literature.

In a second step (chapter 3), a set-up is developed that allows for highly resolved measurements of boundary forces and deformation in sandbox experiments. The set-up is tested in two different tectonic settings, namely a convergent wedge and a Riedel-type strike-slip setting. Besides verifying the set-up, these experiments prove that diffuse deformation in sandbox experiments can indeed be attributed temporally to strain hardening. This has been proposed previously, for example, by Lohrmann et al. (2003) and Dotare et al. (2016); however, the two phenomena had not been observed directly and simultaneously before.

The third part (chapter 4) comprises a set of experiments from both, the Ring-Shear tester and the new set-up, that vary the fault system length while keeping the normal load constant. The results show material strength and strain weakening to be independent of system size. However, the total slip required to form a localised fault increases with system size, where the additional slip for longer fault systems is spent in diffuse deformation around the fault. The volume affected by diffuse deformation increases correspondingly, i. e. deformation becomes more pervasive instead of more intense. Increasing diffuse deformation in this way effectively decreases strain localisation, such that there is no unique correlation between the amount of strain weakening on one hand and the amount of strain localisation on the other hand.

The increase of diffuse deformation observed in the experiments is reflected by the work required for fault growth, W_{prop}, which increases approximately quadratically with fault length. This dependency is similar to theoretical predictions for natural scenarios, as are the numerical values for W_{prop}. From this analogy, diffuse deformation in sandbox experiments can be interpreted as a proxy for small-scale faulting in natural systems, similar to that observed by e. g Oncken et al. (2012) in the Andes. The density of this small-scale faulting in natural fault systems can thus be related to the system size, such that in large systems a particularly dense network of fractures is to be expected.

From the observations reported in this thesis some new research questions arise. For example, in chapter 2 a change of weakening behaviour is reported and its influence on the applicability of the tested material for analogue models is discussed. However, the mechanism causing this change could not be determined with certainty. A future study might address this through a combined approach of numerical DEM models (Distinct Element Models) and physical experiments. Such study should also investigate possible effects of the changing weakening mechanism on the evolution of W_{prop}.

Furthermore, the analysis of W_{prop} carried out on the strike-slip experiments in chapter 4 assumed a plane strain situation, although minor uplift can be observed. Such approximation is probably justified, as the uplift is comparatively small. However, a possible follow-up study using this set-up should include three-dimensional optical monitoring (e. g. stereoscopic cameras) to quantify the influence of uplift and verify the plane-strain approximation.

A third question regards the step-wise pattern of strain evolution observed. It might be controlled by the amount of weakening, which affects the energy balance and thus the timing of fault formation. Further experiments are needed to investigate this relationship which might also be applied to the North Anatolian Fault Zone (NAFZ). Here a pattern of deformation and rupture propagation from East to West can be observed that can be linked to earthquake magnitude (Bohnhoff et al., 2016) and is remarkably similar to the strain evolution observed in the experiments. Understanding this behaviour in the models might shed light on the mechanisms underlying this propagation pattern in nature, despite the different time-scale.

References

Bohnhoff, M., P. Martínez-Garzón, F. Bulut, E. Stierle and Y. Ben-Zion (2016): 'Maximum earthquake magnitudes along different sections of the North Anatolian fault zone'. In: *Tectonophysics* 674, pp. 147–165. DOI: 10.1016/j.tecto.2016.02.028.

Dotare, T., Y. Yamada, J. Adam, T. Hori and H. Sakaguchi (2016): 'Initiation of a thrust fault revealed by analog experiments'. In: *Tectonophysics* 684, pp. 148–156. DOI: 10.1016/j.tecto.2015.12.023.

Lohrmann, J., N. Kukowski, J. Adam and O. Oncken (2003): 'The impact of analogue material properties on the geometry, kinematics, and dynamics of convergent sand wedges'. English. In: *Journal of Structural Geology* 25.10, pp. 1691–1711. DOI: 10.1016/S0191-8141(03)00005-1.

Oncken, O., D. Boutelier, G. Dresen and K. Schemmann (2012): 'Strain accumulation controls failure of a plate boundary zone: Linking deformation of the Central Andes and lithosphere mechanics'. In: *Geochemistry, Geophysics, Geosystems* 13.12. DOI: 10.1029/2012GC004280.

Acknowledgements

I wish to thank my supervisors – Karen Leever, Matthias Rosenau and Onno Oncken – for their support and guidance during my work on this project. In many long discussions they helped me develop the ideas on which this thesis is based.

The experimental work would not have been possible without the help of Frank Neumann and Thomas Ziegenhagen, who turned my obscure ideas about set-ups into machines that actually work and always provided helping hand when I needed one.

On a more personal level I am very grateful to my parents for supporting me through all the years of study that preceded the completion of this thesis and for encouraging me to plough on whenever things were not working out as planned. Finally I would like to say "Thank you!" to my fellow PhD-students at GFZ for making my time here a pleasant one.

This work was supported by the Helmholtz Graduate School GeoΣim.

Curriculum Vitae

For reasons of data protection the curriculum vitae is not included in this online version.

For reasons of data protection the curriculum vitae is not included in this online version.